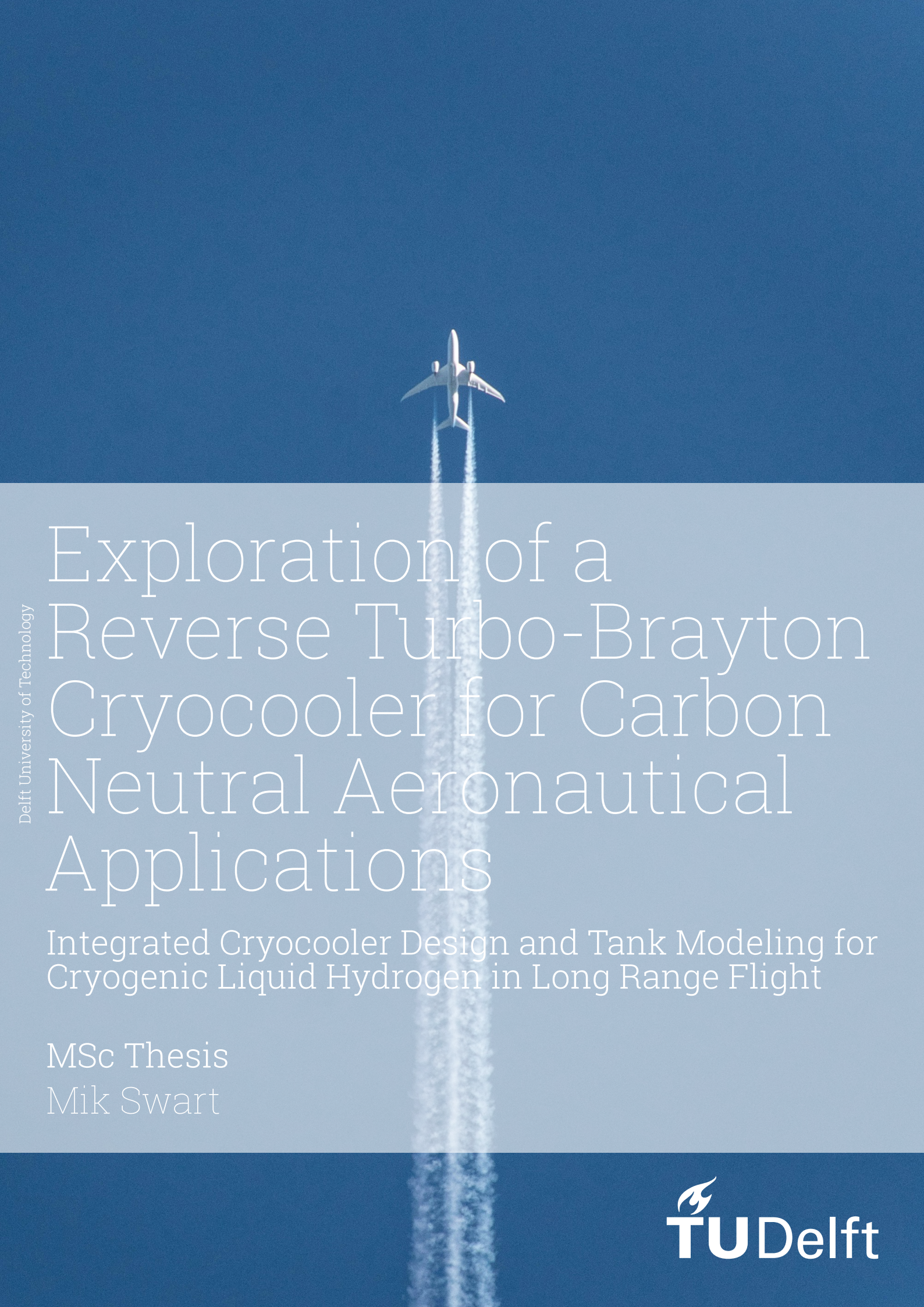

Exploration of a Reverse Turbo-Brayton Cryocooler for Carbon Neutral Aeronautical Applications

Integrated Cryocooler Design and Tank Modeling for Cryogenic Liquid Hydrogen in Long Range Flight

MSc Thesis

Mik Swart

Delft University of Technology

TU Delft

Exploration of a Reverse Turbo-Brayton Cryocooler for Carbon Neutral Aeronautical Applications

Integrated Cryocooler Design and Tank Modeling for Cryogenic Liquid Hydrogen in Long Range Flight

by

Mik Swart

to obtain the degree of Master of Science in Aerospace Engineering

at the Delft University of Technology,

to be defended publicly on Friday May 17, 2024 at 10:00 AM.

Student number:	4677129	
Thesis committee:	Prof. dr. ir. P. Colonna,	TU Delft, Chair
	Dr. ir. M. Pini,	TU Delft, Supervisor
	Dr. ir. C. M. De Servi,	TU Delft, Co-Supervisor
	Dr. ir. N. A. K. Doan,	TU Delft, Examiner

The cover image by Ben Klewais is available at `http://bit.ly/48JDTFf`

An electronic version of this thesis is available at `http://repository.tudelft.nl/`.

TU Delft

Preface

This manuscript marks the end of my time as a student at the TU Delft. Since the first time I arrived in Delft, I have learned something new and exciting every single day. Not just at the faculty, but from everyone I have had the privilege to study, work and live with. I am grateful for being surrounded by brilliant and ambitious people every day, and I will forever cherish these years as a student.

The research I have done would not have been possible without the guidance and support of Matteo, who trusted me with this fascinating yet challenging topic. I am very grateful for his supervision, kindness, great feedback and ideas throughout. He kept me sharp, made sure I pushed the envelope, and broadened my skills and perspective. Additionally, I want to thank Carlo for having the patience to go through countless iterations of the Modelica model with me over the past years. Although not originally intended, I am very thankful he helped supervise this part of my research. I would also like to thank Andrea, for introducing me to TurboSim and including the hydrogen tank model in his DynTherM library.

To my parents and brother, you have been my biggest allies through it all. Without your unconditional support, love, and advice none of it would have been possible. To my friends, thank you. You have made my time as a student that much more enjoyable.

Every thing I learned, every opportunity I got, and every experience over the past years fuelled my curiosity, ambition, inspiration, and my passion for the field of Aerospace Engineering. Closing this chapter in Delft and leaving it behind is difficult, but I am as much excited for what the future will bring me. I intend to continue learning each day, and cannot wait to begin the rest of my life. Starting tomorrow.

Mik Swart
Delft, April 2024

Summary

Climate change is an important problem in current society. In the climate change debate, civil aviation is a highly controversial topic. Global aviation accounts for 1.9% of all greenhouse gas emissions, 2.5% of CO_2 emissions and 3.5% of effective radiative forcing. Although the current emissions are small, civil aviation is expected to emit almost 50% of the CO_2 emissions in the transport sector by 2070. It is, therefore, important that immediate action is taken to develop technologies for net-zero flight. Hydrogen aircraft are an excellent alternative to the current kerosene aircraft, and appear to be the most viable solution for net-zero flight in the long term. One of the main challenges for hydrogen aircraft is to sustain a low boil-off rate for the LH_2 fuel tanks. Currently, aircraft designers have two ways to control this boil-off. That is, the use of insulation, and careful design of the tank shape. The research in this thesis explores an additional method, i.e. the active cooling of the LH_2 mixture in the fuel tank. Through a literature study, it has been identified that Reverse Turbo-Brayton cycles are the most interesting research topic for high-capacity aerospace cryocoolers for boil-off reduction. The research in this thesis is, therefore, focused on high-capacity Reverse Turbo-Brayton Cryocoolers (RTBC) for hydrogen aircraft, and the modelling of boil-off for airborne LH_2 tanks. This is in line with the Climate Action mission of the Delft University of Technology.

The purpose of this research is twofold. First, it is to open the public research space in high-capacity airborne cryocoolers. Second, it is to show the potential of the use of airborne cryocoolers for cryogenic hydrogen storage in the next generation hybrid/electric aircraft. The work in this thesis is one of the first research efforts on aeronautical RTBC outside the United States, and one of few public research efforts on this topic performed in the world. Additionally, this work describes the first detailed numerical thermodynamic modelling effort of cryogenic liquid hydrogen fuel storage in aircraft. This report furthermore presents the integrated modelling of the RTBC, its compressor design, and the LH_2 fuel tank for an exploration study of the carbon neutral hydrogen concept of the long range Flying-V aircraft.

The main outcomes of this work can be split in two parts. The first part is related to the constructed models, and is the following. First, a dynamic, modular, hierarchically structured, a-causal declarative LH_2 tank model has been developed based on conservation laws and the first principles of thermodynamics. This model can be used for the conceptual design and modelling of liquid hydrogen fuel tanks in long range aircraft with and without active cooling, in order to minimise boil-off. Furthermore, a single-stage Reverse Turbo-Brayton Cryocooler system model has been developed based on fundamental thermodynamics, with the option to optimise the system design for the maximum Coefficient of Performance (COP). In addition, the design methodology of an in-house model for the conceptual design of centrifugal compressors based on Local Dimensionless or Scaling Analysis has been presented. An alternative for its multi-objective design optimisation was developed, which can visualise multi-dimensional parametric studies. All models have been verified, and validated by comparison with experimental data.

The second part of the outcome is related to the integrated use of the models. For the exploration study of the hydrogen Flying-V aircraft, an RTBC design has been presented that supplies a cooling power of 800 W at 22 K. This RTBC has a COP of 41% of the Carnot COP, which is almost a doubling in efficiency compared to state-of-the-art low capacity RTBC. The conceptual design for its high-capacity miniature compressor has been performed, resulting in an efficiency of 86%. The influence of the design variables and parameters during its optimisation have been discussed, and it has been identified that manufacturing constraints have a substantial effect on the compressor stage performance. Based on the integrated modelling effort with the liquid hydrogen fuel tank model, it has been demonstrated that there is no weight benefit of using an RTBC for the active cooling of the hydrogen fuel tank in the Flying-V concept in its current state. The RTBC design is expected to weigh 304 kg and have a required power of 25.5 kW. This additional mass and power consumption is not outweighed by the reduction in venting and the decrease in boil-off mass of 44 kg. However, it has been shown that the use of an RTBC decreases the insulation thickness for minimum total tank and boil-off mass. Aside from an additional weight saving of up to 60%, it increases the available volume for hydrogen storage. For an 800 W RTBC, this results in a range increase of almost 1000 km to a total of 9880 km, which is only 900 km short of the range with kerosene. From the results of the study, it is concluded that the RTBC might offer a valuable addition to the Flying-V design space for boil-off control in addition to careful design of the insulation and tank shape, and provided that the weight of the RTBC is lower than 304 kg.

Contents

List of Figures

List of Tables

Nomenclature

Abbreviations

Abbreviation	Definition
AExxxx	Aerospace Engineering course code
AMS	Amsterdam airport code
CFD	Computational fluid dynamics
CNC	Computer numerical control
CO_2	Carbon dioxide
COP	Coefficient of Performance
CPPPO	Computational Propellant and Pressurisation Program
CSE	Classical Similarity Equation
CV	Control volume
DAE	Differential Algebraic Equation
DASSL	Differential Algebraic System Solver
EDS	Earth Departure Stage
EoS	Equations of State
FV-900	Aircraft type of Flying-V family
GDA	Global Dimensionless or Scaling Analysis
GDP	Gross domestic product
GODU LH2	Ground Operations Demonstration Unit for Liquid Hydrogen
HEX	Heat exchanger
HST	Hubble Space Telescope
HTS	High temperature superconducting
IGV	Inlet guide vane
KLM	Koninklijke Luchtvaart Maatschappij (Royal Dutch Airlines)
LAX	Los Angeles airport code
LDA	Local Dimensionless or Scaling Analysis
LEO	Low earth orbit
LH_2	Liquid hydrogen
LLC	Limited liability company
LPS	Low pressure side
LSP	Laminated slotted plate
MDO	Multidisciplinary design analysis and optimisation
MDPDOT	Multi-Dimensional Parametric Design Optimisation Tool

Abbreviation	Definition
MgB2	Magnesium diboride
MTOW	Maximum Take-Off Weight
NASA	National Aeronautics and Space Administration
NFA	Network Flow Analysis
NICMOS	Near Infrared Camera and Multi-Object Spectrometer
NIST	National Institute of Standards and Technology
ODE	Ordinary Differtial Equation
OEW	Operational Empty Weight
ORC	Organic Rankine Cycle
ROCETS	Rocket Engine Transient Simulation
ROM	Reduced order model
RPM	Rotations per minute
PRSV	Peng–Robinson cubic equation of state with the Stryjek–Vera modification
RTBC	Reverse Turbo-Brayton Cryocooler
RTC	Reverse Turbo-Brayton
SIN	Singapore airport code
SMARTS	Simple Model of the Atmospheric Radiative Transfer of Sunshine
STS	Space Transportation System
TankSIM	Tank System Integrated Model
TRL	Technology Readiness Level
TS	Temperature-Entropy
TVS	Thermodynamic Venting System
USD	United States dollar
ZBO	Zero boil-off

Symbols

Symbol	Definition	Unit
a	Speed of sound	[m/s]
A	Surface area	[m^2]
AR	Aspect Ratio	[-]
c_p	Specific heat capacity at constant pressure	[J/kgK]
c_v	Specific heat capacity at constant volume	[J/kgK]
C_m	Heat capacity	[J/K]
COP	Coefficient of Performance	[-]
D	Diameter	[m]
F	Force	[N]
F_f	Tank fill fraction	[-]

Symbol	Definition	Unit
FoS	Factor of Safety	[-]
g	Gravitational acceleration	[m/s^2]
H	Height	[m]
h	Convective heat transfer coefficient	[W/m^{2}K]
h	Height	[m]
h	Specific enthalpy	[J/kg]
k	Impeller shape factor	[-]
k	Thermal conductivity of a fluid	[W/mK]
L	Length	[m]
M	Mach number	[-]
M	Mass	[kg]
$\dot{m}$	Mass flow rate	[kg/s]
N	Number	[-]
n	Number	[-]
Nu	Nusselt number	[-]
OR	Operating range	[-]
P	Power	[W]
P	Pressure	[Pa]
Pr	Prandtl number	[-]
$\mathcal{P}_S$	Entropy production	[J/K]
Q	Heat load	[J]
$\dot{Q}$	Heat transfer rate	[W]
q	Mass flow rate	[kg]
R	Radius	[m]
R	Specific gas constant	[J/kgK]
r	Radius	[m]
Ra	Arithmetic mean surface roughness	[m]
Ra	Rayleigh number	[-]
Re	Reynolds number	[-]
s	Specific entropy	[J/kgK]
SP	Size parameter	[-]
T	Temperature	[K]
t	Thickness	[m]
t	Time	[s]
U	Internal energy	[J]
U	Velocity	[m/s]
V	Volume	[m^3]
v	Specific volume	[m^3/kg]
$\dot{W}$	Rate of work	[W]
w	Mass flow rate	[kg]
x	Vapour quality	[-]

Symbol	Definition	Unit
y	Liquid level as referred to the centreline of the tank	[m]
y	Vector containing the stage main performance and characteristic parameters	[-]
$\boldsymbol{y}$	Vector containing the stage main performance and characteristic parameters	[-]
α	Absolute flow angle	[$^\circ$]
β	Pressure ratio	[-]
β	Thermal expansion coefficient	[1/K]
β	Recuperator loss parameter	[-]
γ_{P_v}	Isentropic pressure-volume exponent	[-]
ϵ	Emittance factor	[-]
ϵ	Nummerical error	[-]
ϵ_R	Thermal effectiveness of the recuperator	[-]
ϵ	Clearance	[m]
η	Efficiency	[-]
λ	Thermal conductivity	[W/mK]
μ	Dynamic viscosity	[Pa s]
Π	Compression ratio	[-]
ρ	Density	[kg/m^3]
σ	Stefan-Boltzmann constant	[W/m^{2}K^4]
σ	Centrifugal stress	[Pa]
σ_y	Yield stress	[Pa]
$\boldsymbol{\sigma}$	Vector containing the stage dimensionless geometrical characteristics	[-]
τ	Time constant	[s]
Φ_{t1}	Swallowing capacity	[-]
χ	Degree of reaction	[-]
ψ	Work (or loading) coefficient	[-]
Ω	Radial velocity	[rad/s]

Subscripts

Subscript	Definition
ax	Axial
b	Back-flow
bl	Blade
c	Condensation
c	Compressor
$choke$	Choke
$CHEX$	Cold-end heat exchanger
$comp$	Compressor

Subscript	Definition
$cond$	Condensation
cyl	Cylinder
des	Design
$drop$	Drop
env	Environment
eq	Equivalent
ev	Evaporation
$evap$	Evaporation
ext	Ecternal
$fuel$	Liquid fuel
g	Gas
h	Hub
i	Internal
$ideal$	Ideal
int	Internal
l	Liquid
l	Liquid fuel
ls	Saturated liquid
$LH2$	Liquid hydrogen
max	Maximum
opt	Optimum
opt	Optimised
out	Outlet
pax	Passenger
$pinch$	Pinch
r	Ratio
r	Reduced
R	Recuperator
rad	Radiation
$real$	Real
R_L	Recuperator loss
s	Shroud
sl	Surface layer-liquid
$start$	Starting value
s	Surface evaporation/condensation
sup	Surface layer
$surf$	Surface evaporation/condensation
t	Tip
t	Total
t	Total
t	Total

Subscript	Definition
T	Turbine
ts	Total-to-static
tt	Total-to-total
$turb$	Turbine
v	Venting
vap	Vaporisation
$vent$	Venting
vol	Volume
vs	Saturated vapour
vs	Vapour-surface layer
w	Wall
$wcond$	Wall conduction
$WHEX$	Warm-end heat exchanger
wl	Wall-liquid
wt	Total wall
wv	Wall-vapour

1 Introduction

The introduction to this Master of Science Thesis starts with the background of and motivation for the research. This is then followed by the original contributions of this work to the aerospace research field, with lastly an overview of the research and document structure.

1.1. Background and Motivation

Climate change is an important topic in current society. For many, the climate change crisis is a part of everyday work or talk. In this climate change debate, civil aviation is a highly controversial topic. Civil aviation is the quickest means of transport available, reducing the time to reach parts of the world from weeks to less than a day. Civil aviation is, therefore, crucial to globalisation. In 2016, the total economic impact totalled USD 2.7 trillion, which amounts to 3.6% of the global gross domestic product (GDP) [34]. However, civil aviation is often criticised about its environmental impact that is caused by a wealthy minority. Although no hard numbers exist, the most cited estimate states that less than 20% of the global population has ever flown[1]. This relative climate influence is often subjected to debate. The total global emissions are, however, small. Global aviation accounts for 1.9% of all greenhouse gas emissions, 2.5% of CO_2 emissions and 3.5% of effective radiative forcing [56, 32].

The main challenge for the Aeronautical sector is decarbonisation. Difficulties for quick decarbonisation are long aircraft development time, the complexity of designing new airborne technologies, extensive safety testing and certification periods, and slow fleet turnover rate. Due to this, civil aviation is expected to emit almost 50% of the CO_2 emissions in the transport sector by 2070 [50]. It is, therefore, important that immediate action is taken to develop technologies for net-zero flight.

Hydrogen aircraft are an excellent alternative to the current kerosene aircraft, and appear to be the most viable solution for net-zero flight in the long term [91, 2]. One of the biggest challenges for hydrogen aircraft is storing and handling the hydrogen onboard. Although compressed gaseous hydrogen (GH_2) can be used for small aircraft, the majority of the proposed hydrogen aircraft designs in literature use liquid hydrogen (LH_2) due to its superb gravimetric efficiency [92, 2, 91]. LH_2 tanks for space applications do exist, however, for the aeronautical sector they do not. LH_2 tanks for aircraft need lower boil-off rates and longer lifetimes than current tank designs [2]. Hereof, boil-off is the primary issue for long-term storage of cryogenic hydrogen [67].

Currently, aircraft designers have two ways to control boil-off. That is, the use of insulation, and careful design of the tank shape. An additional method of interest is active cooling with a cryocooler. The research in this thesis is, therefore, focused on high-capacity cryocoolers for hydrogen aircraft, and the modelling of boil-off for airborne LH_2 tanks. This is in line with the Climate Action mission of the Delft University of Technology, that states that "TU Delft will harness its innovative powers to support the world-wide transition to non-fossil energy, and adaptation of the living environment to the consequences of global warming." [2]

A large number of long life cryocoolers, representing various thermodynamic cycles and hybrid combinations have been developed over time for space applications. In the operating temperature range of 18-45K, which is the range where cryocoolers for LH_2 tanks fall, some prominent solutions exist. These include Single- and Multi-Stage Stirling, Dual Temperature, Continuous Sorption, Reverse Turbo-

[1] https://www.cnbc.com/2017/12/07/boeing-ceo-80-percent-of-people-never-flown-for-us-that-means-growth.html#:~:text=%E2%80%9CLess%20than%2020%20percent%20of,the%20entire%20economy%2C%20Muilenburg%20said.

[2] https://www.tudelft.nl/en/tu-delft-climate-institute/tu-delft-position-on-climate-action

Brayton, and Pulse Tube cryocoolers [84]. Of the aforementioned cryocooler cycles, Reverse Turbo-Brayton cycles are an increasingly interesting research topic for high-capacity aerospace cryocoolers. Applications in the Space sector are future NASA and United States Department of Defense long-duration space missions [43]. Applications are, including but not limited to, planetary and extraterrestrial exploration missions, space-based lasers, extended-life orbital transfer vehicles, and space depots [97].

In the Aeronautical sector, applications of the Reverse Turbo-Brayton cycle might be short, medium and long-duration flights having cryogenic hydrogen storage or superconducting components at cryogenic temperatures. For cryogenic hydrogen storage, a cryocooler can be used to minimise boil-off and to provide pressure control. For superconducting components, the cryocooler can be used to cool the component to the required temperature for minimum electric resistance. Reverse Turbo-Brayton Cryocoolers (RTBC) outperform other cryocoolers for these applications. This is due to their flexible integration within the aircraft or spacecraft, the ability to cool remote and distributed loads, extremely low vibration emittance, long and maintenance free lifetimes, and high efficiency and low system mass at low temperatures and high capacities [100].

Currently, Creare LLC is the only company performing research on RTBC for aerospace applications in cooperation with NASA and the United States Department of Defense. The research set out in this thesis, therefore, is one of the first research efforts on aeronautical RTBC outside the United States, and one of few public research efforts on this topic performed in the world. The purpose of this research is twofold. First, it is to open the public research space in high-capacity airborne cryocoolers. Second, it is to show the potential of the use of airborne cryocoolers for cryogenic hydrogen storage in the next generation hybrid/electric aircraft.

The research proposed here is focused on the turbomachinery of the RTBC, whereas a different MSc student of the research group Propulsion & Power, Faculty of Aerospace Engineering at the Delft University of Technology focuses on the heat exchangers of the same proposed RTBC system. Currently no openly available thermodynamic model of cryogenic storage tanks for aircraft applications can be found in literature. The scope was therefore extended to include thermodynamic modelling of cryogenic hydrogen in a cryogenic storage tank for aircraft. This model can be used for any further study on hydrogen storage in aircraft, such as research on the Flying-V or other advanced programs such as AeroDelft.

1.2. Original Contributions

The original contributions documented in this thesis can be summarised as follows:

- A documentation of all research efforts towards Reverse Turbo-Brayton Cryocoolers, with a focus on turbomachinery.
- A fundamental thermodynamic system model of a single stage Reverse Turbo-Brayton Cryocooler, intended for conceptual design.
- A dynamic, modular, hierarchically structured, a-causal declarative model of a two-phased liquid hydrogen fuel tank for aeronautical applications with venting and active cooling, intended for conceptual design.
- A component-wise multi-dimensional parametric design optimisation tool for the on- and off-design with the in-house reduced-order compressor model (Giuffré, Colonna, and Pini [38]).
- The first detailed documented system design of a single stage Reverse Turbo-Brayton Cryocooler for aeronautical applications, including the conceptual design of its centrifugal compressor.
- Insights on the feasibility and benefits of active cooling of the liquid hydrogen fuel tank concept of the carbon neutral long range Flying-V aircraft (Woensel [94]), and a new and novel insight regarding the effect of insulation thickness and cooling on the cruise range.

1.3. Overview of the Research

The research is structured in order to fulfil its purpose. First, a literature study on Reverse Turbo-Brayton Cryocoolers (RTBC) and liquid hydrogen fuel tanks is performed. Based on this study, a system model for the RTBC and a model for the liquid hydrogen fuel tank is constructed. To demonstrate the performance of the turbomachinery, a detailed conceptual design of the centrifugal compressor is made. All three models are integrated to perform an exploration study on the active cooling of the liquid hydrogen fuel tank concept of the carbon neutral long range Flying-V aircraft (Woensel [94]). Finally, a new insight is presented to show the use of the integrated models to widen the understanding and feasability of carbon neutral aeronautical applications.

2 Background

This chapter contains background information about state-of-the-art research on Reverse Turbo-Brayton Cryocoolers and cryogenic liquid hydrogen tanks. Subsection 2.1 includes all information about the first, and Section 2.2 about the latter.

2.1. Reverse Turbo-Brayton Cryocooler

This section entails the state-of-the-art about Reverse Turbo-Brayton Crycoolers (RTBC). In the first section, the thermodynamic cycle of the system is explained. The second section deepens into the turbomachinery components of the system, and the third section briefly mentions characteristic of the recuperator component. The fourth section treats the RTBC applications, including the only implemented aerospace application.

2.1.1. The Reverse Turbo-Brayton Cycle

Reverse Turbo-Brayton Cryocoolers rely on an inversion of the standard Brayton cycle, as found in most aero engine gas turbines. A schematic and a TS-diagram (Temperature-Entropy diagram) of a single stage RTBC are depicted in Figure 2.1. The working fluid of the cycle is a single-phase fluid, which is chosen based on the thermodynamic performance for the targeted cooling load and temperature. Fluids for RTBC are typically nitrogen for cooling load temperatures above 100 K, neon for temperatures between 100 K and 30 K, and helium for cooling load temperatures below 30 K. The standard single stage RTB-cycle consists of one or more centrifugal compressors, a recuperator, one or more centrifugal turbines, a warm heat sink and a cooling load heat exchanger. The working fluid enters the compressor(s) on the warm end of the RTB-cycle, where it is compressed and circulated through the cycle (1-2). The compressor(s) are driven by electric motors, and are typically decoupled from the turbine(s). The heat of compressing the working fluid, aerodynamic losses and electrical losses are then removed from the cycle using the warm heat sink (2-3). The aftercooler typically rejects the heat into its environment, which for space applications is done by a passive radiator into space. After leaving the hot heat exchanger (HEX), the fluid enters the recuperator. Here, the gas is precooled by the colder low pressure stream leaving the cooling load HEX (3-4). Being cooled down to a substantial lower temperature, the working fluid enters the centrifugal turbine(s) (4-5). Here, the fluid is expanded, cooling the fluid to the required temperature. The shaft power generated is either dissipated or recovered by a turbo-alternator. The fluid then passes the load interface HEX, where the cycle absorbs heat from the cooling load (5-6). After leaving the cooling load HEX, the fluid is redirected to the recuperator where it gets preheated to enter the compressor by the hot stream leaving the aftercooler, in order to restart the cycle at point 1 (6-1) [97].

As can be seen from the RTB-cycle, only two moving parts are required. These are the centrifugal compressor and turbine. These turbomachines are precisely balanced and supported by non-contact gas bearings. In combination with a continuous flow-rate of the working fluid, this ensures high reliability, a maintenance-free lifetime, and negligible vibration emittance [12]. Furthermore, all components from the RTBC can work remotely from the other components. The RTBC can, therefore, be integrated easily with the target application. An additional benefit is the remote placement of the cooling load interface. It can be placed at the most strategic location, offering no penalty of the thermodynamic performance of the rest of the cycle on the cooling load. As an example, for space applications the cooling load interface might be placed inside the storage dewar. This eliminates the temperature difference between the RTBC cooling load interface and the bulk cryogenic fluid temperature (e.g. cryogenic propellant),

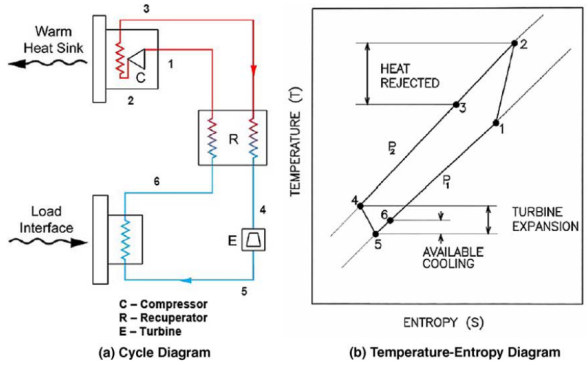

Figure 2.1: Cycle diagram (a) and TS-diagram (b) of a single stage Reverse Turbo-Brayton Cycle [97]

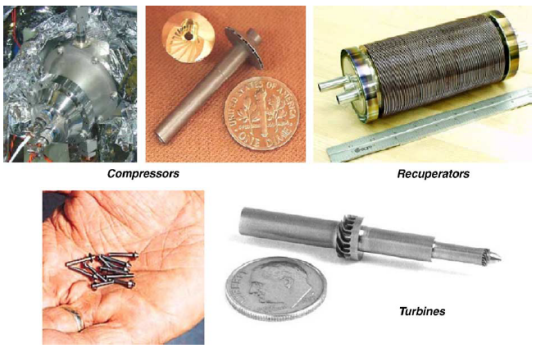

Figure 2.2: Turbo-Brayton components for typical space applications [97]

eliminating an important performance penalty. The connection between a non-integrated cooling load and the bulk fluid could result in a 8.5 K drop due to physical integration losses [77].

Currently, most RTBC are designed for space applications. Recent effort is focused on NASA's intended human exploration missions to Mars. For these human exploration missions to Mars, NASA aims to achieve zero boil-off (ZBO) of the high specific-impulse propellant combinations liquid hydrogen, liquid oxygen and/or liquid methane [78]. Input powers for these cryocoolers are in the order of 1-2 kW, which is an order of magnitude bigger than the first RTBC applications for sensor cooling [100]. For aeronautical applications, however, the order of magnitude increases again to expected input powers in the range of 20-200 kW. The nature of RTBC makes it the perfect cryocooler to scale to higher capacities as required for airborne cryocoolers. RTBC have the ability to transport large amount of heat over significant distances with high conductance [97]. As explained previously in this section, the continuous flow-rate and high heat capacity rate of the working fluid make for an outstanding ability to increase capacity, compared to other cryocoolers. Furthermore, the high power density of rotating turbomachinery make for lightweight and compact components at high capacities relative to other cryocoolers [97].

2.1.2. Turbomachinery

The characteristic component of an RTBC is the turbomachinery. The high power density of these rotating turbomachine parts make for lightweight and compact components at high capacities relative to other cryocoolers [97]. The cooling requirements for earth-satellite space RTBC range from a few Watts to a few hundred Watts [40, 78]. The recent interest of NASA in human exploration to Mars requires increased cooling power, with input powers in the order of 1 to 2 kW [78]. The requirement of these space cryocooler systems have directed development towards miniaturisation of precise turbomachinery components [97]. The typical size of the components of RTBC are shown in Figure 2.2. As a result of this miniaturisation, the operating speeds of the turbomachinery are in the order of 5000 rev/s or 300,000 rpm [97, 100]. This allows for high capacities, whilst delivering compactness and minimising weight. With increased capacity, the overhead losses become smaller and the efficiency increases. Compared to other cryocoolers, the specific mass (mass per cooling capacity) of the RTBC, therefore, decreases with increased capacity [97]. Due to the small scale and high operating speeds of the turbomachinery, radial or centrifugal compressors and turbines are favoured over axial machines [76]. Next to the specific work output due to the aerodynamic forces that both radial and axial turbomachines have, radial turbomachines have a positive contribution to the work due to Coriolis forces. This is independent from the blade profile and dependent upon the meridional streamline shift [76]. This allows radial turbomachines to be compacter than axial machines. Another benefit of using radial turbomachines, is the robustness and therefore its long maintenance-free lifetime [76].

Currently, research efforts are focused on optimisation of the aerodynamic design of rotating and stationary elements of the turbomachinery without compromising its long maintenance-free lifetime and reliability. This is obtained with improved rotor manufacturing techniques utilising 5-axis CNC milling operations and utilising computational fluid dynamics [100]. The optimisation procedure for turbomachines starts with specifying a target aerodynamic efficiency, accompanied by constraints and limits for geometrical parameters such as blade thickness and height, rotor blade inlet and outlet angles, number of blades, length of the diffuser, etc. Using this, the conceptual design is performed with the empirical

relations in the TurbAero design software. The conceptual design is then imported into ANSYS CFX, where the design is iterated to minimise undesirable entropy generation [24]. Additionally, research is performed to enhance motor technology by Hill, Hilderbrand, and Zagarola [45], Acharya et al. [1], and Gong and Habetler [41] to improve net efficiencies. These efforts result in a considerable improvement of turbomachinery efficiency. Early RTBC designs for low-capacity sensor cooling had demonstrated compressor net efficiencies of 35-38% [100, 97], and demonstrated turbine net efficiencies of 60-61% [97, 98]. Recent turbomachinery designed for high-capacity cooling of long-term cryogenic propellent storage in space, show a demonstrated peak compressor net efficiency of 79% [100], and a peak turbine net efficiency of 80% [24].

Additional to the improved aerodynamic and motor performance, research is done to develop fully cryogenic compressors. In RTBC with cooling capacities up to 20 K, the turbine is already operating close to the cooling load temperature, with gas bearings and alternator operating at the same temperature. For cooling loads lower than 20 K, however, a novel technical approach is developed that uses two (or more) RTBC stages. The lowest stage provides the cooling power, and rejects heat at 77 K. This heat rejection can be absorbed by an upper stage of the RTBC, or through liquid nitrogen boil-off [99, 21]. The compressor of the lower stage can operate at cryogenic temperatures, where the density of helium is four times as high as at room temperature. This increases the pressure ratio of a single stage, increasing its power density. Additionally, the increased pressure ratio increases the specific cooling power, decreasing the required helium mass flow rate. This reduces the size of the recuperator and heat exchangers. Most importantly, however, the specific work to compress helium at cryogenic temperatures is decreased significantly. In combination with the lower required mass flow, the input power decreases dramatically. Using this design approach, the size, weight, and input power of the cryocooler are predicted to decrease with at least an order of magnitude [99, 21]. In addition to this research, manufacturing and operational problems such as the use of cryogenic gas bearings are investigated [96, 21]. This is not only needed to enable cryogenic compressors, but can also improve the performance of the turbines.

Unfortunately, no detailed design parameters nor consistent definitions of the characteristic parameters are provided by literature. At the faculty of Aerospace Engineering of the Delft University of Technology, however, research is done on miniature high-speed centrifugal compressors operating with non-standard fluids [35]. Part of this research is the construction of an in-house model for conceptual design of turbomachinery based on Local Dimensionless or Scaling Analysis. The in-house reduced-order model is a python suite relying on the lumped parameters modelling approach. A detailed description of this model can be found in Giuffré, Colonna, and Pini [38]. The philosophy behind the model is to have a fully integrated compressor design process. This is done by incorporating advancements in the conceptual design phase as much as is possible, such that detailed design is only performed once a high-performance feasible design has been developed by the conceptual model. This means that the conceptual design is very close to a working product, and can be improved with e.g. CFD. This is a complete new design philosophy compared to current design methods, which use conceptual design as an indication for a starting point from which a detailed design is constructed. The in-house model shifts the construction of the design as much as possible to the conceptual design, such that time and computational effort is reduced whilst ensuring an optimal design.

2.1.3. Recuperator

Although not the focus of this research, the recuperator is the largest and heaviest component of any RTBC [71]. Creare LLC has been at the forefront of developing high-performance lightweight recuperators for low-capacity space applications. Recently the research focus shifted from low-capacity to high-capacity recuperators for space and aeronautical applications. The highest effectiveness recuperator for high-capcacity space applications had been developed and tested by Deserranno et al. [26]. This micro shell-and-tube recuperator showed an effectiveness above 0.995, for a mass flow rate of 3.6 g/s. This recuperator is designed for a 20 K, 20 W cryocooler.

For aeronautical recuperators, the micro shell-and-tube qualified for NASA space applications might pose size, weight and axial conduction problems. In order to have a more compact core, reduced flow passage size, lighter-weight materials, increased heat transfer, and reduced axial conduction, a novel laminated slotted plate (LSP) recuperator was developed [71]. Testing of the first prototype showed an effectiveness of 0.9885, at a mass flow rate of 1.4 g/s. Future efforts include scaling-up, reducing weight, and switching to more lightweight titanium alloys. It is approximated that the LSP recuperator can reduce the weight of the recuperator with 24% whilst having a similar performance compared to micro shell-and-tube recuperators [71].

2.1.4. Applications of Reverse Turbo-Brayton Cryocoolers

The RTBC has possible applications in 3 main disciplines. These are space applications, aeronautical applications and ground-based High Temperature Superconducting (HTS) transmission cables. A 4th discipline are tactical military applications, such as missile systems, which are not discussed in this thesis due to its complex ethical framework [99].

As of the writing of this thesis, only one RTBC has been fully tested, qualified and implemented into an aerospace (space and/or aeronautical) application. This RTBC was developed by Creare LLC, for the cooling of the Near Infrared Camera and Multi-Object Spectrometer (NICMOS) instrument in the Hubble Space Telescope (HST) [89]. After the original cooling system, which relied on solid nitrogen, was depleted, a new cooling system needed to be installed. This was done in space by astronauts from the Space Shuttle Columbia during the STS–109 mission in March of 2002. The RTBC had a cold load temperature of 77 K and a cooling power of 7 W. The RTBC had a nominal input power of 376 W ($\pm$20W) and a nominal cycle efficiency of 6.2%. It had an operation time of over 45,800 hours, until the NICMOS instrument was set offline in 2008 due to its replacement by the Wide Field Camera 3 [52].

Apart from the only operational RTBC in the HST, multiple space-borne RTBC were designed or are in the design phase for low-capacity and high-capacity applications [84]. These only include low-capacity cryocoolers. Other efforts include high-capacaty RTBC for ground-based HTS transmission cables [16, 56]. However, since the temperature is in the upper range of the cryogenic region (around 77 K) and the systems are ground based and thus not weight-limited, the application is too different compared to low-weight low temperature RTBC. One design was made for airborne RTBC, where a demo-system for the United States Air Force was created [11]. Very little design information is given, and the Carnot efficiency of the demo was just 4%. The design of the system, however, was intended to provide 1 kW of cooling at 95 K with the expected input power of 21-25 kW and an expected mass of 270 kg.

Since no recent high-performing design for airborne RTBC has been made, the research in this report will revolve around the design variables of such system. These include design choices at system level, but also at subsystem level such as the design of the turbomachinery.

2.2. Liquid Hydrogen Tanks for Aircraft

In order to size an RTBC for hydrogen storage in the next generation hybrid/electric aircraft, a preliminary design for a hydrogen tank for the design mission has to be obtained. There is a diverse number of cryogenic tank models in open literature available. Most cryogenic tank design models are for space applications, however, some models exist for aeronautical applications. The purpose of this part of the literature study was to identify a preliminary thermal design model for a hydrogen tank under a high heat load, that is able to incorporate a simple RTBC model. The required outputs of the model are the experienced heat load into the hydrogen mixture control volume (CV), the temperature of the hydrogen mixture, and most importantly the boil-off and vented hydrogen. In addition, the model requires to have input variables such that the design mission can be simulated sufficiently, either by defining the design mission within the model itself or by the use of an external thermal model that simulates the design mission.

The available design models found in literature for cryogenic tank design is elaborated on within this section. All cryogenic tank models can be divided into three categories: theoretical models, analytical models, and numerical models. These models generally do not publish boil-off results, but do include the mechanism of boil-off in the modelling effort. The models in these three categories focus mainly on representing the fluid properties in the tank for pressurisation processes in normal-gravity conditions. Models of boil-off could be added to obtain the required results as needed for this research.

First a brief overview of the available models in literature is given. Hereafter, state-of-the-art models of each of the three classifications are described, after which the most used boil-off models are discussed. It was found that there is not enough data available in literature to size the RTBC and asses its impact. Furthermore, no thermal model in literature was extensive enough nor fulfilled the requirements, so it was decided that a new model was to be developed. The research in this report on the modelling of a cryogenic hydrogen tank will therefore revolve around the assumptions that can be made about the physical processes inside the tank, the mission profile that determines the heat load, and the method of modelling boil-off.

2.2.1. A brief overview of the available models in literature

Cryogenic tanks for aeronautical applications is a new research area. This research is stimulated by the need for a sustainable future aviation fuel. An analysis to estimate the total tank and boil-off mass of hydrogen tanks was developed by NASA in 2002 [18]. In this analysis, one dimensional heat transfer

from the environment to the tank was considered. The boil-off was calculated with an energy balance between the heat flow coming through the insulation, and the energy that is used to boil the liquid hydrogen (the enthalpy of vaporisation).

In 2010, a first preliminary design model for liquid hydrogen tanks onboard aircraft was developed by Verstreate et al. for foam and multi-layer insulation [92]. In this model, conservation of mass is assumed within the tank, and the liquid-vapour mixture is assumed to be in a homogeneous state. This study focused on the gravimetric storage density of liquid hydrogen tanks, and does not provide any information about boil-off characteristics nor heat load into the tank.

More recently, in 2018, a method was developed to model and design cryogenic hydrogen tanks for future aircraft applications [93]. In this study done by Winnefeld et al., the one-dimensional and steady-state heat equation is used to determine the heat flow into the tank. Again, no data about or method to calculate the boil-off was published. The boil-off is used during calculations in the model, as is evident from the different dimensionless parameters that do take the vented mass into account.

In 2021, Mendez Ramos [67] presented a PhD dissertation with a complete overview of cryogenic propellant tank models for space applications. For cryogenic propellant tank modelling and analysis for space applications, the prediction of boil-off is not the primary objective. Although the boil-off process generally is modelled, there are few research papers that publish boil-off results. Instead, the focus is on pressure and temperature trends [67]. Ramos, therefore, aimed to increase the fidelity in the boil-off rate during the initial design phase of the vehicle design of spacecraft. In order to achieve this, a simplified cryogenic tank model was developed. This model is capable of simulating physical processes inside of the tank. The model, however, uses assumptions that do not generally hold and are specific to space applications. Three of the discussed analytical models by Mendez Ramos [67] are elaborated upon in Section 2.2.3, as they are considered state-of-the-art.

2.2.2. Theoretical models: the homogeneous and surface evaporation models

Theoretical models are the simplest means of analysing fluid behaviour inside of cryogenic tanks. It is based on basic fluid and heat distribution theories, and evaluates the tank as a single control volume. The two main theoretical models are the homogeneous model and the surface evaporation model. Both are pressure rise models for closed, non-venting cryogenic tanks undergoing self-pressurisation. These models are not an effort to describe the complicated processes that take place inside of a cryogenic tank, but were developed to compare to experimental data in the 1960s [4]. These models, however, are used in studies for preliminary tank design by Verstraete [92], Lin [61], and Onorato [73]. The homogeneous model in particular has been used as a baseline for other self-pressurisation models, as outlined by Ramos [67]. The homogeneous model generally underestimates pressurisation rates due to its assumption of uniform temperature distribution, whilst the surface evaporation model generally overestimates the pressurisation rate due to its assumption that all heat contributes to the evaporation.

2.2.3. Analytical models: CPPPO, Hastings et al., and TankSIM

Analytical models make use of multiple control volumes to model the heat and mass transfer processes inside of the tank. Compared to theoretical models, they are improved in three ways. First, no assumption is made about the state of the liquid or vapour. This results in the liquid or vapour being able to divert from their saturation states, and be superheated or subcooled. Second, it improves the basic fluid and heat distribution theories with empirical relations and correlations for mass and heat transfer. Third, analytical models include multiple control volumes. With an increasing number of control volumes, the accuracy of analytical models generally increases with the inclusion of more physical processes in the modelling effort. Three models in the space sector are considered state-of-the-art. Two of these models are based on an analytical method developed by Ring [83] for the preliminary design of liquid rocket propellant tanks, making use of thermodynamic relations. These two models are the Computational Propellant and Pressurisation Program (CPPPO) model [20], and a model developed by Hastings et al. [44]. The third model (TankSIM [9]) uses a similar thermodynamic model, but included the implementation of very detailed equations to model physical phenomena in the tank. The three aforementioned state-of-the art analytical models are elaborated upon below.

Analytical model 1: the Computational Propellant and Pressurisation Program (CPPPO)

The CPPPO model is a one dimensional analytic thermodynamic model to calculate pressurisation and cryogenic propellant conditions for liquid rocket propellant tanks. The model uses five 0-dimensional control volumes, or nodes. These are the liquid volume, the gaseous volume, the saturated liquid-vapour surface, the tank wall exposed to the liquid volume, and the tank wall exposed to the gaseous volume. The saturated liquid-vapour surface is infinitely small and allows for heat transfer between the

gaseous volume and liquid volume, and ensures the possibility of surface evaporation. The model was developed for the Ares V Core Stage, Ares V Earth Departure Stage (EDS), and Altair Lunar Lander. All three applications include long storage durations, that require the computation of evaporation, bulk liquid boiling and condensation. The predecessor of CPPPO, ROCETS, was unable to do so [65]. The model includes the possibility to implement a Thermodynamic Venting System (TVS) such as used by the Altair Descent Module [20]. Although the model has a "*reasonable level of fidelity when compared to higher accuracy analytic models and available experimental data*" (Corpening, 2010, p47), the model is not suitable for the use in aircraft applications. The foremost reason is due to the method used to account for the internal tank heat transfer. CPPPO simulates internal heat transfer due to natural or free convection, and makes use of empirically determined heat transfer coefficients obtained from test data from similar systems. Although this is a suitable method to determine the heat transfer rate for the tanks in the Ares V undergoing high g-forces, it is not suitable for aircraft that are mainly in force-equilibrium during cruise.

Heat input accuracy is extremely important to obtain accurate results in cryogenic tank modelling. In 1970 an analysis was performed on a low earth orbit (LEO) experiment, in which it was found that the heat input required an accuracy of less than 5% in order to have the pressure rise rate fall within 1 psia (ca. 7000 Pa) during a 1.5 hour coast phase [10]. With longer duration, such as more than 8 hours for long-range flights, the heat input accuracy becomes even more important in order to accurately model cryogenic tank conditions. It is therefore of great importance that the external and internal heat transfer is modelled correctly. Therefore, if use is made of empirical data for heat transfer coefficients, it is necessary that these data are representative of the application for which the model is made.

Analytical model 2: the model of Hastings et al.

The model of Hastings et al. [44] is, similar to CPPPO [20], a lumped model making use of 0-dimensional control volumes. Hastings makes use of four control volumes, namely the gaseous volume (ullage), tank wall, liquid on the tank wall, and bulk liquid. The tank wall is separated into a section exposed to the liquid volume, and a section exposed to the gaseous volume. The wall adjacent to the liquid is assumed to have the same temperature as the liquid, and is therefore not taken into account in the tank wall model. The gaseous volume is assumed to behave like an ideal gas, and all liquid is assumed to be at saturation conditions. The main difference between CPPPO and the model of Hastings, is the modelling of liquid on the tank wall. This is because in the model of Hastings, a spray bar thermodynamic vent system (TVS) is modelled. The TVS mixes and pumps liquid propellant to a spray bar, which sprays cold propellant droplets in throughout the gaseous volume to reduce the ullage temperature and pressure. Part of these droplets also hit the tank wall in this process, creating the need to have a control volume to model the boiling of liquid on the tank wall. The heat transfer dominant in the model is free convection, but forced convection is used to determine the heat transfer of the liquid droplets sprayed in the ullage.

The model of Hastings et al. predicts tank conditions within a conservative margin, over-predicting pressurisation rates with a factor between 2 and 5 [67]. This over-prediction could be due to the assumption that the liquid is an incompressible saturated liquid. With this assumption, the liquid is assumed to be in state of constant bulk boiling. In reality, the liquid can be subcooled if the saturation temperature rise is greater than the rise in liquid temperature. When the liquid pressure is increasing, the liquid saturation temperature increases accordingly. If the heat input to the liquid is small, the rise in liquid temperature can be less than the rise in saturation temperature induced by the pressurisation rate. This lets the liquid temperature fall below the liquid saturation temperature, subcooling the liquid and stopping the bulk boiling. The assumption that the liquid is always saturated therefore over-estimates the boil-off, and hence the pressurisation rate.

Unfortunately, the model of Hastings et al. is not suitable for the intended modelling of the cryogenic hydrogen tank for aircraft as intended. The tank being researched in this paper does not have a spray bar TVS, making the model of Hastings et al. over-complicated for this application. Most importantly however, the assumption of saturated liquid would not hold if the liquid is actively cooled to a non-saturated state with a cryocooler as is the intention of this research.

Analytical model 3: Tank System Integrated Model (TankSIM)

The third model, TankSIM [9], is like the other models, a lumped 0-dimensional control volumes model. It is based on thermodynamic conservation equations of mass and energy, but uses correlations for mass and heat transfer. It uses 7 control volumes, and 13 model nodes. TankSIM, to which Hastings also contributed, can model the same application as the model of Hastings et al. [44], and more. It can model direct venting of the ullage, a spray bar TVS, and an axial jet TVS. It is a very detailed and extensive model that can be used for Mars and Lunar exploration, asteroid and near-Earth objects

rendezvous, as well as ground based vacuum testing. The model can simulate various stages of long-duration space missions in any succession sequence, and can handle flat, spherical and elliptical tank geometries. Compared to the simpler model of Hastings at al., it models experiments with much more accuracy.

Due to the amount of detail and the accuracy for modelling long duration space missions, TankSIM is inherently not suitable for conceptual modelling of cryogenic propellant tanks for aircraft. The amount of assumptions on not-known variables, the adaption from space to aeronautical application modelling, and the computational cost of the detailed model make it unsuitable to use. The adaptation of the model to aeronautical application modelling is left for another study, when the conceptual design is performed and the design space is narrowed down.

2.2.4. Numerical models

Numerical models are the most detailed and extensive models for analysing fluid condition in cryogenic tanks. There are numerous models available in literature that can simulate cryogenic tank self-pressurisation and active phases in space missions, such as thrust firing of rocket engines [67]. Two distinction can be made in numerical models, that is Network Flow Analysis (NFA) and Computational Fluid Dynamics (CFD) methods. Both type of models are very detailed and can model the complicated physical phenomena occuring in cryogenic tanks accurately [67].

Numerical methods are very costly in computational effort. With high performing processors, both NFA and CFD have a computational cost in the order of hours per simulation [63, 66]. Due to this computational efforts, numerical simulation can only be performed for the modelling of short parts of a mission. Additionally, one would want to use numerical models when the design of the tank is fully specified. For the intended research in this paper, therefore, numerical models are not suitable. For the intended conceptual design of long duration aeronautical missions, the computational costs of all runs could very well extend the duration of the intended research in and by itself.

2.2.5. Boil-off models

The majority of the cryogenic tank models found in literature use one of two boil-off models. These two methods are described in this section.

The first, and most common method to calculate the boil-off is that of dividing the heat transfer rate by the enthalpy of vaporisation. The boil-off mass flow rate is calculated by Equation (2.1), where $\dot{Q}$ is the heat transfer rate, and h_{vap} is the enthalpy of vaporisation of the cryogenic fluid. Generally when using this method, the system is assumed to be steady-state, and the two-phased cryogenic fluid is assumed to be saturated and in equilibrium. In addition, the boil-off is assumed to be minimal so that the fuel quality does not change, and the internal convective heat transfer coefficient is constant.

$$\dot{m}_{\text{boil-off}} = \frac{\dot{Q}}{h_{\text{vap}}} \tag{2.1}$$

The primary concern of using this simple method is that the results are conservative. In 1969, experiments were conducted by the Lewis Research Center, where a 56cm diameter spherical tank was subjected to venting tests and compared to the theoretical method as stated by Equation (2.1) [5]. The results were that the use of the theoretic model resulted in errors in predicted mass loss up to 600%, compared to the experimental data. It was found that this was primarily due to not accounting for the superheating of the vapour. In the experiments, it was found that the vapour absorbs heat faster than the internal mass and heat transfer processes can distribute it. The result is that the vapour is superheated, absorbing a large amount of the total heat transfer. For hydrogen at 3.45 bar, the enthalpy of vaporisation is approximately the same as the absorbed energy that superheats 1 pound (0.45 kg) of vapour 33 K. Superheating of the vapour thus significantly decreases the boil-off. Additionally, during the venting of superheated vapour, the energy leaving the system is higher compared to non-superheated vapour venting. It was found that the heating configuration affected the amount of vapour superheat the most. The theory over-predicted the mass loss due to venting by a factor of 2 during uniform heating. During top heating, the theory over-estimated the mass loss due to venting by a factor of 6. In the study, a homogeneity factor was defined. This factor is the change in system entropy during testing divided by the change in system entropy predicted by the theoretical homogeneous model. The factor for the testing results in shown in Figure 2.3, which shows that the heating configuration is the most important variable affecting the final state of the system.

The second method to calculate boil-off is by indirectly calculating the mass flow rate from the liquid to the vapour in order to attain a certain pressure rise. The method is derived from the perfect gas law. It uses a proposal from Elliot Ring, which states that boiling occurs when the pressure is lower than

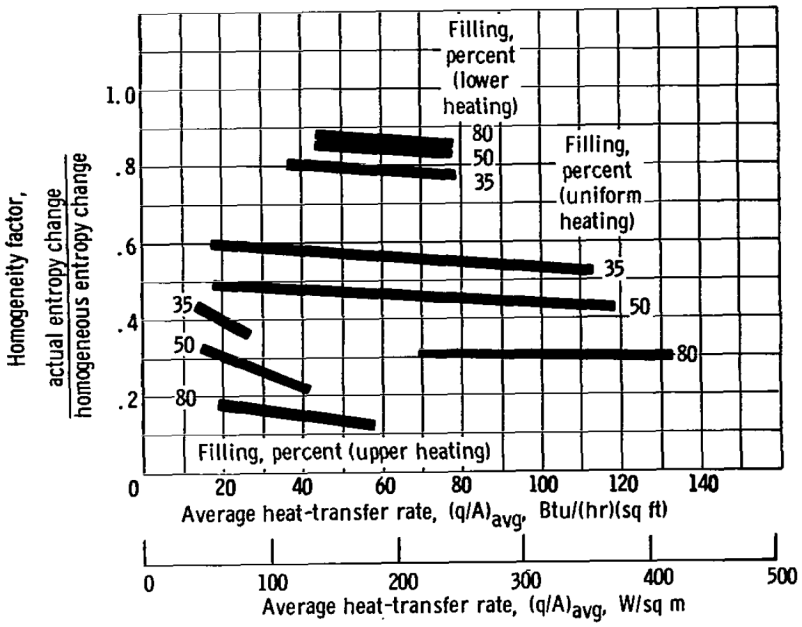

Figure 2.3: Homogeneity factor as a function of average heat transfer rate [4]

the vapour pressure of the liquid at that temperature [83]. The boil-off rate is then calculated by the needed pressure rise to reach the vapour pressure as stated in Equation (2.2). In this equation, P_{v_l} is the vapour pressure of the liquid, P_g and V_g are the pressure and the volume of the gaseous volume respectively, T_l is the temperature of the liquid, R_l is the specific gas constant of the evaporated liquid, and dt is the change in time [20].

$$\dot{m}_{\text{boil-off}} = \frac{(P_{v_l} - P_g)\, V_g}{R_l T_l dt} \tag{2.2}$$

The main concern of this method is the use of the ideal gas assumption. For evaporated cryogenic hydrogen, the vapour consist of gaseous para-hydrogen. At low temperatures, gaseous para-hydrogen does not behave as an ideal diatomic gas [42]. Many quick and simple analyses to check for ideal-gas behaviour of hydrogen (and other gasses) is done by simply using real-gas values obtained from databases in equations such as the equation for the pressure ratio in an ideal isentropic expansion. These equations are derived by assuming a calorically and thermally perfect gas, which does not hold for real-gas behaviour. Using these equations can result in misleading results. For low temperature gaseous para-hydrogen, the pressure, density and temperature ratios for an isentropic expansion to Mach = 1 can deviate from ideal gas behaviour by respectively 8, 4 and 10 percent [42].

Additionally, using the same analogy as the concern of the method described by Equation (2.1), results could be extensively over-estimated. If any assumptions on heat transfer are made that incorrectly model super-heating of the gaseous volume, this method is especially sensitive as it uses the pressure of the gaseous volume directly. If the super-heating of the gaseous volume is not properly calculated, the gaseous pressure can deviate enormously and the boil-off results will be wrong.

3

Methodology

This chapter describes the methodology followed in the research. It entails descriptions of both design and modelling methodology. To fulfil the research purpose, a Reverse Turbo-Brayton Cryocooler model and a cryogenic liquid hydrogen tank model for the active cooling of the hydrogen tank in the Flying-V are developed and tested. Moreover, to demonstrate the performance of the turbomachinery, a detailed conceptual design of the centrifugal compressor is made.

The methodology followed in this research is the 9-step method as thought by Prof. dr. ir. Piero Colonna in the course AE4263 Modelling, Simulation and Application of Propulsion and Power Systems at the Faculty of Aerospace Engineering of the Delft University of Technology (Colonna et al. [17]). The 9 steps in the method are defined by the:

1. Purpose
2. System border and variables
3. Relevant phenomena
4. Hypotheses and assumptions
5. Sub models
6. Conservation laws and constitutive equations
7. Simplifications
8. Implementation
9. Simulation, Validation, Documentation and Application

The first 5 steps complete the conceptual model of the problem. Steps 6 and 7 create the mathematical model, and then finally steps 8 and 9 build the numerical model. With this method, a comprehensive model can be made. The operation of completing the 9 steps in the 9-step method is an iterative process. As a result, if errors are found in the verification and validation or new insights are brought to light during the creation of the model, some or all steps need to be reconsidered or redone. Especially when a model is the first in describing a system, which is the case in this research, multiple iterations need to take place to build an accurate model.

This chapter starts with a description of the physical representation of the modelling problem in Section 3.1. In Section 3.2, the modelling methodology of the liquid hydrogen fuel tank is presented. In Section 3.3, the design and modelling of the Reverse Turbo-Brayton Cryocooler system model and the conceptual compressor is discussed. The verification and validation of the models are presented in Section 3.4. Lastly, the connectivity between the designs and models are discussed in Section 3.5.

3.1. Physical Representation of the Modelling Problem

In order to accurately model a complex system, machine or component, it is of extreme importance to have a good understanding of its physical representation. This understanding helps throughout each of the steps in the 9-step method, makes the problem and final model comprehensible, and helps in formulating conclusions about the modelling results. Two models are developed in this research, a Reverse Turbo-Brayton Cryocooler model and a cryogenic liquid hydrogen tank model for the active cooling of the hydrogen tank in the Flying-V. The physical representation of the latter is presented in Section 3.1.1, whilst the physical representation of the first is described in Section 3.1.2.

3.1.1. Physical Representation of the Liquid Hydrogen Fuel Tank

To create a theoretical model of a liquid hydrogen fuel tank for long range flight, a good understanding of the physical system is required. The application for which the model was created is the Flying-V concept, developed at the Delft University of Technology. Woensel [94] has performed an integration study of a liquid hydrogen fuel tank into the concept of the Flying-V, which is henceforth considered as the application. A visualisation of the liquid hydrogen fuel tank within its application is shown in Figure 3.1. To aid with visualisation, the Flying-V is shown in Figure 3.2. The Flying-V is a flying wing aircraft concept under study at the Delft University of Technology. The wing has a dual function, namely serving as wing ánd as fuselage. The original concept, in collaboration with Airbus and financed by KLM, promises a reduction of 20% in fuel burn compared to a conventional reference aircraft (A350-900) having the same flight mission and capacity. This is assuming current engine technology and manufacturing techniques [8].

One of the research done on the Flying-V was an integration of a liquid hydrogen fuel tank, to asses the effect on mission performance and the implications on the fuel system [94]. The fuel tank proposed in the research is an integral tank in the aft of the wing sections. This makes the fuel tank structure carry the loads of the wing structure, in addition to the loads resulting from its function as cryogenic fuel tank. This results in higher volumetric efficiency, which is needed for the liquid hydrogen storage. The effect hereof is that the outer tank wall is exposed to the environment in flight, and that a layer of insulation is needed on the inside of the tank wall. In addition, the tank follows the elliptical shape of the fuselage which prohibits the use of pressure resistant shapes such as a sphere or cylinder.

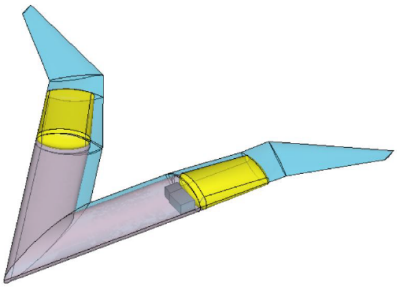

Figure 3.1: Isometric view of the liquid hydrogen fuel tank (yellow) inside the Flying-V [94]

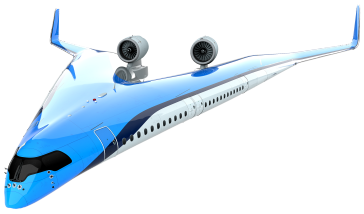

Figure 3.2: Isometric view of the Flying-V[1]

The environment acting on the tank is different for each phase of flight, might develop over the duration of a flight phase and can vary per flight. The tank experiences external convection and radiation, conduction through the tank wall, and internal convection and radiation. The external convection is not only dependent on environmental conditions, but also on flight conditions and the boundary layer propagation over the wing. The external radiation can depend on the environment (e.g. cloudy or sunny), the location of the sun depending on the time and day of the year and geographical location, and the amount of albedo radiation it receives from the ground (e.g. clouds, sea, and mountains all differ in albedo radiation). In addition, the tank wall radiates heat towards the environment. The internal convection and radiation is dependent on the local wall temperature, the local mixture phase, and the local thermodynamic state of the mixture. This makes the thermodynamic problem, in addition with active cooling, complex.

The hydrogen inside the tank is a low pressure two-phased mixture, with the liquid being at cryogenic conditions. A venting system is present to ensure that the tank pressure does not exceed the maximum pressure. Additionally, liquid hydrogen is depleted from the tank to serve as fuel in the aircraft engines. Depending on environmental and cooling conditions and the amount of hydrogen depleted from the tank, the liquid hydrogen can evaporate or the gaseous hydrogen can condensate. The conditions inside of the tank are, therefore, dynamic.

To complete the physical problem, a connection between the internal and external condition is present. This connection is the heat transfer between the tank wall and the two-phased hydrogen mixture, which is where the main effort of cryogenic fuel tank models resides (see Section 2.2.3). The heat transfer coefficient differs per radial location, and is dependent on environmental and internal conditions. The resulting total system is therefore dynamic and highly complex.

[1] Obtained from `https://www.tudelft.nl/lr/flying-v`

3.1.2. Physical Representation of the Reverese Turbo Brayton Cryocooler

To create a model for the Reverese Turbo Brayton Cryocooler, a good understanding of the physical system is required. In Section 2.1 the components and characteristics of the RTBC are discussed. Only one RTBC has been fully tested, qualified and implemented into an aerospace application [89]. The RTBC considered in this thesis research, however, has a capacity that is multiple magnitudes bigger. A NASA innovation research from 2016-2018 proposed a Cryocooler for MgB2 Superconducting Systems in Turboelectric Aircraft [95]. The research finished at TRL4, and includes a system-layout, size, and mass estimation. Moreover, the capacity is of the same order of magnitude as considered in this thesis research. As seen in Figure 3.3, the cryocooler consists of a warm module, a cold module in a vacuum canister, and a module containing the power and control electronics. The warm module consists of the compressor(s) and the heat sink. The cold module incorporates the turbine, cooling load heat exchanger, and recuperator. The complete system has a mass of 304 kg, a length of 203 cm and a height of 102 cm. Due to the absence of data on other RTBC systems of the same scale, it was decided that the design in Figure 3.3 is taken as the reference design for the RTBC. Using the weight and dimensions of the reference design, definite conclusions can be drawn about the feasibility of using RTBC to cool liquid hydrogen fuel tanks. The cooling power of 800 W at 20 K might not be the optimal requirement for the cooling of the liquid hydrogen fuel tank, but provides a suitable starting point for design exploration from which further research can be conducted.

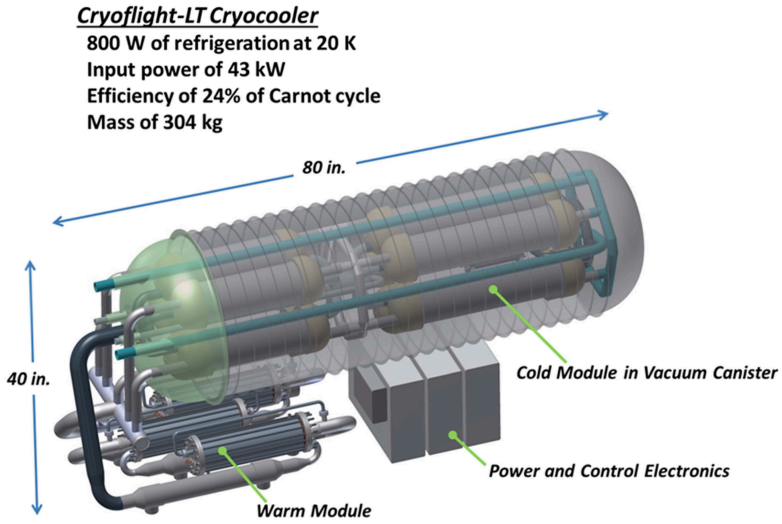

Figure 3.3: Briefing Chart image of the Cryocooler for MgB2 Superconducting Systems in Turboelectric Aircraft [95]

3.2. Modelling Methodology of the Liquid Hydrogen Fuel Tank

The purpose of modelling the liquid hydrogen fuel tank, is to show the potential of active cooling of an airborne liquid hydrogen fuel tank for long range flight. As discussed in Section 2.2, no existing model in open literature satisfies the requirements for this research. A new model was therefore created. This model can be used for the conceptual design and modelling of liquid hydrogen fuel tanks in long range aircraft with and without active cooling, in order to minimise boil-off. The subsections in this section describe the methodology of the model, and follow the 9-step method stepwise from step 2 throughout step 8.

3.2.1. Definition of the system model

In order to correctly model the liquid hydrogen fuel tank, it is important to precisely define the system model with its boundaries, known inputs, unknown outputs, and internal and external variables. A 3D and 2D visualisation of the system model can be found in Figures 3.1 and 3.4. The boundary of the model is the outer tank wall. As the model developed in this research consists of over 2076 variables and parameters, they are not individually described in this report.

An important part of the system model definition is defining the type of problem to be modelled, as this will determine if the System of Equations (SoE) consists of algebraic equations or differential-algebraic equations. In order to define the type of modelling problem, the model requirements are

needed. From the purpose and intended use of the model, it follows that the model needs to:

- be easy to use without knowing detailed design parameters;
- be non-computational expensive;
- capture the dynamics of the physical phenomena occurring in the tank;
- model on- ánd off-design;
- have the ability to include active cooling;
- correctly model boil-off and venting.

The requirement to use the model for conceptual design without knowing detailed design parameters, puts the problem in the macroscopic category (finite Control Volumes (CVs)). Modelling microscopic phenomena require the design to be beyond the conceptual phase. Since the intended use of the model is the conceptual design phase, the use of tools for microscopic phenomena such as detailed Computational Fluid Dynamics (CFD) are excluded. Furthermore, the requirement to model dynamic behaviour in on- ánd off-design requires a dynamic, modular, hierarchically structured, a-causal declarative model, which results in a system of Differential Algebraic Equations (DAEs).

3.2.2. Modelled phenomena and Control Volumes

Cryogenic storage is a complex discipline of engineering. To fully understand the phenomena occurring in a cryogenic tank during extended storage, numerous analytical, numerical and experimental studies have been performed [67]. The main difference between cryogenic storage models is the level of sophistication in the interpretation, inclusion and prediction of these phenomena. An overview of the phenomena that influence mass and energy transfer has been carefully documented by Mendez Ramos [67]. The current subsection discusses the manner in which the relevant phenomena are included, and the control volumes in which and over which the phenomena occur.

The basis for the tank model are the conservation equations for energy and mass. Phenomena not influencing these conservation equations are not considered. To aid understanding of the phenomena influencing mass and energy conservation, a schematic of all mass and energy transfer is shown in Figure 3.4. The definition of each variable in the diagram is stated in Table 3.1. Only two variables are known and taken as input to the model, i.e. $\dot{Q}_{int}$ and $\dot{m}_{fuel}$. All other variables are the unknowns of the mathematical problem, and are the outputs of the model. In total, 11 plus 2 control volumes are considered. The first control volume is the gaseous hydrogen, from hereon referred to as the vapour. The second control volume is the liquid hydrogen, from hereon referred to as the liquid. The third control volume is a infinitely thin saturated surface layer, consisting of no mass. This surface layer is used to calculate the evaporation and condensation at the liquid-vapour interface, as is commonly done in literature [67, 9, 20, 83]. The wall is constructed from 8 segments of 45° each, spanning the whole 360°. Each wall segment is modular build according to the layers of different material present in the geometric tank design, resulting in extra control volumes (see Section 3.2.4). For sake of simplicity, the 8 control volumes (with internal control volumes) of the wall are referred to as the wall. In addition, two end caps on either side of the tank make for an extra two control volumes. The end caps are not numbered in Figure 3.4, as it is a cross-sectional view.

To develop the conceptual physical model, a decision must be made about which phenomena is relevant and which is negligible. Additionally, the model must be adequate for the conceptual design stage. In all cases, the principle of parsimony must be applied. To provide a clear overview, the phenomena are split into four categories: phenomena related to the wall, the liquid, the vapour, and the surface layer. All phenomena are displayed in Figure 3.5, where the phenomena above the line in each text-box are modelled (relevant), and the phenomena below the line in italics are omitted in the model. Next to negligible phenomena being omitted, some phenomena are omitted due to the in-ability to include them into the conceptual model for various reasons as discussed below.

The wall experiences external convection and radiation to the outside environment, which are included by using an external environment model. Heat is conducted throughout the internals of the wall, consisting of structural materials and insulation, which is relevant for the model. Due to the tank being cryogenic, the outer wall temperature can be cooled down substantially depending on the insulation used. Frost formation from liquid air droplets can form on the tank wall, which can have impact on the aerodynamic performance of the aircraft if the tank wall is also the outer wall. Although the outer skin of the Flying-V also acts as the tank wall, this phenomena is omitted as it only starts occurring when temperatures of the outside wall drop below 108 K [62].

The liquid experiences convective and radiative heat transfer with the wall it is in contact with. Additionally, bulk boiling can occur when the liquid is in saturation. As the model is a fuel tank with internal

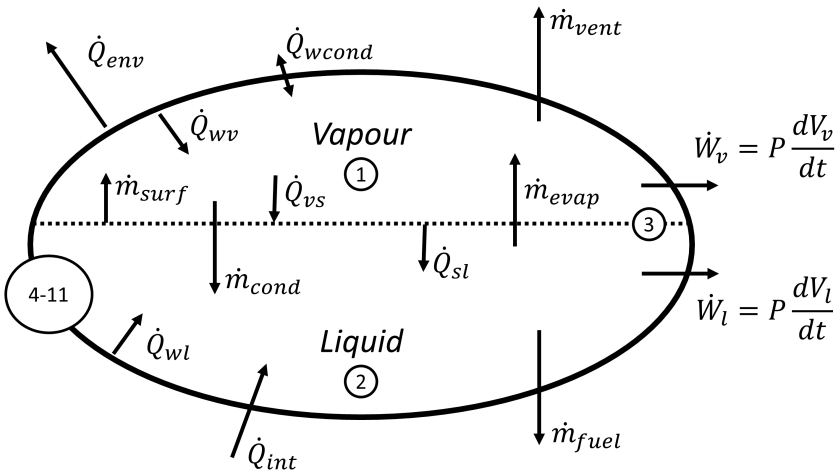

Figure 3.4: Diagram of all mass and energy transfers of the liquid hydrogen fuel tank, including the numbering of all CVs except the end caps

Table 3.1: Definition of the mass and energy transfer variables in Figure 3.4. The variables $\dot{Q}_{int}$ and $\dot{m}_{fuel}$ are known inputs, all other variables are the unknown outputs of the mathematical problem

Variable	Definition	Unit
Heat transfer		
$\dot{Q}_{wv}$	Heat transfer rate from the wall to the vapour	W
$\dot{Q}_{wl}$	Heat transfer rate from the wall to the liquid	W
$\dot{Q}_{vs}$	Heat transfer rate from the vapour to the surface layer	W
$\dot{Q}_{sl}$	Heat transfer rate from surface layer to the liquid	W
$\dot{Q}_{wcond}$	Heat transfer rate that conducts through the wall segments	W
$\dot{Q}_{env}$	Heat transfer rate from the wall to the environment	W
$\dot{Q}_{int}$	Heat transfer rate introduced directly into the liquid from sources other than the wall	W
Mass transfer		
$\dot{m}_{evap}$	Liquid evaporation mass flow rate	kg/s
$\dot{m}_{cond}$	Vapour condensation mass flow rate	kg/s
$\dot{m}_{surf}$	Surface evaporation/condensation mass flow rate	kg/s
$\dot{m}_{vent}$	Vapour venting mass flow rate	kg/s
$\dot{m}_{fuel}$	Liquid fuel mass flow rate	kg/s
Fluid work rate		
$\dot{W}_v$	Vapour rate of work	W
$\dot{W}_l$	Liquid rate of work	W

cooling, both fuel flow and internal cooling towards the liquid is included in the model. Conversion of para- to ortho-hydrogen (and vice-versa) is neglected, as no viscosity model exists for para-hydrogen,

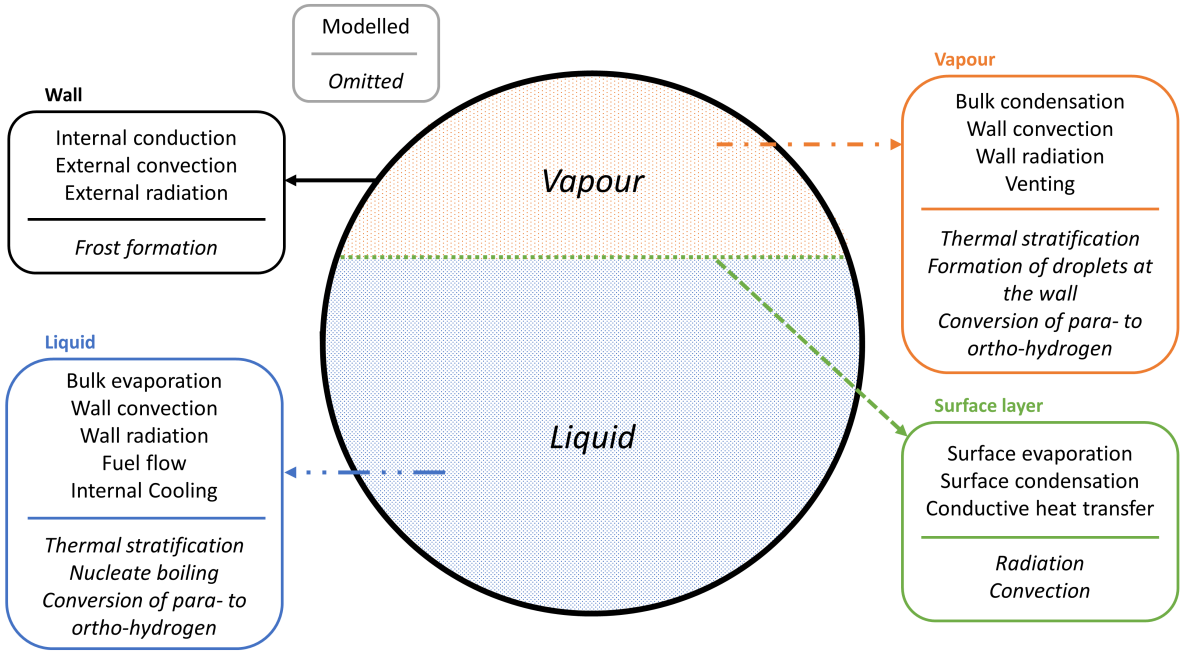

Figure 3.5: Diagram of all phenomena occurring in the liquid hydrogen fuel tank. Above the line in each text-box are the modelled phenomena, below the line in italics are the phenomena omitted in the model

and no viscosity and thermal conductivity model exist for ortho-hydrogen in the fluid models available in the CoolProp library (Section 3.2.6). Instead, equilibrium hydrogen is used of which approximately 75% is ortho-hydrogen and 25% is para-hydrogen, which is normally the case for temperatures above 223 K. At cryogenic temperatures, however, the hydrogen composition is close to a 100% para-hydrogen composition. At higher temperatures, the para-hydrogen is converted into ortho-hydrogen which can take up a significant amount of heat. Especially between 50-200 K, this conversion of its nuclear spin should not be neglected [91]. Due to inability of the fluid model to model this, however, this phenomena is neglected. Stratification in the liquid is also neglected, as increased tank capacity increases the time to fully develope stratification [67], and it significantly increases the complexity of the model. Possible inclusion of stratification would require detailed experimental data of the tank, or a significant increase in control volumes which increases the complexity of the model considerably. Moreover, due to the high-heat input the liquid is expected to be in a fully (boiling) saturated state, or due to cooling the liquid is expected to have a homogeneous temperature. In both cases, no stratification can occur. Lastly, nucleate boiling, i.e. the formation of vapour bubbles at the wall, is neglected. Inclusion would increase complexity of the conceptual model, and require details of local parasitic heat flows or imperfections at the tank wall.

The vapour experiences convective and radiative heat transfer with the wall it is in contact with. Similarly as the liquid, bulk condensation can occur when the vapour is in saturation. As active pressure control is included by means of venting, a venting mass flow is included in the model. Likely as for the liquid, conversion of para- to ortho-hydrogen is not modelled. Thermal stratification is also neglected, as it would require detailed experimental data of the tank or a significant increase in control volumes which increases the complexity of the model considerably. Lastly, formation of dew droplets at the wall is neglected, as it would increase the model complexity without adding significant benefits.

At the surface layer, evaporation of the liquid or condensation of the vapour can occur. Both are taken into account, depending on the heat transfers between the vapour, liquid and surface layer. As no relations for heat transfer at a liquid-vapour interface in a finite volume exists, a conduction model is used as proposed by Bolshinskiy et al. [9]. This neglects the radiative and convective heat transfer. Experimental research by Aydelott [4] indicates that conduction could indeed be the primary form of energy exchange at the liquid-vapour interface of liquid hydrogen storage. Note that the infinitely thin saturated boundary layer accounts for stratification close to the interface.

3.2.3. Assumptions

In Section 3.2.2, a decision was made about which phenomena to include in the model in order to reduce complexity. The complexity of these remaining phenomena, however, is infinitely high in reality.

To simplify the phenomena, hypotheses and assumptions are formulated. The purpose is to simplify the model such that it can be used during conceptual design, i.e. without knowing every detailed parameter of the design and without using much computational effort and cost. Assumptions are known to hold (within the modelled phenomena), whilst hypotheses must be verified. The assumptions applied to the model are divided into assumptions related to thermodynamics, heat transfer, and mass transfer. One hypothesis is formulated regarding the heat transfer through the wall, which will be verified in Section 4.4. All assumptions and hypotheses are listed below.

Thermodynamic assumptions:

- The liquid volume is modelled as a one- or two-phased mixture, depending on whether vapour bubbles are present.
- The vapour volume is modelled as a one- or two-phased mixture, depending on whether dew droplets are present.
- An infinitely thin saturated boundary layer between the liquid and vapour volume exists, having no mass.
- The liquid volume is a single CV with one thermodynamic state.
- The vapour volume is a single CV with one thermodynamic state.
- The thermodynamic state of the vapour leaving the tank is equal to the thermodynamic state of the vapour inside the tank during venting.
- The thermodynamic state of the liquid leaving the tank is equal to the thermodynamic state of the liquid inside the tank during fuel usage.
- Only the liquid volume is cooled by the RTBC.

Heat transfer assumptions:

- The tank is assumed to be symmetric and in equilibrium in axial directions, so no axial conduction is assumed.
- A wall segment exposed to both the liquid and vapour has one temperature, but transfers heat to both the liquid and vapour through the area exposed to the corresponding fluid state.
- The heat transfer to the saturated surface layer is assumed to be pure conduction, as no correlations for liquid-gas interface heat flow rates in a finite volume exist [9].
- Hydrogen gas is transparent for thermal radiation [91].
- Natural convection is modelled using dimensional analysis (Buckingham-Pi theorem).
- During the duration of the flight, the velocity fields inside the tank are small and do not generate any forced convection.

Mass transfer assumptions:

- Venting is immediate and continuous for pressures above the venting pressure.
- The propagation of bubbles and dew throughout the liquid and vapour volume is not modelled in detail, but a time constant is used for stable simulation.

Thermodynamic hypothesis:

- No transverse conduction occurs in the wall, due to the small temperature differences between the segments.

In the following sections, the assumptions and hypotheses are restated to explain their usage to construct corresponding equations for the model components.

3.2.4. Sub models

The liquid hydrogen tank model is decomposed into sub models. Each sub model is carefully selected to reduce the tank model complexity. The division of the model into hierarchically structured sub models is done using a modular approach, carefully defining the sub models such that it allows for reusability for future novel model developments. In order to decompose the system model effectively, the sub model borders are chosen at the system boundaries such that accumulation of conserved variables can be defined and variables can be averaged. This modular approach distinguishes the developed model from state-of-the-art models in literature, as these models are tailored to specific applications and cannot be used for other applications due to the nature of their model setup.

Following this approach, the liquid hydrogen tank system model is decomposed into 4 hierarchically structured layers containing 8 unique sub models, 9 unique components and 5 unique standard library components. The differentiation between sub models and components is made by their hierarchy: a sub model can contain components and/or sub models, whereas a component contains a system of equations. The distinction between sub models and sub sub models etc. is not made to prevent tediousness. The unique sub models, non-standard library components and standard library components are listed in Tables 3.2 to 3.4. The 4 hierarchically structured layers are shown in Figures 3.6 to 3.10.

Table 3.2: Sub models used in the liquid hydrogen fuel tank model

Sub models
1. Integrated Liquid Hydrogen Tank
2. Tank Pressure Controller
3. Tube Tank Section
4. Dome Tank Section
5. Fuselage/Tank Tube Wall Structure
6. Fuselage/Tank Dome Wall Structure
7. Tube Tank Insulation Structure
8. Dome Tank Insulation Structure

Table 3.3: Non-tandard library components used in the liquid hydrogen fuel tank model

Non-standard library components
1. Environment
2. Hydrogen Mass Flow
3. Two-Phased Hydrogen Mixture Container
4. Reverse Turbo-Brayton Cryocooler
5. External Convection
6. Wall Radiation
7. Solar Radiation
8. Tube Conduction
9. Dome Conduction

Table 3.4: Standard library components used in the liquid hydrogen fuel tank model

Standard library components
1. Pressure Sensor
2. Massflow Sensor
3. Integrator
4. Add
5. Real Expression

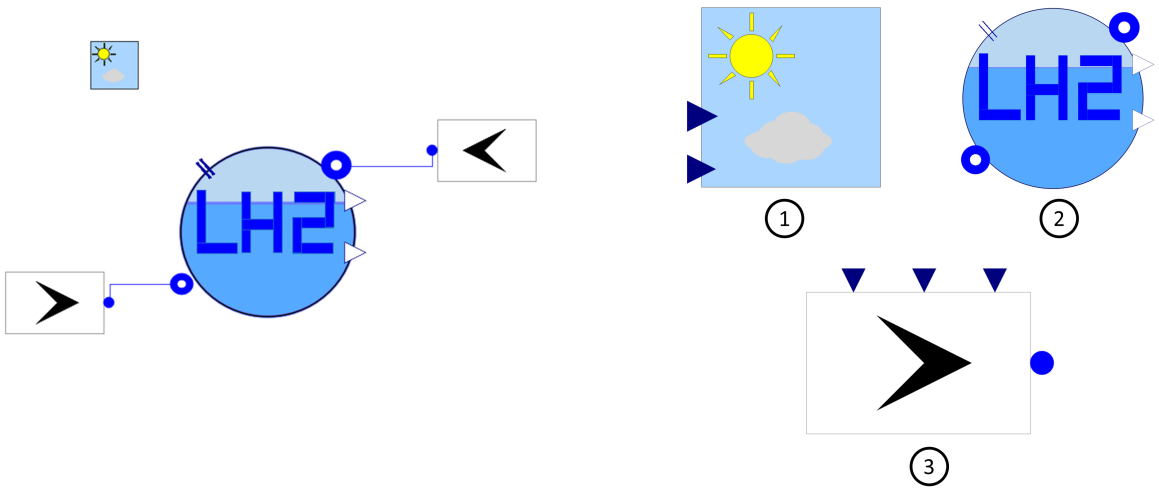

Figure 3.6: The first hierarchical layer with corresponding sub models and components. The first hierarchical layer (the system) is shown on the left, and the corresponding numbered sub model and components on the right. The environment component is denoted by number 1, the integrated liquid hydrogen tank sub model by number 2, and the hydrogen mass flow component by number 3.

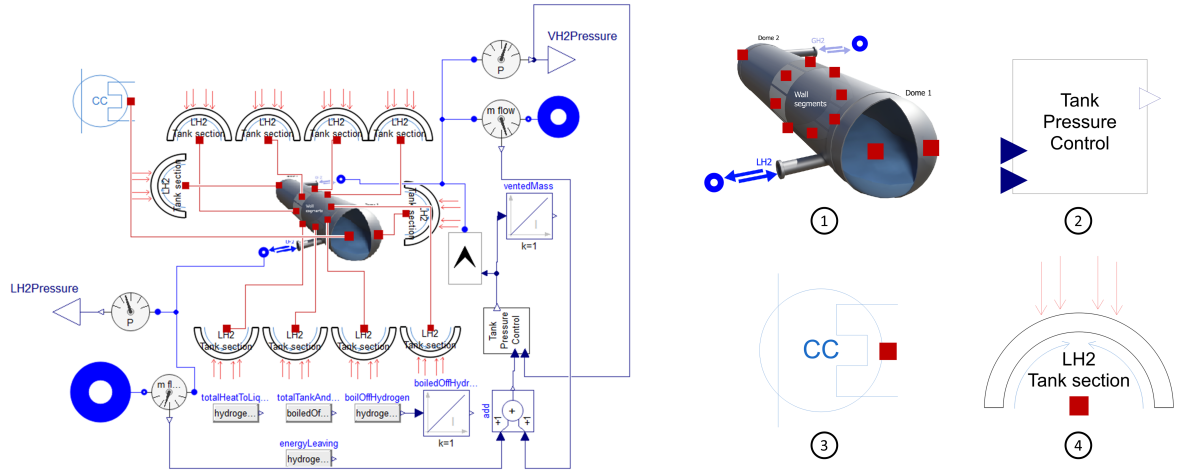

Figure 3.7: The second hierarchical layer with corresponding sub models and components. The second hierarchical layer (subsystem 1) is shown on the left, and the corresponding numbered sub model and non-standard library components on the right. The two-phased hydrogen mixture container component is denoted by number 1, the tank pressure controller sub model by number 2, the Reverse Turbo-Brayton Cryocooler component by number 3, and both the tube and dome tank sub models by number 4.

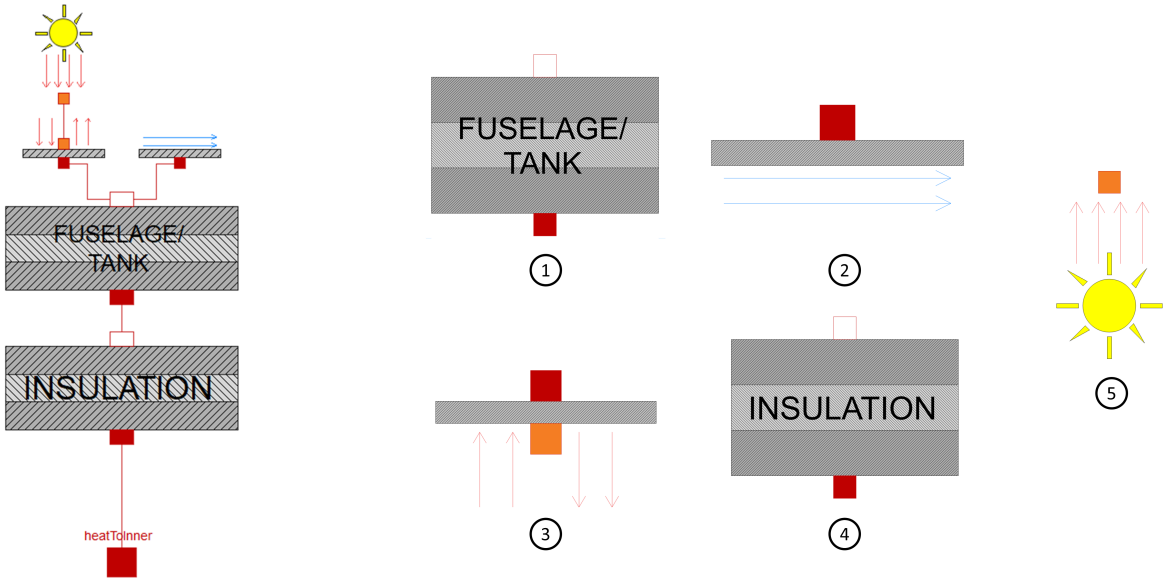

Figure 3.8: The third hierarchical layer with corresponding sub models and components. The unique part of the third hierarchical layer (subsystem 2) is shown on the left, and the corresponding numbered sub model and components on the right. The fuselage/tank wall structure sub model is denoted by number 1, the external convection component by number 2, the wall radiation component by number 3, the tank insulation structure sub model by number 4, and the solar radiation component by number 5. Sub models 1 and 4 can be both filled by either the tube structure or dome structure sub models to create the 8 tube tank and 2 dome tank sections.

The first hierarchical layer, also the system, the model, or the system model, is shown in Figure 3.6. It consists of two unique components and one sub model. Number one in the figure denotes the environment component. This environment component is linked to the Simple Model of the Atmospheric Radiative Transfer of Sunshine (SMARTS) computer program, that calculates the solar radiation on the tank. The integrated liquid hydrogen fuel tank sub model is denoted by number 2. Component 3 denotes the hydrogen mass flow component, that is connected to the fuel and venting ports of the integrated liquid hydrogen tank.

The second hierarchical layer, also subsystem 1, is the integrated liquid hydrogen tank sub model as denoted by the number 2 in Figure 3.6. It is shown in Figure 3.7. It exists of 1 sub model and 3 components, with additional standard Modelica library components and the hydrogen mass flow component from Figure 3.6. The standard Modelica library components are used to facilitate easy result analysis, and provide information to the pressure controller. The sub model at the centre of the hierarchical layer is the two-phased hydrogen mixture container component, denoted by number 1. The tank pressure

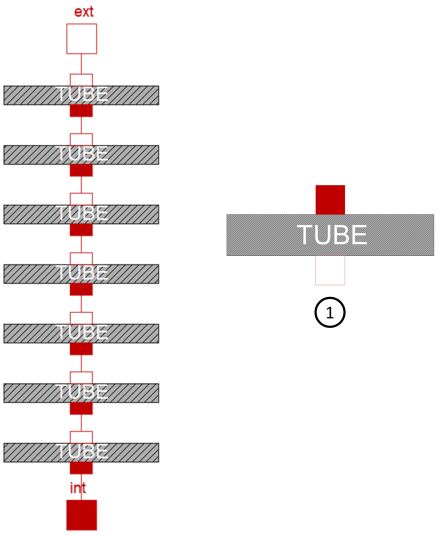

Figure 3.9: The first part of the fourth hierarchical layer with corresponding sub models and components. The first unique part of the fourth hierarchical layer (subsystem 3) is shown on the left, and the corresponding component on the right. The tube conduction component is denoted by number 1.

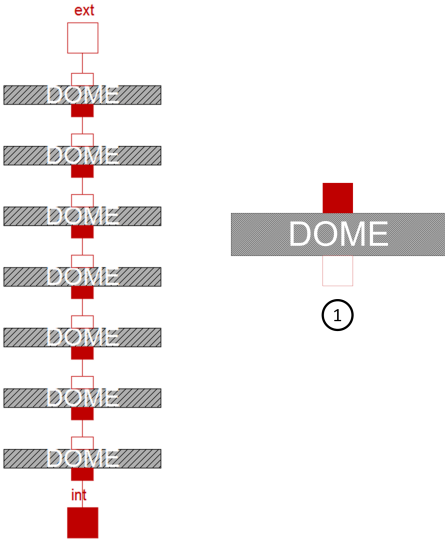

Figure 3.10: The second part of the fourth hierarchical layer with corresponding sub models and components. The second unique part of the fourth hierarchical layer (subsystem 3) is shown on the left, and the corresponding component on the right. The dome conduction component is denoted by number 1.

controller subsystem, designed by a peer MSc student, is denoted with number 2. Number 3 shows the Reverse Turbo-Brayton Cryocooler component, which is a simplified representation of the RTBC. The RTBC component has a constant cooling load temperature, and continuously removes heat from the fluid with a constant cooling power. Modelling the RTBC in this manner assumes ideal cooling operation and neglects the losses associated with the interaction of the RTBC with the fluid. Finally, most of the sub models in this hierarchical layer are the tank sections, denoted by number 4. Two dome sections, and 8 cylindrical tube sections are connected to the two-phased hydrogen mixture container component.

The third hierarchical layer, also subsystem 2, consists of the 8 tube tank section sub models and 2 dome tank sections as denoted by number 4 in Figure 3.7. There are two unique parts in the subsystem which are visualised in the same manner, but labelled differently. The visualisation is shown on the left of the figure, and the corresponding numbered sub model and components on the right. The fuselage/tank wall structure sub model is denoted by number 1, the external convection component by number 2, the wall radiation component by number 3, the tank insulation structure sub model by number 4, and the solar radiation component by number 5. Sub models 1 and 4 can be both filled by either the tube structure or dome structure sub models to create the unique tube tank section or the unique dome tank section.

The fourth hierarchical layer, also subsystem 3, consists of 4 unique sub models combining a total of 20 sub models. The unique fuselage/tank tube wall structure sub model and unique fuselage/tank dome wall structure sub models are denoted by number 1 in Figure 3.8. Figure 3.9 shows the fuselage/tank tube wall structure sub model on the left and the tube conduction component on the right. Figure 3.10 shows the fuselage/tank dome wall structure sub model on the left, and the dome conduction component on the right. The unique tube tank insulation structure and unique dome tank insulation structure sub models are constructed in the same way and with the same components as in Figure 3.9 and Figure 3.10. Instead of 7 layers of components, the tank insulation structure sub models have 11 layers of components.

In order to connect all sub models and components, four different types of connectors are used. The following connectors are used for the construction of the system model:

- Fluid Connector : Mass flow rate $\dot{m}$ (flow), pressure P (effort), specific enthalpy h (stream), composition X (stream) and extra (outside of standard mass-balance) transported properties C (stream). Since hydrogen has a single composition and no extra transported properties, the latter two stream variables are neglected by the hydrogen medium package.
- Thermal Connector : Temperature T (effort), and heat flow rate $\dot{Q}$ (flow).
- Irradiance Connector: Incident irradiance E (effort), and incidence angle θ (effort).

- Real Connector: Any real value $input$ or $output$ (effort).

Except for the two-phased hydrogen mixture component, all components are taken or adapted from existing libraries. The standard library components are taken from the Modelica Standard Library[2], developed by the Modelica Association. The hydrogen mass flow component is adapted from the ThermoPower library[3], developed by Prof. F. Casella [14]. All other components and sub models are taken or adapted from the DynTherM library[4], developed by Dr. A. Giuffré [36]. For all of the three libraries, documentation exists in open literature. In the following sections, therefore, only three non-standard library components are elaborated upon: the tube conduction, dome conduction, and two-phased hydrogen mixture component. Despite the tube conduction and non-aspect ratio dome conduction components having documentation from the original in-house library, they are shortly discussed in this report as they are of key importance to the model.

3.2.5. System of Equations

All components of the system model are first principles models. That is, all components are based on conservation laws and the first principles of thermodynamics. The foundation of the models are the conservation equations for mass and energy. These equations are, however, not sufficient to close a model. To complete the model, constitutive equation are required. These equations are mathematical relations that approximate physical phenomena (see Section 3.2.2) using certain hypotheses and assumptions (see Section 3.2.3). The definition of these mathematical equations involves a physically-based model which can be of different levels of fidelity and complexity.

Tube Conduction System of Equations

The Tube Conduction component is a 0D dynamic model of conduction in a hollow cylinder. The component lumps the cylinder with all its properties at the mean (half-)thickness. It contains 3 equations, one of which is a conservation equation (Equation (3.1)). The other two relate the heat conduction through the internal and external half-thickness of the lumped cylinder. Equations (3.2) and (3.3) are simply Fourier's law of thermal conduction integrated over respectively the internal and external half thicknesses. The equations are displayed below.

$$C_m \frac{dT_{vol}}{dt} = \dot{Q}_{int} + \dot{Q}_{ext} \tag{3.1}$$

$$\dot{Q}_{int} = \lambda(2c\pi L)\left(\frac{T_{int} - T_{vol}}{\log\left(\frac{R_{int}+R_{ext}}{2R_{int}}\right)}\right) \tag{3.2}$$

$$\dot{Q}_{ext} = \lambda(2c\pi L)\left(\frac{T_{ext} - T_{vol}}{\log\left(\frac{2R_{ext}}{R_{int}+R_{ext}}\right)}\right) \tag{3.3}$$

In these equations, $\dot{Q}_{int}$ and $\dot{Q}_{ext}$ are the heat flow rates through the internal and external half-thickness respectively, and T_{vol}, T_{int} and T_{ext} are the temperatures of the lumped volume, the internal surface and the external surface. R_{int} and R_{ext} are the radii at the internal and external surfaces, L is the length of the cylinder, λ is the thermal conductivity of the material, C_m is the heat capacity of the cylinder, and c is a coefficient that resembles the fraction of the cylinder with active heat transfer.

Dome Conduction System of Equations

The Dome Conduction component is, like the Tube Conduction component, a 0D dynamic model of conduction. It models conduction through a hollow sphere, where the component is lumped with all its properties at the mean (half-)thickness. It contains 3 equations, one of which is a conservation equation (Equation (3.4)). The other two relate the heat conduction through the internal and external half-thickness of the lumped sphere. Equations (3.2) and (3.3) are again Fourier's law of thermal conduction integrated over respectively the internal and external half thicknesses.

$$C_m \frac{dT_{vol}}{dt} = \dot{Q}_{int} + \dot{Q}_{ext} \tag{3.4}$$

[2]For more information, see `https://github.com/Modelica/ModelicaStandardLibrary`
[3]For more information, see `https://github.com/casella/ThermoPower`
[4]For more information, see `https://github.com/Propulsion-Power-TU-Delft/DynTherM`

$$\dot{Q}_{int} = \lambda(4c\pi R_{ext}R_{int}) \left(\frac{T_{int} - T_{vol}}{\frac{R_{ext}+R_{int}}{2} - R_{int}} \right) \tag{3.5}$$

$$\dot{Q}_{ext} = \lambda(4c\pi R_{ext}R_{int}) \left(\frac{T_{ext} - T_{vol}}{R_{ext} - \frac{R_{ext}+R_{int}}{2}} \right) \tag{3.6}$$

In these equations, $\dot{Q}_{int}$ and $\dot{Q}_{ext}$ are the heat flow rates through the internal and external half-thickness respectively, and T_{vol}, T_{int} and T_{ext} are the temperatures of the lumped volume, the internal surface and the external surface. R_{int} and R_{ext} are the radii at the internal and external surfaces, λ is the thermal conductivity of the material, C_m is the heat capacity of the sphere, and c is a coefficient that resembles the fraction of the sphere with active heat transfer. As a dome is generally half a sphere, this coefficient's default value is 0.5.

It is possible for the dome to have an aspect ratio (AR) smaller than 1. The definition of domes containing an aspect ratio is presented in Appendix B for the interested reader. If the domes have an aspect ratio, the radii R_{int} and R_{ext} in Equations (3.2) and (3.3) are simply replaced with the equivalent radii $R_{eq_{int}}$ and $R_{eq_{ext}}$ in Equation (3.7).

$$R_{eq_{int}} = R_{int} \left(\frac{1 + AR^2}{2AR} \right), \qquad R_{eq_{ext}} = R_{ext} \left(\frac{1 + AR^2}{2AR} \right) \tag{3.7}$$

Two-Phased Hydrogen Mixture Container System of Equations

The total System of Equations of the Two-Phased Hydrogen Mixture Container contains 257 equations and relations. The model is build upon 4 conservation equations, being supported by 215 constitutive equations, 28 boundary equations, 6 assertion conditions, and 4 initial equations. Additionally, an external fluid model for the hydrogen vapour and hydrogen liquid is used. The constitutive equations are divided into heat transfer, mass transfer, geometrical, and fluid thermodynamic equations. The boundary, assertion, and initial equations and relations are grouped into model specific equations and relations. These six categories are elaborated upon below.

Conservation Equations

The foundation of the two-phased hydrogen mixture container component are the mass and energy conservation equations. A diagram visualising the mass and energy transfer processes occurring in the component is shown in Figure 3.11. The variables in the diagram are explained in Table 3.1. The mass and energy transfer rates acting on the mixture are split up in two, i.e. those acting on the vapour CV and those acting on the liquid CV. The mass and energy conservation equations for the vapour CV are given by Equation (3.8) and Equation (3.10). Those for the liquid CV are given by Equation (3.9) and Equation (3.11). The variables in the conservation equations follow the notation of the library it is written in, and can therefore be different compared to the regular notation in this report such as used in Figure 3.11 (see Table 3.5).

$$\frac{dM_v}{dt} = q_v + w_{ev} - w_c + w_s \tag{3.8}$$

$$\frac{dM_l}{dt} = q_l - w_{ev} + w_c - w_s \tag{3.9}$$

$$\frac{dE_v}{dt} = q_v h_v + w_{ev} h_{vs} - w_c h_{ls} + w_s h_{vs} + \dot{Q}_{v_{tot}} - \dot{Q}_{vs} - P\frac{dV_v}{dt} \tag{3.10}$$

$$\frac{dE_l}{dt} = q_l h_l - w_{ev} h_{vs} + w_c h_{ls} - w_s h_{ls} + \dot{Q}_{l_{tot}} + \dot{Q}_{sl} - P\frac{dV_l}{dt} \tag{3.11}$$

In Equations (3.8) to (3.11), $\frac{dM_v}{dt}$ and $\frac{dM_l}{dt}$ are the time derivatives of the vapour and liquid mass respectively, and $\frac{dE_v}{dt}$ and $\frac{dE_l}{dt}$ are the time derivatives of the vapour and liquid energy respectively. The variables q_v and q_l are the vapour fluid and liquid fluid mass flow rates, and w_{ev}, w_c, and w_s are the bulk evaporation, bulk condensation, and surface mass flow rates respectively. Positive values of w_s correspond to evaporation, whilst negative values correspond to condensation on the surface interface. Furthermore, h_v and h_l are the specific enthalpy of the vapour and the liquid, h_{vs} is the specific enthalpy of saturated vapour at the tank pressure, and h_{ls} is the specific enthalpy of saturated liquid at the tank

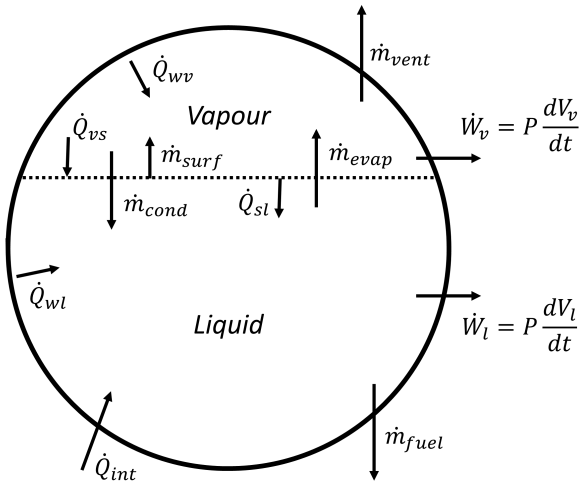

Figure 3.11: Diagram of all mass and energy transfers of the two-phased hydrogen mixture container component

pressure. The variables $\dot{Q}_{v_{tot}}$ and $\dot{Q}_{l_{tot}}$ are the total heat transfer rates to the vapour and the liquid, $\dot{Q}_{vs}$ and $\dot{Q}_{sl}$ are the heat transfer rate from the vapour towards the surface and the heat transfer rate from the surface towards the liquid respectively, and $P\frac{dV_v}{dt}$ and $P\frac{dV_l}{dt}$ are the tank pressure multiplied with the change in volume over time for the vapour and the liquid (i.e. the work done by the vapour and the liquid $\dot{W}_v$ and $\dot{W}_l$).

Table 3.5: Relation of different heat and mass transfer variable notations in Equations (3.8) to (3.11) to Figure 3.11

Notation	Definition	Notation	Definition
$\dot{Q}_{v_{tot}}$	$\dot{Q}_{wv}$	w_{ev}	$\dot{m}_{evap}$
$\dot{Q}_{l_{tot}}$	$\dot{Q}_{wl} + \dot{Q}_{int}$	w_c	$\dot{m}_{cond}$
$\dot{Q}_{vs}$	$\dot{Q}_{vs}$	w_s	$\dot{m}_{surf}$
$\dot{Q}_{sl}$	$\dot{Q}_{sl}$	q_v	$\dot{m}_{vent}$
		q_l	$\dot{m}_{fuel}$

Heat Transfer

The heat transfer processes occurring within the tank are convective and radiative heat transfer between the wall and the liquid and vapour volumes, and the heat transfer between the infinitely thin surface layer and the vapour and liquid volumes (see Section 3.2.2). It is assumed that that during the duration of the flight, the velocity fields inside the tank are small and do not generate any forced convection. Additionally, the assumption is made that the vapour does not receive any radiative heat transfer, as the wall is at a temperature close to 0K and hydrogen gas is transparent for thermal radiation (see Section 3.2.3) [91]. The liquid-wall interface therefore experiences natural convection and radiation, whereas the vapour-wall interface only experiences natural convection. The heat transfer between the vapour-liquid interface is modelled with a conduction model as done in validated literature, as no correlations exist for the corresponding heat flow rate in a finite volume [9]. For this conduction model, it is assumed that the surface layer in infinitely thin and that the temperature of the vapour and liquid are linearly dependent on the height.

Natural convection is modelled using dimensional analysis (Buckingham-Pi theorem). For the liquid, the following correlation is used [46, 91, 94]:

$$Nu_{h_l} = 0.0605 Ra_{h_l}^{1/3} \tag{3.12}$$

This relation was derived from a heat transfer model focusing on diffusive transport, and deemed representative for natural convection of hydrogen in an enclosure under normal gravity conditions [46]. The relation was developed for a broad range of applications, including cryogenic tankage on spacecraft, and produces conservative results [91].

The definition of the Nusselt, Rayleigh, and Prandtl numbers completing the dimensional analysis are defined as[5]:

$$Nu_{h_l} = \frac{h_{conv_l} \cdot h}{k_l}, \qquad Ra_{h_l} = \frac{g \cdot \beta \cdot \Delta T \cdot h^3 \cdot Pr \cdot \rho^2}{{\mu_l}^2}, \qquad Pr = \frac{\mu_l \cdot c_p}{k_l} \tag{3.13}$$

In these equations, h_{conv_l} is the convective heat transfer coefficient between the liquid and the wall, k_l is the thermal conductivity of the liquid, g is the gravitational acceleration, β is the thermal expensaion coefficient of the liquid, ΔT is the temperature difference between the wall and the liquid, ρ is the density of the liquid, μ_l is the dynamic viscosity of the liquid, and c_p is the liquid's specific heat at constant pressure. Both the Nusselt and Rayleigh number use the height of the liquid level h as characterising length.

For the vapour, only limited data is available in literature to determine a relation for the dimensional analysis [91]. Initially, a correlation by Brewer [13] was adopted in correspondence with Verstraete [91] and Woensel [94]:

$$Nu_v = 17 \tag{3.14}$$

During validation, however, this correlation was replaced by a peer MSc student in order to match the experimental results slightly better. The incorporated relation describes the analytical solution for natural convection in enclosures heated from the side. It holds for fluids with $Pr > 1$ such as water, oils, and as a limiting case, gases (air) [6]. The circulation pattern regimes for which the relation holds are shown in Figures 3.12 and 3.13. Gill [33] first provided the analytical solution to the heat transfer rates in regimes III and IV. Bejan [7] provided notes on the original paper, with the addition of the overall heat transfer rate across the enclosure. This analytical solution to the overall heat transfer rate is provided in Equation (3.15).

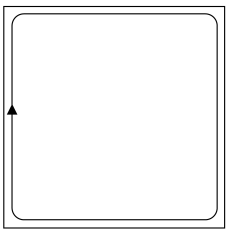

Regime III

Figure 3.12: Circulation pattern associated with high Rayleigh numbers (boundary layer regime) [6]

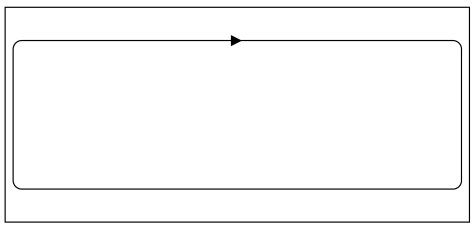

Regime IV

Figure 3.13: Circulation pattern associated with a shallow enclosure limit [6]

$$Nu_{h_v} = 0.364 \frac{L}{H} \cdot Ra^{1/4} = 0.364 \frac{D}{(D-h)} Ra_{h_v}^{1/4} \tag{3.15}$$

In Equation (3.15) L is the the horizontal length, which is the diameter of the tank D. The characteristic height H is chosen to be the height of the vapour volume, which is the diameter minus the height of the liquid volume $(D-h)$. The Nusselt, Rayleigh and Prandtl numbers can be obtained by substituting the new characteristic length $(D-h)$ into the characteristic length of the liquid h in Equation (3.13).

Equation (3.15) is an analytical solution, is based on circulation patterns that do not match the geometry exactly, and assumes side heating only. Moreover, it is not developed for cryogenic hydrogen vapour. Depending on its thermodynamic state, however, hydrogen vapour has a Prandtl number of around $Pr \approx 0.7$, which is close to that of air at ambient temperatures. Despite its limitations, Equation (3.15) provided an improvement during validation when compared to Equation (3.14). It is, however, recommended to improve the used heat transfer relations for natural convection of the cryogenic hydrogen vapour in the tank.

For the radiative heat transfer to the liquid, use is made of an equivalent convective coefficient h_{rad_l} [60, 91]:

$$h_{rad_l} = \epsilon\sigma(T_w^2 + T_l^2)(T_w + T_l) \tag{3.16}$$

[5] In the research from Verstraete [91] and Woensel [94], the kinematic viscosity is incorrectly not squared, which would make the dimensionless Nusselt and Rayleigh number have a dimension (see the original paper from Hochstein et al. [46] for the correct relation).

Where T_w and T_l are the wall and liquid temperature respectively, σ is the Stefan-Boltzmann constant and ϵ is the emittance of the wall.

The final heat load for each wall segment can then be calculated using

$$\dot{Q}_{wl} = h_{tot_l} A_{wl}(T_w - T_l)\,, \qquad \dot{Q}_{wv} = h_{tot_v} A_{wv}(T_w - T_v) \tag{3.17}$$

Where

$$h_{tot} = h_{conv} + h_{rad} \tag{3.18}$$

And where A_{wl} and A_{wv} are the area's of each segment in contact with the liquid and vapour respectively.

The heat flow rates acting on the infinitely thin surface layer are calculated by a conduction model consisting of the following equations:

$$\dot{Q}_{vs} = 2A_{sup}\frac{\lambda_v(T_v - T_s)}{h_v}\,, \qquad \dot{Q}_{sl} = 2A_{sup}\frac{\lambda_l(T_s - T_l)}{h_l} \tag{3.19}$$

Where $\dot{Q}_{vs}$ and $\dot{Q}_{sl}$ are the heat transfer rate from the vapour towards the surface and the heat transfer rate from the surface towards the liquid respectively, A_{sup} is the area of the surface layer, λ_v and λ_l are thermal conductivity of the vapour and liquid, and h_v and h_l are the height to the centre of the vapour and liquid liquid volumes with respect to the surface layer. The heights are defined by Equation (3.20), where R_{int} is the internal radius of the cylindrical section of the tank, and y is the level as referred to the centreline of the tank.

$$h_v = \frac{(R_{int} - y)}{2}\,, \qquad h_l = \frac{(R_{int} + y)}{2} \tag{3.20}$$

Mass Transfer

Mass transfer in the model can occur through six separate phenomena. The four naturally occurring phenomena are bulk evaporation (or bulk boiling), bulk condensation, and surface layer condensation and evaporation. In addition, liquid can be withdrawn for fuel usage and vapour can be released for venting operations. The fuel and venting mass flow rate are controlled by other components in the model, and are inputs to the two-phased hydrogen mixture container component.

The surface layer condensation and evaporation mass flow rates are calculated by using the energy jumping boundary condition, proposed by Delhaye [23] and Meserole et al. [68]. They suggest that at a point belonging to a surface of discontinuity (Truesdell and Toupin [90]), such as phase change, the local fundamental conservation laws are not expressed by partial differential equations, but by jump conditions. Using these jump conditions at the surface layer leads to Equation (3.21), as proposed by Bolshinskiy et al. [9]. In this equation, the mass transfer is calculated by dividing the heat flow occurring over the surface layer by the difference in enthalpy of the vapour and liquid at the thermodynamic state of the saturated infinitely thin surface layer:

$$w_s = \frac{\dot{Q}_{vs} - \dot{Q}_{sl}}{Dh_s} \tag{3.21}$$

Positive values of w_s correspond to evaporation, whilst negative values correspond to condensation on the surface interface. In this equation $\dot{Q}_{vs}$ and $\dot{Q}_{sl}$ are the heat transfer rate from the vapour towards the surface and the heat transfer rate from the surface towards the liquid respectively, and Dh_s is defined as:

$$Dh_s = h_{vs} - h_{ls} \tag{3.22}$$

The bulk evaporation and condensation rates are determined by the external fluid property model, which threats the liquid and vapour volumes as independent two-phased mixtures. As boiling or condensation occurs, bubbles or dew will start to form in the liquid and vapour volumes respectively. This is computed in the fluid property model based on the energy jumping boundary condition. The formulation of relations to describe the propagation of bubbles and dew throughout their volumes in order

to get the exact mass flow rates is deemed unnecessary complex. Instead, the mass flow rates are determined using the same method as used by Casella and Leva in their steam drum component in the ThermoPower Modelica library [14]. This method makes use of a time constant over which the bubble and dew propagation occur that ensures stability of the model simulations. The equations describing the mass transfer are:

$$w_{ev} = \frac{x_l \rho_l V_l}{\tau_{ev}} \qquad\qquad w_c = \frac{(1 - x_v)\rho_v V_v}{\tau_c} \tag{3.23}$$

In here, w_{ev} and w_c are the bulk evaporation and condensation mass flow rates, ρ_l, ρ_v, V_l and V_v are the density and volume of the liquid and vapour, and x_l and x_v are the vapour quality in the liquid and vapour volume. The vapour qualities are described by

$$\text{if} \quad h_l \leq h_{ls}: \quad x_l = 0, \qquad\qquad \text{else}: \quad x_l = \frac{h_l - h_{ls}}{h_{vs} - h_{ls}} \tag{3.24}$$

$$\text{if} \quad h_v \geq h_{vs}: \quad x_v = 1, \qquad\qquad \text{else}: \quad x_l = \frac{h_v - h_{ls}}{h_{vs} - h_{ls}} \tag{3.25}$$

The time constants of evaporation and condensation, τ_{ev} and τ_c, are set to a default of 10 seconds for stable simulation, but can be changed according to the required simulation stability and other requirements of the problem formulation.

Geometrical Relations

For airborne liquid hydrogen fuel tankage, correct modelling of the external and internal heat transfer distribution is extremely important. Incorrect modelling of the heat distribution can result in an error of a factor 6 (see Section 2.2.5). Geometrical relations are therefore crucial, and set this model apart from other hydrogen tankage models.

The main geometrical variable that determines the internal heating distribution is the level of the liquid in the tank. This level can vary between a full and an empty tank during the mission time span, which results in a highly dynamic system. It is, however, impossible to explicitly define a mathematical relation for the level of the liquid in a horizontal cylindrical tank with or without end domes. As the model is implemented in Modelica (see Section 3.2.6), it is not needed to explicitly define all variables if the model is well-posed. The liquid level is therefore implicitly defined using the liquid volume, which can be calculated by the model using the initial conditions, the mass conservation equations and the thermodynamic state of the liquid.

The liquid volume of a horizontal cylindrical tank is determined by the following geometrical relation, where y is the level of the liquid volume referred to the centreline of the tank:

$$V_{l_{cyl}} = L\left(R_{int} \arccos\left(\frac{-y}{R_{int}}\right) + y\sqrt{R_{int}^2 - y^2}\right) \tag{3.26}$$

Where $V_{l_{cyl}}$ is the liquid volume, L is the length, and R_{int} is the internal radius of the cylindrical section. The interface area between the wall and the liquid volume is then calculated using

$$A_{wl_{cyl}} = 2LR_{int} \arccos\left(\frac{-y}{R_{int}}\right) \tag{3.27}$$

And the liquid-vapour interface area by

$$A_{sup_{cyl}} = 2L\sqrt{R_{int}^2 - y^2} \tag{3.28}$$

The relations completing the definition of the geometrical system are then

$$V_t = V_l + V_v \qquad\qquad A_{wt} = A_{wl} + A_{wv} \tag{3.29}$$

Where the total volume V_t and wall area A_{wt} are known inputs, and the vapour volume V_v and wall vapour interface area A_{wv} are computed. The wall is then discretised in 8 sections of $\frac{1}{4}\pi$ radians each, such that each segment can have a different heat flow connector.

In the case where two end domes are present, having an aspect ratio AR, Equations (3.26) to (3.28) are extended to Equations (3.30) to (3.32). The geometrical definition of the additional terms are elaborated upon in Appendix B for the interested reader. The domes were chosen not to be discretised like the cylindrical wall segments, as that would increase the model complexity and computational time drastically with little accuracy improvement.

$$V_l = L\left(R_{int}\arccos\left(\frac{-y}{R_{int}}\right) + y\sqrt{R_{int}^2 - y^2}\right) + \pi\left(y_0 + dR\right)^2\left(R_{eq} - \frac{1}{3}\left(y_0 + dR\right)\right) - 2\left(L^*\left(R^{*2}\arccos\left(\frac{-y}{R^*}\right) + y\sqrt{R^{*2} - y^2}\right)\right) \tag{3.30}$$

$$A_{wl} = 2LR_{int}\arccos\left(\frac{-y}{R_{int}}\right) + 2\pi R_{eq}\left(y_0 + dR\right) - 2\left(2L^*R^*\arccos\left(\frac{-y}{R^*}\right)\right) \tag{3.31}$$

$$A_{sup} = 2L\sqrt{R_{int}^2 - y^2} + \pi\left(R_{eq}\cos\left(\arcsin\left(\frac{y}{R_{eq}}\right)\right)\right)^2 - 2\left(2L^*\sqrt{R^{*2} - y^2}\right) \tag{3.32}$$

Fluid Thermodynamic Properties and Relations

The fluid thermodynamic properties are calculated by the fluid library ExternalMedia (see Section 3.2.6). The communication between the external fluid database and the model is performed by a C/C++ interface layer. This layer is called via external C functions, which make use of C++ objects. The function of the interface layer is to initialise and maintain the external fluid computation codes (i.e. active solvers).

The implementation of ExternalMedia in the Modelica component is to first set the thermodynamic state of the liquid, vapour and the saturation state, based on the tank pressure and the state enthalpy. All functions returning state properties are called after setting the state record, so that most of the CPU time is spent solving the basic equations of state. The calculation of the derived properties add a minor overhead in this way. As Modelica is a declarative modelling language, great care must be taken in the calling of the medium functions in order for the solver to work. As the order of calling the functions is not guaranteed and the interface layer and solvers can act like 'black boxes', the correct method to call the functions can vary per component.

In this two-phased hydrogen mixture container component, the only external equations used are:

$$\text{Saturation State Record} = f(P)\,, \quad \text{Liquid State Record} = f(P, h_l)\,, \quad \text{Vapour State Record} = f(P, h_v)\,,$$

$$T_l = f(P, h_l)\,, \qquad \rho_l = f(P, h_l)\,, \qquad T_v = f(P, h_v)\,, \qquad \rho_v = f(P, h_v)$$

All other medium properties are directly accessed via the state records.

Model Specific Equations and Relations

The boundary, assertion, and initial equations and relations are grouped under the model specific equations and relations. All boundary equations relate the component external connectors to the variables inside the component. An example equation would be the boundary conditions for the liquid hydrogen fuel outlet:

$$P_{LH2_{out}} = P_{tank}\,, \qquad w_{LH2_{out}} = q_l$$

In addition to these two equations, 26 other boundary equations are present. These are left for the interested reader to read in the source code of the final model.

The model uses an implicit high order multi-step differential algebraic system solver, namely DASSL. The original solver is described by Petzold [75], however, the used implementation is called DASPK2.0[6] and is described by Li and Petzold [59]. Due to the nature of the solver, measures are needed to ensure the model is not evaluated outside the limits of physical validity. This would otherwise lead to incorrect results. In Modelica, assertion conditions can be included in the code that raise errors if the model is evaluated outside the limits of validity. For example, a large step-size in the solver or a value of an

[6] For more information, see `https://openmodelica.org/doc/OpenModelicaUsersGuide/latest/solving.html#f1`

iteration variable might lead to the evaluation of the model for a liquid level outside of the tank. This is undesirable, so an assertion checks that the liquid level stays within the limits of the tank wall. In total, six assertions were needed to be developed to ensure solver stability:

$$M_l > 0 + \epsilon\,, \qquad M_v > 0 + \epsilon\,, \qquad V_l > 0 + \epsilon\,, \qquad V_v > 0 + \epsilon\,,$$

$$y < R_{int} - \epsilon\,, \qquad y > -R_{int} + \epsilon$$

All of the assertions check whether the gaseous or liquid hydrogen is depleted. The first four do so directly by checking the masses and volumes. The last two do so by checking that the liquid level does not exceed the tank radius in both directions. All relations have the numerical error term ϵ. This term is selected to ensure solver stability, and has been set to a default of 1E-6. Solver stability is ensured by selecting the numerical error term to be small enough to ensure accurate results, and large enough to ensure the solver's step size never oversteps the intended assertion conditions and a simulation error occurs instead of an assertion error.

The assertion conditions check for the two depletion situations, and stop the codes when one of them occurs. If the liquid hydrogen is depleted, the aircraft has run out of fuel and the code is therefore terminated. If the gaseous hydrogen is depleted, the pressure has build up so tremendously that all gas has been vented and the tank becomes a one-phased liquid hydrogen container. This would result in an unsafe situation with a high risk of explosion, as the pressure rise with absorbed heat becomes incredibly steep. When this risk of explosion starts to occur, the code is terminated.

The final model specific equations are the initial equations. Three options can be selected: no initialisation, fixed state initialisation, and steady state initialisation. If the no initialisation option is selected, no initial equations are provided. For the fixed state initialisation, four initial equations are provided:

$$P = P_{start}\,, \qquad h_l = h_{l_{start}}\,, \qquad h_v = h_{v_{start}}\,, \qquad V_l = V_{l_{start}}$$

For the steady state initialisation, also four equations are provided:

$$\frac{dP}{dt} = 0\,, \qquad \frac{dh_l}{dt} = 0\,, \qquad \frac{dh_v}{dt} = 0\,, \qquad \frac{dV_l}{dt} = 0$$

Thee first three initial variables were chosen due to the model dependency on the fluid model which is set by the pressure, and the enthalpy of the liquid and vapour states. The last initial variable was selected as the liquid volume implicitly determines the most important variable for the heat flow calculations, that is the liquid level y. Moreover, the liquid volume is generally known during conceptual design as opposed to other unknown geometrical data important for heat calculations. The number of initial equations matches the number of DAEs present in the model (i.e. the conservation equations), and corresponding ODEs in the translated model. For the fixed state initialisation, the standard starting enthalpy for the liquid and vapour are the enthalpy at bubble point and at dew point at the tank pressure respectively.

As the liquid level y is implicitly calculated from the liquid volume V_l, it is an iteration variable of the initialisation problem. Therefore, an additional starting value or 'guess' for the liquid level is provided to improve solver stability at the start of the simulation. This starting value is chosen for simulation stability, but has no effect on the final simulation results. This starting value is:

$$y_{start} = 0.808 F_f R_{int}$$

In this equation, F_f is the fill fraction of the tank. The fill fraction is defined as the fraction of volume the liquid occupies in the tank at the start of the simulation.

3.2.6. Implementation

The hydrogen tank model is created within Dymola. Dymola is a simulation environment developed by Dassault Systèmes based on the Modelica modelling language. This simulation environment was chosen due to the experience of the supervisors with this program, and the superb interface of the Modelica language that it offers. The equations and relations are written in the interface, which are then

solved by Dymola based on the coding language of C. The differential algebraic system of the model is translated into a system of ordinary differential equations which is solved by the DASSL solution algorithm. The DASSL algorithm is an implicit high order, multi-step solver, which can solve systems that are substantially more complex than standard form ODE systems. The solver is based on the backward differentiation formula, and has a mature source code. The used tolerance in the simulation is 1E-6.

The compiler used for Dymola is Visual Studio 2019/Visual C++ 2019. The visualisation of the results is done in the Dymola interface. After running the model for well considered inputs, the results are checked so that no coding error occurs. Dymola can also be accessed outside of the Dymola environment, using python. For this end, a python interface comes readily available with the Dymola installation. From within the python compiler of choice, simulations can be set up, run, and visualised. This makes automated model simulations possible, and contributes to the insights presented in Section 4.4.

The fluid library used in the tank model is ExternalMedia. ExternalMedia provides a framework in Modelica for interfacing external fluid property models. It computes the fluid properties to Modelica.Media-compatible component models. ExternalMedia has been designed whilst keeping two main goals in mind. That is, maximising the efficiency of the code, whilst minimising the extra code required to interface existing external codes to the library. The library provides Modelica media packages of pure fluid models, including two-phased models, which are fully compatible with the *Modelica.Media.Interfaces.PartialTwoPhaseMedium* interface. Two external fluid property model software are currently supported by ExternalMedia: FluidProp and CoolProp.

Without a licence, FluidProp does not model ortho- or para-hydrogen, and only models hydrogen using GasMix (ideal gas model) and FreeStanMix (PRSV cubic equation of state). CoolProp, however, does not require a licence and models the equation of state [55], thermal conductivity [3], viscosity [70], melting line [22] and surface tension [69] of hydrogen accurately. Due to the requirement of a licence for FluidProp and the intention of open usability of the tank model, CoolProp is used. CoolProp is validated with REFPROP, which makes use of the NIST Reference Fluid Thermodynamic and Transport Properties Database.

3.3. Design & Modelling Methodology of the Reverse Turbo-Brayton Cryocooler

The purpose of designing and modelling the Reverse Turbo-Brayton Cryocooler (RTBC) is twofold. First, it is to open the public research space in high-capacity airborne cryocoolers. Second, it is to show the potential of using RTBC for the cooling of cryogenic hydrogen storage for long range flight. In order to achieve this purpose, an RTBC system design is performed, as well as the conceptual design of the high-speed miniature compressor. For the conceptual design of the compressor, in-house tools and models exist. For the system design of the RTBC, a simple model is created based on thermodynamic equations and relations. The design and modelling methodology of the RTBC follows the 9-step method as explained in the chapter introduction, however, the sub model of the compressor is designed and modelled using Scaling Analysis.

The section is structured in two subsections. The design and modelling methodology of the RTBC system is presented in Section 3.3.1, after which the detailed conceptual compressor design and modelling methodology is presented in Section 3.3.2.

3.3.1. System model of the Reverse Turbo-Brayton Cryocooler

A single-stage RTBC system is considered in this research, as this provides a clear benchmark for further studies on airborne RTBC. The cycle diagram and TS-diagram of the system is visualised in Figure 3.14. The purpose of the system model is to obtain the performance parameters and TS-diagram of the system, whilst only knowing information about the subsystem efficiencies, cooling load temperature, aftercooler outlet temperature, compressor pressure ratio, and the cooling power. This subsection first gives the definition of the system model. Then the assumptions are stated and the system of equations is provided. Finally, the implementation of the model and the system optimisation are described.

Definition of the system model

The system model models the thermodynamic processes occurring to the working fluid in the RTB-cycle as depicted in Figure 3.14. It is a static model, intended for on-design system optimisation. The model lumps the fluid to six stations, at which the pressure and temperature are defined. Between the stations in the cycle, six processes occur. These processes are:

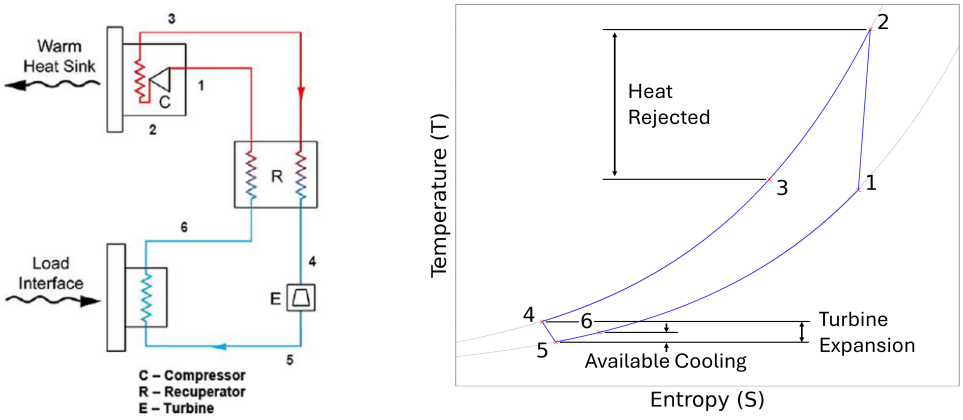

Figure 3.14: Cycle diagram [97] (left) and TS-diagram (right) of a single stage Reverse Turbo-Brayton Cycle

- Non-isentropic compression in the compressor (station 1-2)
- Heat rejection in the aftercooler (station 2-3)
- Pre-cooling in the recuperator (station 3-4)
- Non-isentropic expansion in the turbine (station 4-5)
- Heat absorption at the cooling load (station 5-6)
- Pre-heating in the recuperator (station 6-1)

In Section 2.1.3 it has been described that the recuperator is the most heavy component of the system, and thus its performance requirements will be strict. Hwang and Jeong [48] showed that for recuperators with strict requirements, pressure drops should be considered in the system design, despite it being regularly neglected in the design stage. In addition to the processes described above, therefore, the pressure losses the cycle working fluid experiences over the heat exchanger and recuperator components are included.

Assumptions

In order to simplify the processes occurring in the cycle, assumptions are formulated. These assumptions are:

- The working fluid is a calorically perfect (ideal) gas.
- The load interface and warm heat sink heat exchangers have ideal thermal performance.
- No thermal parasitics are present.
- No electronic losses occur.
- The compressor has no inverter losses.
- No losses are present in the turboalternator power recovery.
- Pressure losses between the processes (i.e. tubing, etc.) are negligible.
- The pressure losses in the heat exhangers and recuperator are assumed based on values presented in literature.
- The value of the turbine efficiency is assumed based on literature.
- The value of the recuperator thermal effectiveness is assumed based on literature.

The value of the compressor efficiency is not assumed, but will be the result of the conceptual compressor design presented later in this section.

System of Equations

The System of Equations is based on the First Law of Thermodynamics, namely that the energy accumulation of a closed system is equal to the energy input as work and heat:

$$W + Q = \Delta U \tag{3.33}$$

Applying this basic idea of energy consumption to the Reverse Turbo-Brayton cycle gives

$$\Delta U_{1-2-3-4-5-6} = (Q_{in} - Q_{out}) + (W_{in} - W_{out}) = 0 \tag{3.34}$$

Where ΔU is zero, since U is a function of state and the cycle returns the system to its original starting state. For each process, an energy balance equation can be set up expressing the work or heat input/output as the change in enthalpy during the process. This relation, based on the definition of specific heat at constant pressure, is shown in Equation (3.35). Furthermore, this equation is about energy input (or output), so work and heat can therefore be used interchangeably based on the occurring process.

$$dQ = Mdh = Mc_p dT \tag{3.35}$$

The resulting energy balances for the six processes are then:

$$\text{Compression:} \quad \dot{W}_{1-2} = \dot{m}c_p(T_2 - T_1) \tag{3.36}$$

$$\text{Heat rejection:} \quad \dot{Q}_{2-3} = \dot{m}c_p(T_2 - T_3) \tag{3.37}$$

$$\text{Heat rejection:} \quad \dot{Q}_{3-4} = \dot{m}c_p(T_3 - T_4) \tag{3.38}$$

$$\text{Expansion:} \quad \dot{W}_{4-5} = \dot{m}c_p(T_4 - T_5) \tag{3.39}$$

$$\text{Heat absorption:} \quad \dot{Q}_{5-6} = \dot{m}c_p(T_6 - T_5) \tag{3.40}$$

$$\text{Heat absorption:} \quad \dot{Q}_{6-1} = \dot{m}c_p(T_1 - T_6) \tag{3.41}$$

To complete the System of Equations, three energy loss equations are defined for the compressor, turbine, and recuperator, relating the component efficiency to temperatures inside the processes. These equation can be derived from the definition of the compressor and turbine isentropic efficiencies and the recuperator thermal effectiveness as stated in Equations (3.42) to (3.44).

$$\eta_C = \frac{\dot{W}_{comp}^{ideal}}{\dot{W}_{comp}^{real}}\,; \qquad \eta_T = \frac{\dot{W}_{turb}^{real}}{\dot{W}_{turb}^{ideal}}\,; \tag{3.42, 43}$$

$$\epsilon_R = \frac{\dot{Q}_{recup}^{real}}{\dot{Q}_{recup}^{max}} \tag{3.44}$$

In these equations, η_C, and η_T are the isentropic efficiencies for the compressor and turbine, and ϵ_R is the thermal effectiveness of the recuperator. Note that the non-isentropic real work is in the denominator for the compression process, and in the numerator for the expansion process. This is due to the increase in required work for non-isentropic compression in the compressor, and the decreased work output for non-isentropic expansion in the turbine. In Equation (3.44), a distinction is made by equating the real heat transfer to the maximum heat transfer, instead of the ideal heat transfer. The use of the term maximum is preferred here as it equates the thermal effectiveness, not the isentropic efficiency.

Using the isentropic compression or expansion equations and making use of mathematical manipulation, Equations (3.42) and (3.43) can be written as Equations (3.45) and (3.46), where Π_C and Π_T are the pressure ratios for the compressor and turbine respectively. Equation (3.47) can be derived from Equation (3.44), utilising that the maximum heat transfer between the cold and warm streams of the recuperator is the enthalpy difference between the cold and warm inlets $\dot{m}c_p(T_3 - T_6)$. Additionally, the real heat transfer between the cold and warm streams is either the absolute enthalpy difference over the warm stream $\dot{m}c_p(T_3 - T_4)$ or the absolute enthalpy difference over the cold stream $\dot{m}c_p(T_1 - T_6)$. The recuperator loss $\dot{Q}_{R_L}$ is then simply the difference between the maximum heat transfer and the real heat transfer of the recuperator $\dot{Q}_{recup}^{max} - \dot{Q}_{recup}^{real}$, which can be obtained by mathematical manipulation.

$$\frac{T_2}{T_1} = \frac{\Pi_C^{\frac{\gamma-1}{\gamma}} - 1}{\eta_C} + 1\,; \qquad \frac{T_5}{T_4} = 1 - \eta_T\left(1 - \Pi_T^{\frac{\gamma-1}{\gamma}}\right)\,; \tag{3.45, 46}$$

$$\dot{Q}_{R_L} = \dot{m}c_p(1 - \epsilon_R)(T_3 - T_6) \tag{3.47}$$

It is important to note that the recuperator loss $\dot{Q}_{R_L}$ in Equation (3.47) is not an actual heat loss leaving the system, but a loss with respect to the fictional maximum heat transfer obtained if the recuperator would have a 100% thermal effectiveness. It is assumed that the recuperator is adiabatic, and

that therefore no heat losses to the environment occur. Furthermore, the assumption is used that the working fluid behaves as a calorically perfect gas, and that the heat exchangers at the load interface and warm heat sink have ideal thermal performance such that T_3 and T_6 are constant and can be used as system inputs. These assumptions generally hold for RTBC designs [97].

The performance parameters of the system are defined as the Coefficient of Performance COP, the Carnot efficiency η_{carnot}, and the COP as a percentage of Carnot efficiency $\%\eta_{carnot}$. The COP is defined as the ratio of the net cooling provided to the net work required, see Equation (3.51). In this equation, $\dot{Q}_{net}$ is the net cooling power, $\dot{W}_C$ is the compressor power and $\dot{W}_T$ is the turbine power. The Carnot efficiency of the cycle is the maximum attainable efficiency, and is defined using basic energy and entropy balances. Using Figure 3.14 and assuming no energy or entropy accumulation, the energy and entropy balances can respectively be written as

$$\underbrace{Q_{net} + (W_C - W_T)}_{\text{energy input}} = \underbrace{Q_{2-3}}_{\text{energy output}} \quad ; \qquad \underbrace{\frac{Q_{net}}{T_6}}_{\text{entropy input}} + \underbrace{\mathcal{P}_{\mathcal{S}}}_{\text{entropy production}} = \underbrace{\frac{Q_{2-3}}{T_3}}_{\text{entropy output}} \tag{3.48, 49}$$

Equation (3.48) can be substituted in Equation (3.49) for Q_{2-3}. Solving for the efficiency results in

$$\eta = \frac{Q_{net}}{W_C - W_T} = \frac{Q_{net}}{Q_{net}(T_3/T_6 - 1) + \mathcal{P}_{\mathcal{S}} T_6} \tag{3.50}$$

The second law of thermodynamics requires $\mathcal{P}_{\mathcal{S}} \geq 0$, resulting in the term $\mathcal{P}_{\mathcal{S}} T_6$ to be positive. This shows that the entropy production term will always reduce the efficiency below its maximum. Therefore, the maximum efficiency η_{carnot} is obtained when the RTBC cycle is reversible and does not produce entropy, as expressed by Equation (3.52). The COP as a percentage of Carnot efficiency is then simply expressed by Equation (3.53).

$$COP = \frac{\dot{Q}_{net}}{\dot{W}_C - \dot{W}_T} \, ; \qquad \eta_{carnot} = \frac{1}{T_3/T_6 - 1} \, ; \tag{3.51, 52}$$

$$\%\eta_{carnot} = \frac{COP}{\eta_{carnot}} = \frac{\dot{Q}_{net}}{\dot{W}_C - \dot{W}_T} \left(\frac{T_3}{T_6} - 1 \right) \tag{3.53}$$

Implementation

The system model for the RTBC is written in Python and compiled by Visual Studio Code. The flowchart of the code is shown in Figure 3.15. Note that the non-dimensional variables $\tilde{w}_T, \tilde{w}_C, \tilde{q}_{R_L}, \tilde{q}_{hot}$, and $\tilde{q}_{net}$ are the corresponding dimensional variables divided by the mass flow and specific heat ($\dot{m} c_p$), and is in essence the temperature difference over each process.

The Equations of State (EoS) are obtained through the low level interface of CoolProp. For the fluid relation computations related to the RTBC system model in this report, the REFPROP library is used. CoolProp relies on the use of an Abstract State Class that provides the basic fluid properties based on interrelations of the fluid properties, their derivatives and the Helmholtz energy terms. The state resulting from the Abstract State Class is updated using two state variables, resulting in the EoS. In the RTBC system model, pressure and temperature are used as the two state variables defining the EoS.

Optimisation

In order to study the variation of system and subsystem parameters of the RTBC with the design variables, an optimisation study is done. With this study, the optimal design point is chosen. As seen in Figure 3.15, just four design variables for the RTBC system exist. Namely, **the cooling power $\dot{Q}_C$, the cold load temperature T_6, the heat rejection temperature T_3, and the pressure ratio of the compressor Π_C**. The cooling power $\dot{Q}_C$ and temperatures T_6 and T_3 are set by the application, which in this research is the cooling of the liquid hydrogen fuel tank onboard the Flying-V (Section 3.1). The only remaining design variable that can be selected for optimisation is the compressor pressure ratio.

The optimisation study has the objective to minimise its coefficient of performance (COP). In order to stay consistent with literature, the results are also expressed in the percentage of Carnot efficiency. This is effectively the COP as percent of the Carnot efficiency. The Carnot efficiency of the cycle is solely determined by the (fixed) temperatures T_6 and T_3, and is therefore exlusively determined by its application. The optimisation study is done for a pressure ratio range between 1 and 8. For all pressure ratios that have no feasible design, the results are omitted.

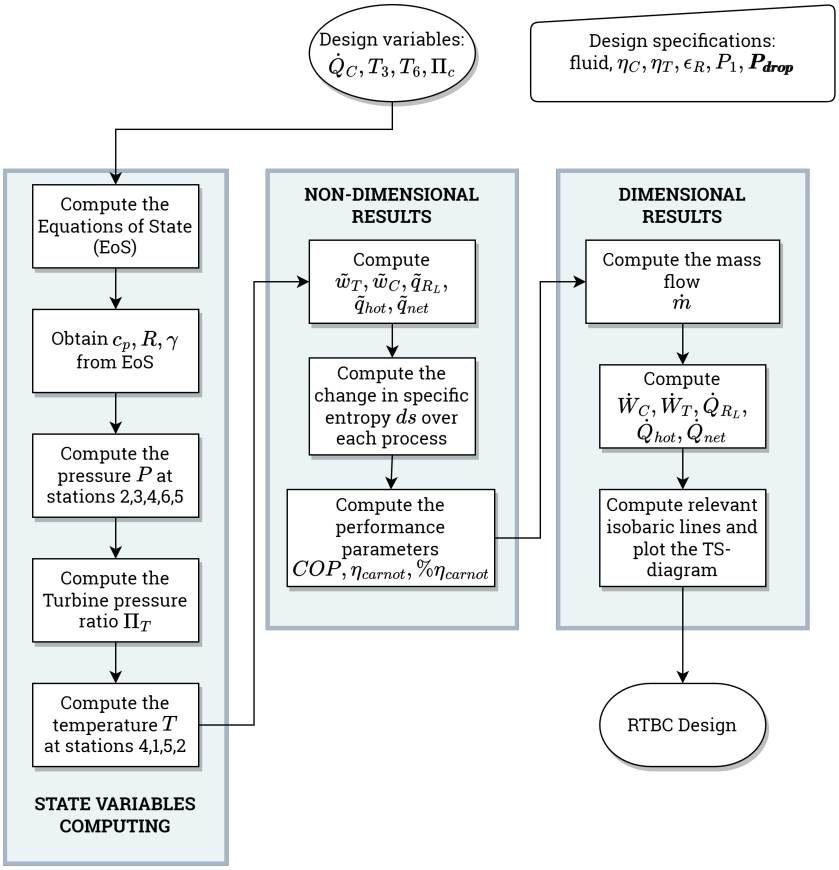

Figure 3.15: Flowchart of the RTBC system model

3.3.2. Subsystem model of the centrifugal compressor

This section documents the modelling and conceptual design of the high-speed miniature compressor in the RTBC. First, Local Dimensionless or Scaling Analysis (LDA) is explained. Following, the in-house model for the conceptual design is described at an executive level. The design and modelling of the compressor is then explained thereafter. Lastly, a parametric optimisation tool is presented that visualises the influence of the design variables during optimisation.

Conceptual design based on Scaling Analysis

Centrifugal compressors are generally designed based on a Global Dimensionless or Scaling Analysis (GDA). Scaling analysis provides a means to compute a set of dimensionless parameters from the problem variables, even if the final form of the equation is unknown. This is also known as the Buckingham π theorem. GDA assumes that the machine is a 'black-box', and makes use of the key overall performance parameters of the turbomachine. These are, for example, pressure ratio, efficiency, normalised mass flow rate and reduced speed. With this approach, the performance of a full-sized turbomachine can be analysed by testing a small-scale version. Furthermore, the off-design performance can be predicted using compressor (or turbine) maps. These maps show characteristic operating curves of a turbomachine, based on key overall dimensionless performance parameters.

By using a scaling analysis based on global parameters, a decision about the flow path type and shape of the velocity triangles is made at an early design phase. This in turn affects stage performance. Albeit this 'black-box' approach ensures scaling based on key parameters, it has no regard for optimal stage design. A different dimensionless approach is therefore preferred, namely Local Dimensionless or Scaling Analysis (LDA). Instead of considering global parameters, LDA focusses on dimensionless stage parameters that can be used to express stage performance parameters. These local stage performance parameters can in turn be used to express global performance parameters.

Using LDA, the main performance and characteristic parameters can be expressed as [38]:

$$\boldsymbol{y} = f(\Phi_{t1}, \psi, \alpha_2, \beta, \overline{\gamma_{P_v}}, Re, \boldsymbol{\sigma}) \tag{3.54}$$

In Equation (3.54), $\boldsymbol{y}$ is a vector containing the main performance and characteristic parameters of the compressor stage. This includes e.g. efficiency and operating range, and rotational speed and

impeller tip radius. The right hand side of Equation (3.54) entails information about the impeller flow angles, diffuser stability, work, thermodynamic behaviour of the fluid, viscous effects, and geometrical features. In classical similarity analysis, Equation (3.54) is referred to as the Classical Similarity Equation (CSE) [39].

The impeller flow angles dictating the velocity triangles are explicitly determined by the swallowing capacity

$$\Phi_{t1} = \frac{\dot{m}}{\rho_{t1} U_2 D_2^2}, \tag{3.55}$$

the work (or loading) coefficient

$$\psi = \frac{\Delta h_{tt}}{U_2^2}, \tag{3.56}$$

and the degree of reaction χ. The degree of reaction is replaced in Equation (3.54) by the absolute flow angle at the inlet of the diffuser α_2. By doing so, the parameter does not only complete the determination of the impeller flow angles, but can also be used to characterise diffuser stability. The work performed by the impeller is determined by the pressure ratio β and the thermodynamic behaviour of the fluid, which is expressed by the average value of the isentropic pressure-volume exponent [54]

$$\gamma_{P_v} = -\frac{v}{P}\frac{\delta P}{\delta v}\bigg|_s = -\frac{v}{P}\frac{c_p}{c_v}\frac{\delta P}{\delta v}\bigg|_T \tag{3.57}$$

over the compression process, denoted by $\overline{\gamma_{P_v}}$ [39]. The effects of viscosity are accounted for by the average Reynolds number within the impeller, diffuser, and volute. The last term on the right hand side of Equation (3.54), the vector $\boldsymbol{\sigma}$, represents the stage dimensionless geometrical characteristics. Since turbomachines in RTBC are on a very small scale, however, a few parameters in the vector $\boldsymbol{\sigma}$ are dimensional. Due to limits of manufacturability, some geometrical features are unable to be scaled and therefore need to be taken as dimensional.

One of the cornerstone equations of LDA is the dimensionless Euler equation, relating the compression ratio β_{tt} to the peripheral Mach number at the impeller outlet M_{U_2}, the thermodynamic behaviour of the fluid γ_{P_v}, and the work coefficient ψ. The dependency of compression ratio on M_{U_2} indicates not only a strong dependency on the peripheral speed U_2, but also the working fluid's speed of sound a_{t1}. The dimensionless Euler equation shown in Equation (3.58) can be used for design purposes, and for indications about off-design of turbomachinery. Most importantly, it provides a tool to select the working coefficient for a target pressure ratio, based on operating fluid and the peripheral speed threshold. Alternatively, it can be rewritten to correlate the impeller tip speed Mach number to the pressure ratio of a stage for a given work coefficient (Equation (3.59)).

$$\beta_{tt}^{\frac{\gamma_{P_v}-1}{\gamma_{P_v}}} = 1 + (\gamma_{P_v} - 1)\psi M_{U_2}^2 \tag{3.58}$$

$$M_{U_2}^2 = \sqrt{\frac{\beta_{tt}^{\frac{\gamma_{P_v}-1}{\gamma_{P_v}}} - 1}{\psi(\gamma_{P_v} - 1)}} \tag{3.59}$$

Centrifugal compressor model

At the Faculty of Aerospace Engineering of the Delft University of Technology, an in-house model for conceptual design of turbomachinery has recently been developed by Giuffré, Majer, and Pini based on LDA. The in-house reduced-order model is a python suite relying on the lumped parameters modelling approach. The model uses three design assumptions; the absence of Inlet Guide Vanes (IGV), the use of a backward-swept impeller, and the use of a vaneless diffuser. The design assumptions, including their advantages and disadvantages (Pini [76]), are listed in Table 3.6. Moreover, it includes the possibility of design optimisation in order to maximise total-to-total efficiency and operating range at design rotational speed. A detailed description of the model can be found in Giuffré, Colonna, and Pini [38].

The philosophy behind the model is to have a fully integrated compressor design process. That is, to integrate the design of the compressor stage(s) with the design of the system as much as possible. The in-house conceptual design model, therefore, uses as much details and advancements in compressor design as possible. For example, semi-empirical correlations are used for losses that are generally not included in conceptual design. This means that the conceptual design is very close to a working

product, and can be integrated into the system design with ease. After the integrated system design is performed, the compressor can be improved with CFD. This is a complete new design philosophy compared to current design methods, which use conceptual design based as an indication for a starting point, from which a detailed design is constructed that is integrated with the system (see Section 2.1.2).

The accuracy of the model has been assessed by comparing the predictions to three well-documented experimental test cases available in literature [29, 28, 30, 51, 87], and with CFD simulations of a new compressor prototype developed by the in-house model itself [37]. Two of the three test cases are large centrifugal compressors having air as working fluid [29, 28, 30, 51]. One test case [87] and the CFD analysis [37] represent small scale centrifugal compressors working with non-standard fluids, such as the compressors generally used in RTBC. The result of the validation study is that more than 95% of the experimental and CFD data are within the $\pm$5% uncertainty bands from the values predicted by the in-house reduced-order model [38, 37].

Table 3.6: Design assumptions of the in-house reduced-order compressor model, including their advantages and disadvantages [76]

Design Assumption	Advantages	Disadvantages
No Inlet Guide Vanes	Axial and vortex free inflow	High blade twist
		High inlet tip speed Mach number
Backward-swept impeller	Reduced absolute flow velocity	Lower work input
	Lower flow diffusion	Lower specific work
	High efficiency	Higher blade speed
	Stable operation	Higher stresses
Vaneless diffuser	Simple concept	Low efficiency
	Low manufacturing cost	
	Large operating range	

Centrifugal compressor design

The conceptual design of the centrifugal is performed based on ten design variables, and a specific working fluid. In Figure 3.16, the meridional view of the centrifugal compressor considered in the in-house model is shown. The subscripts used for the design variables are consistent with the stations showed in Figure 3.16. The ten design variables used for the conceptual design are the swallowing capacity

$$\Phi_{t1} = \frac{\dot{m}}{\rho_{t1} U_2 D_2^2}\,, \tag{3.60}$$

the isentropic loading coefficient

$$\psi_{is} = \frac{\Delta h_{tt,is}}{U_2^2}\,, \tag{3.61}$$

the total-to-total pressure ratio β_{tt}, the mass flow rate $\dot{m}$, the impeller shape factor

$$k = 1 - \left(\frac{R_{1,h}}{R_{1,s}}\right)^2\,, \tag{3.62}$$

the impeller outlet absolute flow angle α_2, the number of blades N_{bl}, the diffuser ratio R_3/R_2, and the non-dimensional parameters characterising the shape of the diffuser, namely the diffuser blade height ratio

$$H_{r,pinch} = \frac{H_3 - H_2}{H_2(R_2/R_{pinch} - 1)}\,, \tag{3.63}$$

and the diffuser pinch radius ratio

$$R_{r,pinch} = \frac{R_{pinch} - R_2}{R_3 - R_2}\,. \tag{3.64}$$

These 10 design variables are summarised in Table 3.7, including their typical range. Note that the first four variables set the overall stage design ($\Phi_{t1}, \psi_{is}, \beta_{tt}, \dot{m}$), the three thereafter complete the impeller design (k, α_2, N_{bl}), and the last three determine the diffuser design ($R_3/R_2, H_{r,pinch}, R_{r,pinch}$). Next to these design variables and the specification of the working fluid, the model requires reduced total inlet conditions (P_r and T_r), and a vector of geometrical parameters related to production constraints, e.g. thicknesses and clearances. Note that all variables and parameters, except the mass flow rate, are gathered into the CSE (Equation (3.54)) of the LDA. The mass flow rate is used to scale the design to its intended application. Instead of the mass flow rate, it can be decided to use the size parameter [38]:

$$SP = \frac{\dot{V}_1^{1/2}}{\Delta h_{ts}^{1/4}}. \tag{3.65}$$

Table 3.7: The 10 design variables of the conceptual compressor design

Description	Definition	Typical range
Swallowing capacity	$\Phi_{t1} = \frac{\dot{m}}{\rho_{t1} U_2 D_2^2}$	0.05-0.2
Isentropic loading coefficient	$\psi_{is} = \frac{\Delta h_{tt,is}}{U_2^2}$	0.6-1.2
Total-to-total pressure ratio	β_{tt}	2-8
Mass flow rate	$\dot{m}$	0.05-0.25 kg/s
Impeller shape factor	$k = 1 - \left(\frac{R_{1,h}}{R_{1,s}}\right)^2$	0.65-0.95
Impeller outlet absolute flow angle	α_2	60°-75°
Number of blades	N_{bl}	10-20
Diffuser radius ratio	R_3/R_2	1.2-2.0
Diffuser blade height ratio	$H_{r,pinch} = \frac{H_3 - H_2}{H_2(R_2/R_{pinch} - 1)}$	0.0-1.0
Diffuser pinch radius ratio	$R_{r,pinch} = \frac{R_{pinch} - R_2}{R_3 - R_2}$	0.0-1.0

As the model is based on a lumped parameters approach, the flow quantities and main dimensions of the compressor are lumped at each of the stream-wise stations shown in Figure 3.16. At each station, the thermo-physical fluid properties are evaluated through the NIST reference thermodynamic library (also known as REFPROP) [58]. The incoming flow is assumed to be uniform and axial (no IGV). At the impeller inlet, the flow quantities are evaluated at five span-wise locations, to account for different peripheral speed and to capture the free-vortex flow distribution. The velocity triangle at the inlet station is determined by the selection of swallowing capacity Φ_{t1}, and minimisation of the local relative Mach number at the inducer shroud (Rusch and Casey [85]). The initial guess of the velocity triangle at station 2 is determined by the selection of the outlet absolute flow angle α_2 and the isentropic loading coefficient ψ_{is}. The true work coefficient is then iterated to match the target total-to-total pressure ratio β_{tt}, adjusting for slip and losses. Slip is accounted for by a semi-analytical model (Qiu et al. [80]), whilst losses are predicted by a set of semi-empirical correlations (Giuffré, Colonna, and Pini [38]). Splitter blades are considered in the impeller design when the throat length is smaller than a user-defined threshold, as to ensure manufacturability. The vaneless diffuser is assumed to be pinched close to the diffuser inlet, in order to delay rotating stall inception. The flow in the diffuser is modeled by integration of a set of two-dimensional differential equations (Stanitz [88]). The volute is assumed to have no friction and no pressure gradient in the circumferential direction, such that conservation equations can be used for its design (Casey and Robinson [15]).

Geometrical parameters related to production constraints are documented in Giuffré, Colonna, and Pini [37]. These manufacturability constraints are for blade thicknesses and clearances in miniature high-speed aluminium twin-stage compressors for the Environmental Control System of Next-Gen aircraft. Turbomachinery for RTBC are the smallest high-speed equipment manufactured to date, requiring different materials and higher manufacturing precision. In accordance with dimensions in literature (Zagarola et al. [100] and Cragin, McCormick, and Zagarola [21]), all manufacturing constraints are lowered to be a third of their original value as used by Giuffré, Colonna, and Pini [37]. The new values are presented in Table 3.8. The effect of this dimensional decrease will be investigated by a sensitivity study based on the final obtained design (Section 4.3.3). Additionally to the geometrical parameters presented in Table 3.8, surface roughness is also considered as a dimensional parameter. Due to

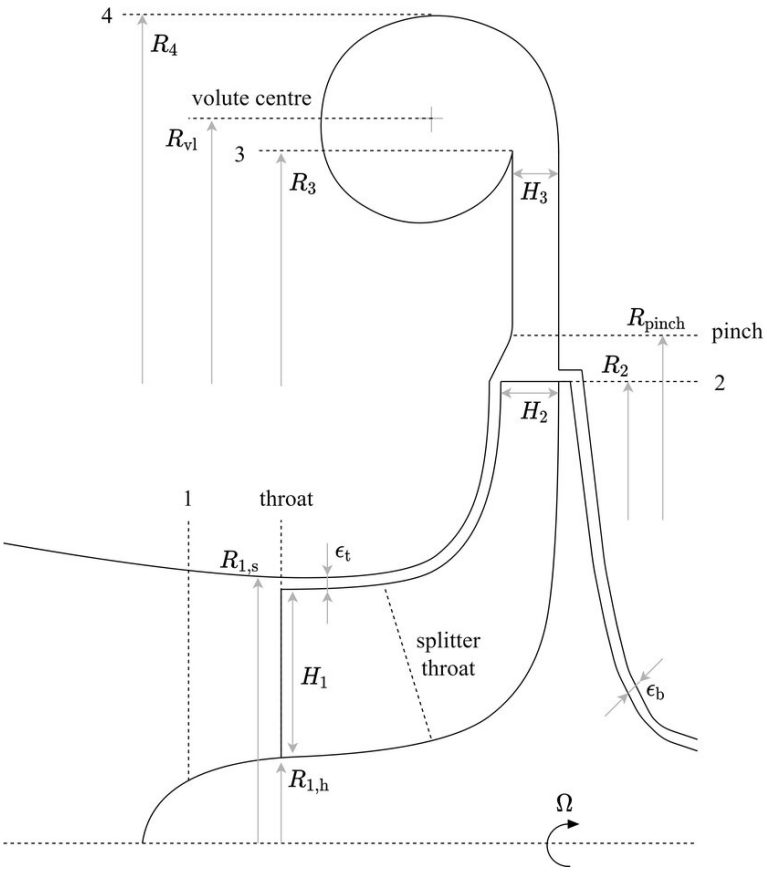

Figure 3.16: Meridional view of a centrifugal compressor stage featuring splitter blades, pinched vaneless diffuser, overhung volute, and no inlet guide vanes [38]

limited data on manufactering constraints of surface roughness for turbomachinery in RTBC, this parameter is not changed from the original value in the in-house reduced-order compressor model. The effect of this surface roughness, however, is studied upon in the sensitivity study in Section 4.3.3.

Table 3.8: Geometrical dimensional parameters related to manufacturing constraints

Parameter	Value	Parameter	Value
$t_{bl,h}$	0.2 mm	$t_{bl,s}$	0.1 mm
$\epsilon_{t,1}$	0.05 mm	$\epsilon_{t,2}$	0.05 mm
ϵ_b	0.05 mm		

In addition to the conceptual design of a centrifugal compressor, the model can compute the operating map of a design once the main dimensions have been computed. The procedure to do so is well documented by Giuffré, Colonna, and Pini [38]. It is not described here, as off-design is not the main focus of this research.

Component-wise Multi-Dimensional Parametric Design Optimisation

The in-house reduced-order model has the ability to perform multi-objective design optimisation. This design optimisation problem consists of design variables, inequality constraints, and two objectives [38]. These two objectives are a maximum total-to-total efficiency η_{tt} and a maximum operating range defined by

$$OR = \frac{\dot{m}_{choke} - min(\dot{m})}{\dot{m}_{des}}. \tag{3.66}$$

An interested reader is referred to Giuffré, Colonna, and Pini [37, 38] for extra information and applications. An unfortunate result of the multi-objective design optimisation, is that the influence of the design variables on the optimisation objectives cannot be assessed effectively. That is, multi-objective

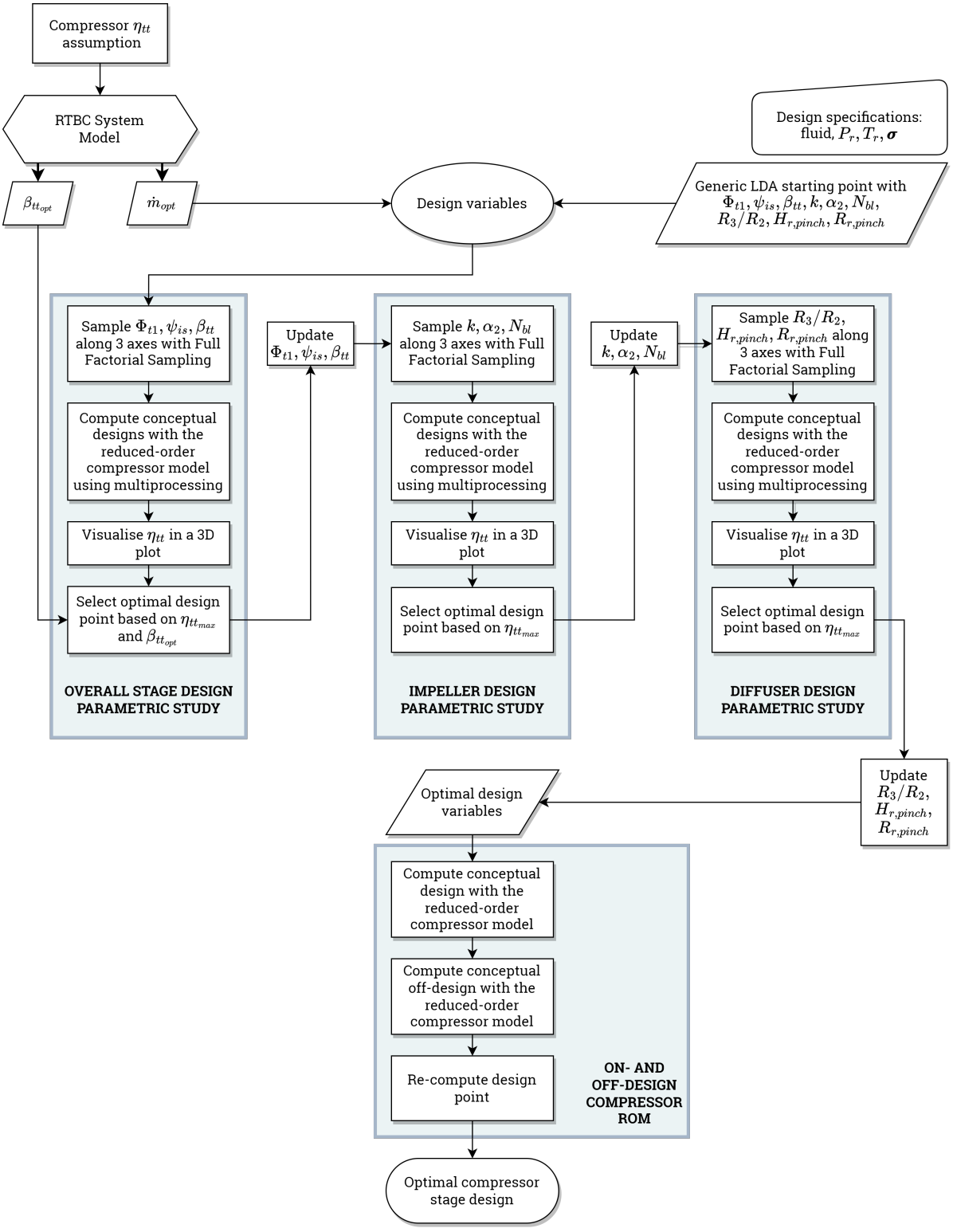

Figure 3.17: Flowchart of the component-wise multi-dimensional parametric design optimisation procedure. A flowchart of the on- and off-design compressor rom is displayed in Figure 3.18

optimisation algorithms generally behave like a 'black box'. The optimisation algorithm will find a Pareto front with corresponding design vectors. From these results, it is generally not apparent how much weight each variable has on the optimisation objectives, nor the trends of inter-variable correlations. For the purpose of this research, however, a clear understanding of the performance trends, variable importance, and inter-variable correlation is incredibly important. To document the influence that the design variables and parameters have on the design whilst still obtaining an optimised design, a Multi-Dimensional Parametric Design Optimisation Tool (MDPDOT) has been developed.

The MDPDOT is a tool that can be used to visualise multi-dimensional parametric studies. It samples the variables the user is interested in along a maximum of three axes, using Full Factorial Sampling. At each design point, the design routine is performed, and the performance of the compressor is computed at the design rotational speed. This is done using process-based parallelism (multiprocessing in Python), to save expensive computational effort. When the parametric study has been completed, an optimal design is chosen, the off-design performance computation for this design is performed, and the design point is re-computed.

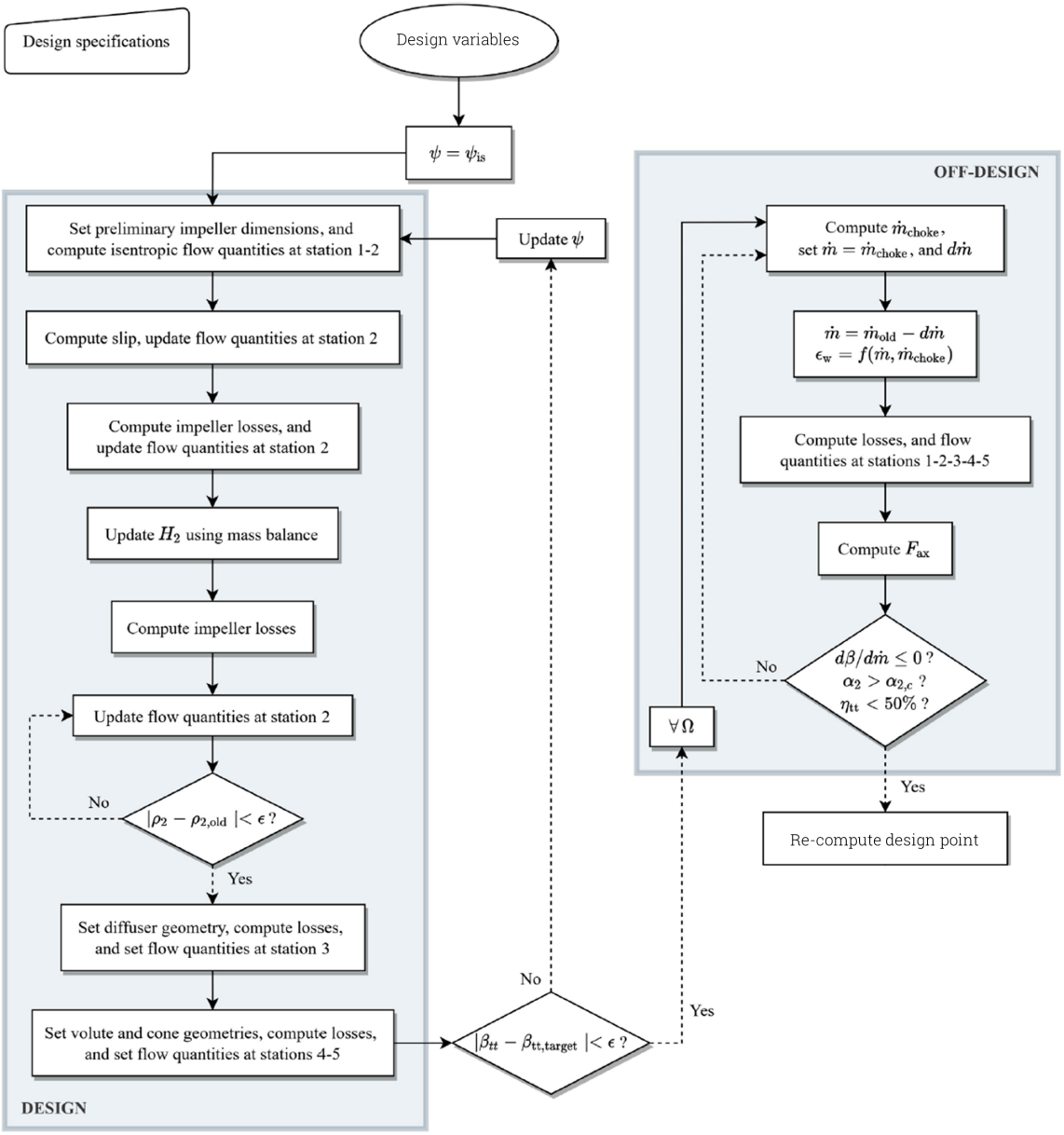

Figure 3.18: Flowchart of the reduced-order compressor model: design and off-design. The symbol ϵ refers to the tolerance prescribed in the algorithm [38]

As shown in Table 3.7, the design space of a conceptual compressor is composed of 10 variables. The mass flow, however, is not needed to express the main performance and characteristic parameters, as can be seen in the CSE (Equation (3.54)). The mass flow is functioning as a scaling variable for the LDA, and is therefore not considered in the parametric study. In order to quantify dimensional results, however, the mass flow for maximum RTBC system efficiency (see Section 3.3.1) is used as fixed parameter. The first three of the remaining design variables set the overall stage design ($\Phi_{t1}, \psi_{is}, \beta_{tt}$), the three thereafter dictate the impeller design (k, α_2, N_{bl}), and the last three determine the diffuser design ($R_3/R_2, H_{r,pinch}, R_{r,pinch}$). This division of the design space into three component-wise design spaces consisting of three design variables enables component-wise multi-dimensional parametric design optimisation.

The sequence in the MDPDOT is based on component importance and flow direction. First the MDPDOT is used to perform a parametric study based on overall stage design from a generic starting design point. From this study, the optimal design point is picked constrained by the given total-to-total pressure ratio for maximum RTBC system efficiency (see Section 3.3.1). Starting from this point, MDPDOT is used to perform a parametric study based on impeller design. Again, the optimal design point is selected. This design point is used with the MDPDOT to perform a parametric study on diffuser design. Finally, the optimal design point is selected. The off-design performance computation for this design is performed, and the design point is re-computed. A flowchart of this procedure is shown in Figure 3.17. Additionally, a flowchart of the on- and off-design compressor reduced order model (ROM) marked by the last three blocks in the figure is displayed in Figure 3.18.

3.4. Verification and Validation

This section presents the verification and validation of the created and used models in this research. Verification and validation is an important step in the creation of a model. It serves in assessing the correct working of a model, and the accuracy of the predictions a model makes. The approach to verification and validation can differ per research and sector. The definitions adhered to in this research are (Colonna et al. [17] and Computational Fluid Dynamics Committee [19]):

> **Verification:** *a procedure to check if a model is correctly implemented and represents its conceptual description.*
>
> **Validation:** *a procedure to assess a model's capability to reproduce the actual process in the real world.*

The section is structured as follows. First, the verification and validation of the liquid hydrogen fuel tank is presented in Section 3.4.1, using two verification cases and one validation case. Second, the verification and validation for the Reverse Turbo-Brayton Cryocooler system model is presented in Section 3.4.2. The verification and validation of the in-house conceptual compressor model by its authors has been briefly summarised with the model description in Section 3.3.2, and will not be discussed again in this section.

3.4.1. Verification and Validation of the Liquid Hydrogen Fuel Tank Model

In literature, hardly any data for verification and validation exist for the modelling of boil-off for an actively cooled cryogenic two-phased mixture tank with pressure control. Despite the absence of data, two verification cases and one validation case are discussed. The verification of the model is part of the research in this report. The validation case of the model has been set up by another MSc student of the research group Propulsion & Power, Faculty of Aerospace Engineering at the Delft University of Technology. The case is a zero boil-off duty cycle test for a large-scale ground operated liquid hydrogen tank, where the active cooling cycled off and on. A discussion about the obtained data is presented at the end of this subsection, and is part of the research.

The verification of the liquid hydrogen fuel tank model is performed in three steps. First, *error evaluation* is performed. The code behind the model is checked on bugs, incorrect implementation, errors in communication between code environments, error in inputs and other errors and bugs. Dymola provides an option to check for syntactic, semantic and pedantic errors. This highlights the origin of the error, warning, or other message. Additionally, errors can arise during translation, initialisation or simulation of the model. When the error evaluation is successfully performed, *consistency checks* are performed. This examines expected relationship between inputs and results. Examples are checking the conservation equations or checking fluid behaviour based on the fluid state variables. Finally, when the code contains no errors and is consistent, *highly accurate verification cases* are simulated. Although error evaluation and consistency checks are the most tedious and time consuming parts for a newly developed model with external coding environments and a high number of complex relations, these are not discussed in this report. Instead, two verification cases are discussed. The first case is a textbook example of a spherical nitrogen container, simulating the boil-off of a one-phased fluid based on thermal circuits. The second case is a theoretical study performed by NASA to estimate the size and performance of hydrogen storage systems for aircraft applications. In this study, the effect of insulation thickness on total tank and boil-off mass is analysed with theoretical relations.

Spherical nitrogen tank verification case

The first verification case is example 3.6 in the textbook "Fundamentals of Heat and Mass Transfer" by Incropera et al. [49], and is depicted in Figure 3.19. In the example, the heat transfer rate and boil-off

is calculated for a spherical, thin-walled metallic container storing liquid nitrogen. The nitrogen is one-phased, and at a temperature of 77 K. The tank has a radius of 0.25 meter, and is exposed to ambient air at 300 K, with a constant convection of 20 W/m^{2}K. The insulation is a layer of 25 mm thick reflective evacuated silica powder, with a heat conductivity of 0.0017 W/mK. The heat transfer to the nitrogen is modelled with thermal resistance circuits. The boil-off is calculated by dividing the heat transfer to the nitrogen by its latent heat of vaporisation. Moreover, the following assumptions are used:

1. Steady-state conditions apply.
2. Heat transfer is one-dimensional and in radial direction.
3. The heat transfer resistance through the container wall and to the nitrogen is negligible.
4. The fluid and ambient properties are constant.
5. External radiation is negligible.

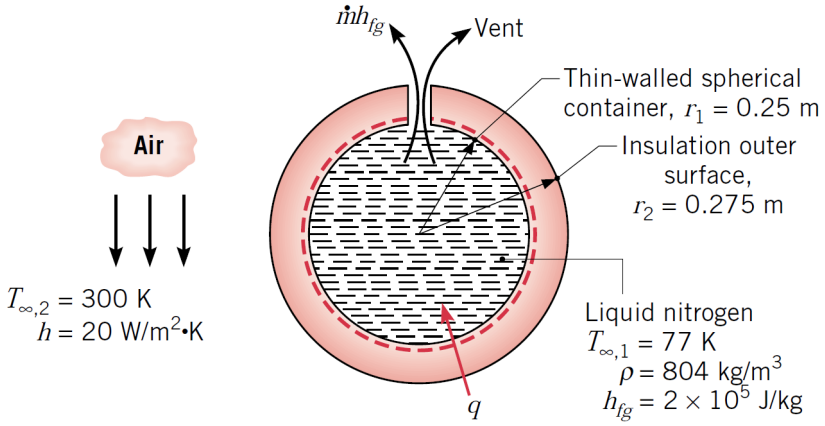

Figure 3.19: Schematic of the nitrogen tank verification case [49]

The liquid fuel hydrogen tank model developed in this research is much more complex, and differs greatly on assumptions. Moreover, the model is cylindrical, two-phased, dynamic and has fluid behaviour as output instead of input. By cleverly choosing inputs to the model, however, this verification case can be mimicked. First, the fill fraction is set to 99.98% such that a negligible amount (0.02%) of vapour is present in the tank, such that the case becomes practically one-phased. Second, the metallic wall thickness is reduced to a minimum such that it has a negligible effect on the heat transfer. Third, all sub models and components apart from the two-phased hydrogen mixture container component are modelled as spherical sections. This is readily available in the model, as the end caps on the cylindrical tank are modelled as spherical domes. Lastly, the simulation is conducted for an hour and average results are taken over this period without considering the initial 60-second transient.

Unfortunately, the parameterisation of the cylindrical two-phased hydrogen mixture container component prohibits the use of a spherical fluid mixture model. As changing the parameterisation will change most of the relations in the two-phased mixture component, a different solution is proposed. That is, the internal volume and internal area of the tank are matched with the spherical case. This ensures a similar heat transfer and fluid behaviour, except for the change of fluid level with boil-off (which is still calculated based on a cylinder). Since the tank fill fraction is close to 100% and the boil-off is minimum, the effects of the incorrect fluid level relation are deemed negligible.

A summary of the verification case is presented in Table 3.9. In this table, the parameters of the theoretical example and the model are presented with the differences expressed in percentage. Note that the fluid state characteristics (temperature, pressure, etc.) are an input to the theoretical example, but an output of the model. The results show differences all below 0.5%, which is deemed negligible. This close resemblance of the results was expected, as all of the assumptions of the theoretical model are applied to or mimicked in the model. The extremely small error can be contributed to the fluid having two phases, and that some heat is absorbed by the small amount of vapour in the spherical container. The liquid level, determining the ratio of heat that is absorbed by the vapour or liquid, contributes slightly to this error.

An interesting observation, is that the model confirms the assumption that the heat transfer resistance from the wall to the nitrogen is negligible. Indeed, the results show that the heat transfer coefficient from the wall to the liquid is in the order of 10^2 W/m^{2}K, and from the wall to the vapour in the

Table 3.9: Summary of the spherical nitrogen tank verification case parameters

Case parameter	Theoretical example	Model	Difference
Tank characteristics			
Shape	Spherical	Spherical/Cylindrical[1]	-
Inner radius	0.25 m	0.25 m	-
Outer radius	0.275 m	0.27501 m	0.00%
Tank wall thickness	Thin-walled	1×10^{-5} m	-
Tank wall material	Metallic	Aluminium 2014-T6	-
Tank wall conductivity	Negligible resistance	154 W/mK	-
Insulation thickness	0.025 m	0.025 m	-
Insulation material	Evacuated silica powder	Evacuated silica powder	-
Insulation conductivity	0.0017 W/mK	0.0017 W/mK	-
Venting pressure	1.0 atm	1.0 atm	-
Atmospheric conditions			
Fluid	Air	Air	-
Temperature	300 K	300 K	-
Pressure	1 atm	1 atm	-
Heat transfer	Convection	Convection	-
Convective heat-transfer coefficient	20 W/m^{2}K	20 W/m^{2}K	-
Fluid characteristics			
Fluid	Nitrogen	Nitrogen	-
Fluid phase	One-phased	Two-phased	-
Fill fraction	100%	99.98%	-0.02%
Fluid temperature	77 K	77.355 K	0.46%
Fluid pressure	1.0 atm	1.0 atm	0.00%
Fluid density	804 kg/m^3	805.9 kg/m^3	0.24%
Fluid latent heat of vaporisation	2×10^5	1.99×10^5	-0.41%
Heat transfer rate & boil-off			
Heat transfer rate	13.06 W	13.02 W [2]	-0.31%
Boil-off	6.53×10^{-5} kg/s	6.52×10^{-5} kg/s [2]	-0.15%

order of 10^2-10^3 W/m^{2}K. This high heat transfer coefficient is explained by the high Rayleigh number of cryogenic nitrogen. Cryogenic nitrogen has a low dynamic viscosity, with a density close to that of water at 300K. For hydrogen, the heat transfer coefficient is expected to be slightly lower due to its much lower density and slightly lower dynamic viscosity. Furthermore, the effects of superheated vapour are negligible and the heating configuration in both the theoretical case and the model is equal and uniformly distributed (constant natural convective heat transfer). The differences of the model with theory in the order of a factor 2-6 as explained in Section 2.2.5 are therefore not applicable.

[1] See the text of this section for detailed explanation of the model tank parameterisation
[2] Average value over the first hour, without considering the initial 60-second transient

The NASA hydrogen storage for aircraft verification case

The second verification case is a study performed by NASA at the Glenn Research Center [18]. The study explored options for storing gaseous hydrogen, cryogenic hydrogen, and chemically bound hydrogen for aircraft applications. Included are studies on tank design, material selection, cryocoolers and more. One of the analyses in the report is about the effect of insulation thickness on the overall tank system weight (including boil-off) of a cryogenic hydrogen storage tank with a venting system. The analysis makes use of one dimensional heat transfer analysis, as shown in Figure 3.20. Note that the tank has an outer insulation layer, and an inner tank wall carrying the loads. The tank is assumed to be in an isolated environment, such that only natural convection and radiation are present. Furthermore, it is assumed that the heat transfer to the inner tank wall is equal to the heat transfer to the hydrogen mixture. Once the surface temperature of the outer insulation layer is known, the heat transfer to the internal hydrogen mixture is calculated by one-dimensional radial conduction through the insulation layer. The boil-off is then calculated by dividing the heat transfer to the inner wall by the latent heat of vaporisation of the hydrogen.

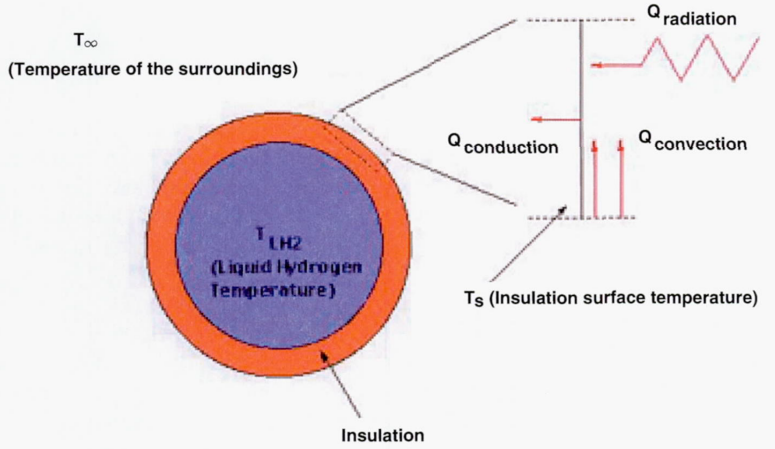

Figure 3.20: Schematic of the one dimensional heat transfer of the liquid hydrogen tank of the NASA hydrogen storage for aircraft verification case [18]

Results are shown in the report for a duration of 8 hours, for 4 tank designs determined by the mass of hydrogen stored in kilograms. Apart from the mass of the stored hydrogen and its storage duration, no more inputs are given. The verification is therefore performed qualitatively, to check if the model produces the same trends. In the report by NASA multiple insulation types and tank materials are provided, accompanied by some typical values for venting pressure and fill fraction. Additionally, equations for the tank wall thickness and volume of the tank are provided.

Numerous variation of possible input parameters were tried for 4 stored hydrogen masses, i.e. 1660 kg, 830 kg, 210 kg and 40 kg. One combination of input parameters produced matching results, which is shown in Figure 3.21. This plot shows the variation of the tank mass plus boil-off mass, varying with the insulation thickness. This trend effectively shows the mass of the tank system that cannot be used as a fuel versus the insulation thickness for a specified (initial) mass of hydrogen. Note that the different hydrogen masses have different tank designs, tailored to the amount of hydrogen stored. A summary of the input parameters for each tank design is shown in Table 3.10. The internal radius and thickness of the tank wall for each design is determined based on Equation (3.67), where V_t is the volume of the tank, r_i the internal radius, L the length of the cylindrical part of the tank, t_w the tank wall thickness, P the pressure in the tank, and FoS and σ_y the tank wall material Factor of Safety, and yield strength respectively.

$$V_t = \frac{4}{3}\pi r_i^3 + \pi r_i^2 L \qquad t_w = \frac{r_i P FoS}{2\sigma_y} \tag{3.67}$$

An important note is that the NASA report provides a thermal conductivity of evacuated silica powder of 0.17×10^{-3}. This value is, however, not used for the model. Rettelbach et al. have performed extensive research about evacuated silica powders in the 1990s. They found experimentally that thermal conductivities for silica powders are in the range of 0.1×10^{-3} W/mK at 20 K to 3×10^{-3} W/mK at 275 K [81]. Since temperatures in the insulation layer are ranging from 20 K to around 290 K, a mean value of the thermal conductivity is used instead of the value at the lowest temperature. In Rettelbach et al.

Table 3.10: Summary of the NASA hydrogen storage for aircraft verification case input parameters

Case parameter	Model input
Tank characteristics	
Shape	Cylindrical tank with end domes
Length of the cylindrical part	5 m
Venting pressure	1.45 bar
Fill fraction	0.928
Tank wall characteristics	
Tank wall material	Steel (ASTM-A514)
Tank wall yield strength	690 MPa
Tank wall density	7860 kg/m^3
Tank wall conductivity	52 W/mK
Tank wall Factor of Safety	1.5
Insulation characteristics	
Insulation material	Evacuated silica powder
Insulation conductivity	0.0017 W/mK
Insulation density	160 kg/m^3
Environmental conditions	
Heat transfer	Radiation & free convection
Altitude	0 [m]
Date & time	18-06 14:00
Geographical location (lat / long)	41.4° / -81.86°

[82], mean values for different evacuated silica powders with an inner temperature of 20.4 K and an outer temperature of 290 K are experimentally obtained. These values are in the range of 1.3-1.9$\times 10^{-3}$ W/mK. In accordance with Incropera et al. [49], a value of one order of magnitude bigger is chosen than the one reported in Colozza [18]. The thermal conductivity is therefore taken to be 1.7$\times 10^{-3}$ W/mK.

Figure 3.21 shows a excellent correspondence between the model results (solid lines) and the NASA predictions (dotted lines). For all tank designs, except 1600 kg, the curves have a satisfactory agreement. The lower two curves over-predict the boil-off slightly but show the same trends. For the 830 kg of hydrogen, the curve corresponds well with the theoretical data, but over-predicting the total mass slightly for lower insulation thicknesses. For the 1660 kg of hydrogen, the total mass is over-predicted for lower insulation thicknesses and under-predicted for higher insulation thicknesses. The trend for this hydrogen mass is corresponding for insulation thicknesses below 5 mm and above 20 mm. In between, the location of minimum total tank and boil-off mass differs whereas the minimum value corresponds well. The reason for the higher predicted total mass for low insulation thickness might be due to the model using a mean thermal conductivity value between 20-290 K, whereas for a low insulation thickness the outer temperature of the insulation layer might be far below 290 K. This decrease in mean insulation temperature also decreases the thermal conductivity, however, this is not taken into account by the model.

This shift of minimum total tank and boil-off mass to higher insulation thickness by the model is seen for all four curves and is the most prominent difference in the results. This can be due to numerous factors related to heat transfer, such as a lower used mean thermal conductivity of the insulation with decreasing insulation thickness, or different external heat transfer coefficients and conditions. All in all, with the degree of uncertainty of the inputs to the model this graph shows not only qualitatively but also quantitatively great correspondence of the model to the verification case.

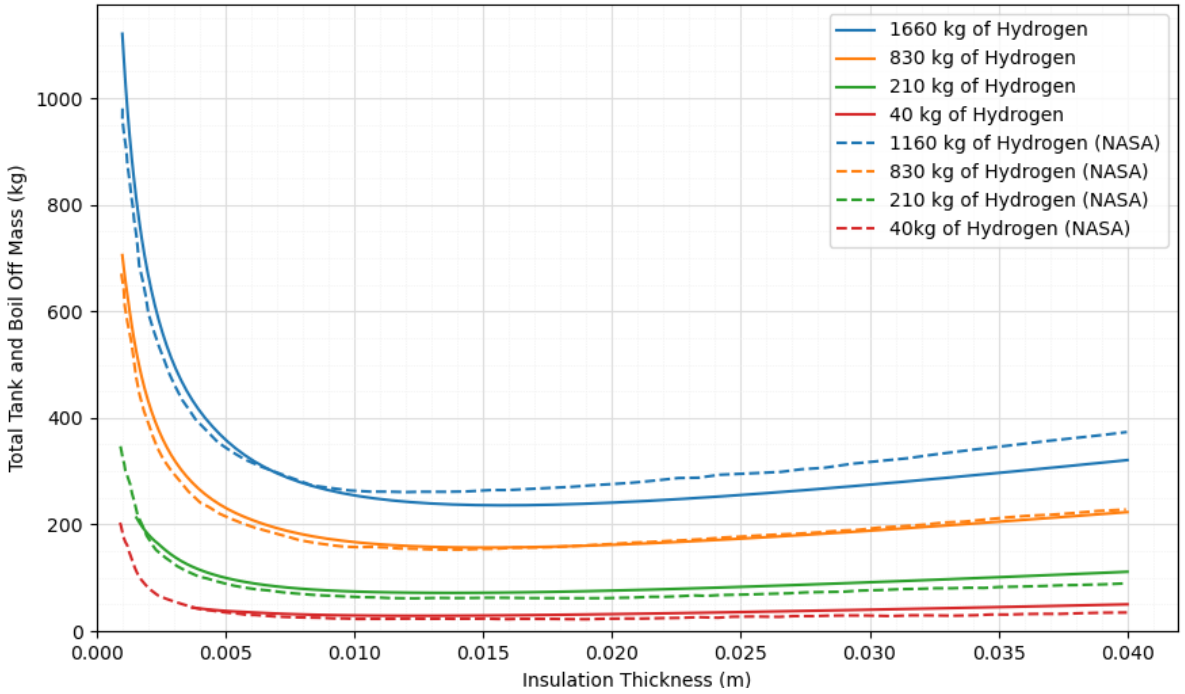

Figure 3.21: Effect of insulation thickness on overall tank system weight (including boil-off mass), for various tank designs. The solid lines are results from the model, the dotted line denoted with NASA are the verification case predictions [18]

Validation case

In an effort to explore zero boil-off methods for large-scale liquid hydrogen tanks, NASA has built and tested a Ground Operations Demonstration Unit for Liquid Hydrogen (GODU LH2) [72]. Part of this study was a series of duty cycle tests, which cycled the active cooling off and then on. The case considered in the validation is the data of a test at 33% fill level, which was performed due to the unintentional cooler shut-down during a temperature control test. The test was performed between August 4, 2015 and August 10, 2015. During the test, the cooling was switched off for the first 80 hours. At 80 hours, the cooling was turned on until the end of the testing period. Data was gathered about the pressure variation, and the temperature at various sensors distributed vertically in the tank. The set-up of the validation, model simulation and result visualisation has been performed by another MSc student of the research group Propulsion & Power, Faculty of Aerospace Engineering at the Delft University of Technology, and is presented in Figure 3.22. As the model only has one CV for the vapour, the average vapour temperature is computed and plotted as reference.

A clear observation can be made from the test data. During the first 80 hours, an immediate stratification in the vapour can be observed. This rise in vapour pressure increases the pressure, until the cooling is activated. This quickly de-stratifies and cools down the mixture, decreasing the pressure. The liquid stratifies slightly, with only a small temperature difference between the two bottom temperature sensors.

As seen in Figure 3.22, the model predicts a liquid temperature that falls within the two temperature sensors positioned in the liquid. The vapour temperature, on the other hand, is under-predicted by the model. As a result of the lower vapour temperature, the pressure is under-predicted as well. Both the pressure and temperature predictions by the model show the same behaviour when the cooling is turned on. A slight difference in the initial pressure and temperature decrease exists, as the model does not account for stratification. As the model predicts the vapour to be at a lower temperature, the duration of the initial pressure and temperature decrease is smaller than experimentally obtained. At 100 hours, when the initial pressure and temperature decrease is over and flattens off, the model predicts a similar decreasing vapour trend. This shows in the pressure trend, which matches that of the experimental data closely from 100 hours onwards.

The source of the model deviation from the experimental data are the internal heat transfer relations from the wall towards the two-phased hydrogen mixture. As elaborated in Section 3.2.5, the heat transfer relations are obtained from a NASA heat transfer model from the 1980s [46, 91, 94]. This was at the time a simple correlation for natural convection in an enclosure, that ensured a broad range of model applications (i.e. both various space and aeronautical applications). The effect of using this correlation is the over-estimation of heat transfer to the liquid compared to the heat transfer towards

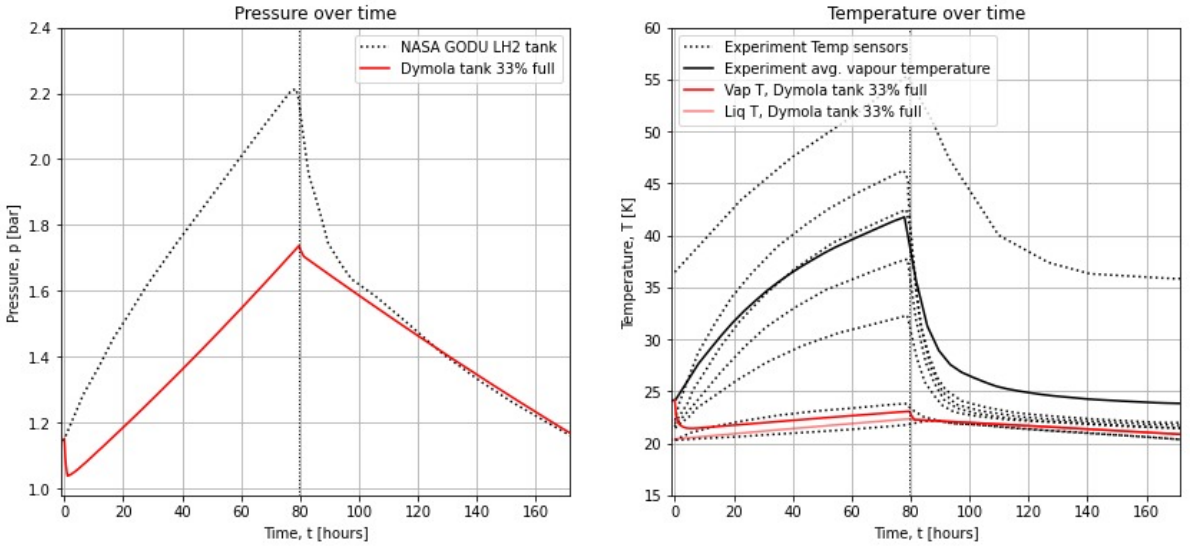

Figure 3.22: Validation data of the liquid hydrogen fuel tank, as visualised by another MSc student of the research group Propulsion & Power, Faculty of Aerospace Engineering at the Delft University of Technology

the vapour.

In Section 2.2.5, the importance of capturing the behaviour of superheating of the vapour for aeronautical applications has been discussed. Due to the under-prediction of the superheating of the vapour, the model over-predicts the boil-off and vented mass [5]. The main reason for over-prediction of boil-off is the over-prediction of heat transfer towards the liquid. Additionally, the lower predicted pressure decreases the saturation temperature. This does not only increase heat transfer to the liquid, but also accelerates the moment when boil-off starts to occur. The over-prediction of vented mass might seem counter intuitive, as the pressure is under-predicted. Indeed, the model will predict a postponed start of venting operations. When the venting starts to occur, however, vapour is vented with a lower temperature. This does not only increase the density of the vented hydrogen, but also decreases the enthalpy of the vented hydrogen. This results in a higher mass being removed from the tank during venting, whilst lowering the heat removal. As a result, more high-density hydrogen needs to be vented to reduce the same amount of internal energy and the total vented mass is over-predicted. All the aforementioned behaviour is seen in the model predictions and confirmed by experimental data [5].

The result of the validation, is that despite the model having been verified, the boil-off and vented mass predictions of the model are conservative. That is, the model over-predicts the liquid hydrogen being lost during the mission duration due to boil-off and venting. In contrast, both pressure and temperature are under-predicted. As the model is verified, and the implications of the validation are known, the model can be used for further research. It is, however, recommended that new experiments are performed with the purpose of establishing adequate heat transfer correlations for a cryogenic two-phased mixture in a finite volume. Furthermore, it is recommended to study the possibility of including stratification in the model without over-complicating the model, such that it can still be used in the conceptual design phase. Note that, as described in Section 3.2.2, conversion of para- to ortho-hydrogen is not taken into account by the model. This conversion from para- to ortho-hydrogen between 50K-200K can take up a significant amount of heat input [91], due to which the model could over-estimate boil-off for cases with superheated vapour above 50 K even more.

Note in Figure 3.22 that the upper experimental temperature sensor curve in the right plot deviates from all other temperature sensors in starting value, trend, and end value. This curve might correspond to the pressure curve of the data presented by Notardonato et al. [72], or it resemblance a faulty temperature sensor. This curve should, therefore, not be considered in the computation of the average vapour temperature. The actual average vapour temperature is therefore lower than indicated in Figure 3.22. This results in a closer match of the model with the validation data than suggested by the figure.

Note furthermore that the simulation starts with an initial decreasing transient. This is either due to a false equilibrium starting condition, or by a fixed state initialisation with a wrong starting vapour temperature. Due to the decrease in the high starting vapour temperature, the pressure decreases in the initial transient. It is recommended that the validation is redone with correct starting conditions to eliminate this artificial initial transient.

3.4.2. Verification and Validation of the Reverse Turbo-Brayton Cryocooler system model

The verification of the the Reverse Turbo-Brayton Cryocooler system model is performed in three steps, similar to the liquid hydrogen fuel tank model. First, *error evaluation* is performed. The code behind the model is checked on bugs, incorrect implementation, errors in communication between code environments, error in inputs and other errors and bugs. When the error evaluation is successfully performed, *consistency checks* are performed. This examines expected relationship between inputs and results. Examples are checking that the first and second law of thermodynamics hold and plotting TS-diagrams of the process the fluid undergoes. The error evaluation and consistency checks are not discussed in this report.

Finally, when the code contains no errors and is consistent, *highly accurate verification cases* were to be simulated. Since RTBC for aerospace applications is a new and niche field of research, no data for verification was found in public literature. There are, however, two validation cases available in literature. It was therefore decided that no highly accurate verification case were simulated, but instead only validation was performed. Both of the validation cases were published by Zagarola from Creare LLC, together with other coworkers and NASA researchers. The first validation case is the only produced and operated RTBC for aerospace applications to date, i.e. the NICMOS cryocooler for the Hubble Space Telescope [98]. The second case is an optimsation study performed for NASA zero boil-off (ZBO) liquid hydrogen storage in space. It presents estimated performance using detailed validated models, and are thus considered validation data. Both cases present additional scaled designs, which are compared to the model for extra validation. The results hereof can be found in Appendix A.

The NICMOS cryocooler validation case

The first validation case is the engineering model for the NICMOS cryocooler, which has been extensively documented for load temperatures between 29 K and 49 K [98]. A scaling study has been performed on this cryocooler to increase the original cooling power of 6.3 W to 40 W, documented by Zagarola and McCormick [97]. For the validation case discussed here, the original RTBC design is used. The RTBC has a cold load of 6.3 W at 49 K, with an additional 0.7 W estimated external parasitics. The cooler required 335 W of input power, and had a 9.3% fraction of the Carnot efficiency. The 10 W output power of the turboalternator was not recovered. The cycle used neon as fluid, had a compressor ratio of 1.82 and one single stage compressor. A summary of the validation case is presented in Table 3.11.

As observed from the validation results, the model matches the engineering model of the NICMOS RTBC within 1.1%. Although this is a good result, multiple detailed performance parameters are missing in this study. Such as mass flow rate, the recuperator thermal effectiveness, and a value of the pressure in the cycle. As such, no clear conclusions can be drawn about the origin of the difference in the results. To strengthen the validation, another case is simulated with an extended list of performance parameters in the following subsection.

The NASA ZBO liquid hydrogen storage in space validation case

The second validation case is a design study and technology demonstration effort for NASA on a 20 K, 20 W crycooler for zero boil-off (ZBO) liquid hydrogen storage in space [25]. The study is composed of the results of a validated model and the technology demonstration of the turbine, compressor and recuperator. Furthermore, it presents two scaled designs of 50 W and 80 W. For the validation discussed here, the 20 K, 20 W cryocooler is used.

The crycooler consists of three single stage centrifugal compressors connected in series, with inter-compressor heat rejection build into the compressor housing. It has a single stage turbine, a recuperator consisting of 6 stages connected in series, and uses helium as working fluid. A cycle schematic is shown in Figure 3.23. The validated model in the study estimates detailed component performance. The turbomachine models take aerodynamic losses, viscous drag, seal leakage, resistive losses and electromagnetic dissipation into account. The electronic model estimates power conversion losses and overhead losses. The model for the recuperator modules accounts for stream-to-stream heat transfer losses, streamwise heat conduction, pressure drops, and parasitics originating from radiation and heat conduction through the supports. Tubing models take pressure losses between components into acount, and models for the aftercooler account for thermal inefficiencies and pressure drops in the heat exchangers.

As apparent, the validated model used in the validation case is more detailed than the model developed in this research. This provides the opportunity to validate that the conceptual model developed can predict detailed performance data based on component efficiency coefficients. To efficiently compare the conceptual model to the validation case, the compressor inverter efficiency and turboalternator

Table 3.11: 49 K, 6.3 W cryocooler performance results against model predictions

Performance parameter	Validated result	Model prediction	Difference
Crycooler performance			
Cold load temperature	49 K	49 K	-
Cold load	6.3 W[1]	6.3 W[1]	0%
Heat rejection temperature	292 K	292 K	-
Turboalternator power	10 W	10 W	0%
Turboalternator power recovered	0 W	0 W	0%
DC input power	335 W	339 W	1.1%
Fraction of carnot efficiency	9.3%	9.2%	-0.1%
Crycooler features			
Cycle gas	Neon	Neon	-
Number of stages	1	1	-
Number of compressors	1	1	-
Cycle pressure ratio	1.82	1.82	-
Component performance			
Compressor efficiency	38%	38%	0%
Turbine efficiency	60%	60%	0%
Recuperator loss parameter β	30%	30%	0%

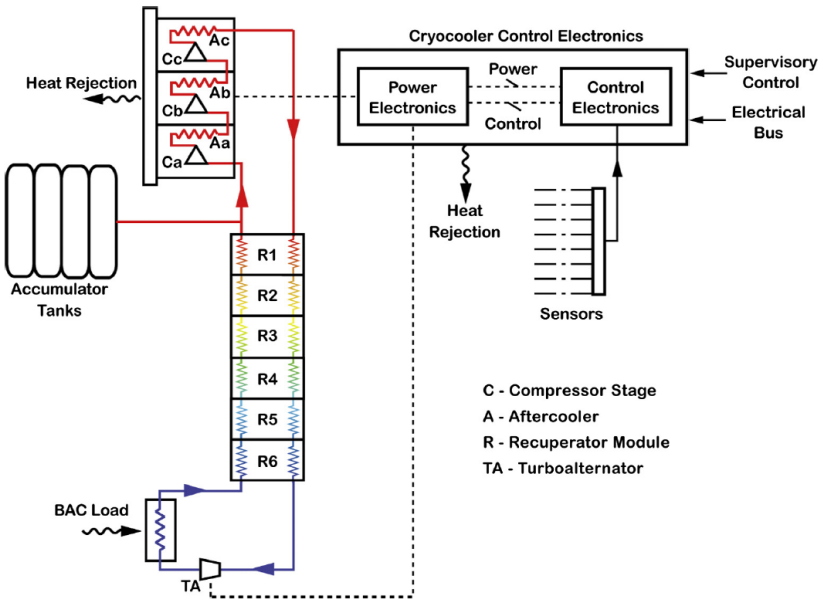

Figure 3.23: Cycle schematic of the 20 K, 20 W crycooler used for validation [25]

power recovery in percent were included in the conceptual model as well as the inverter overhead power of 10 W. A summary of the validation case data is displayed in Table 3.12.

As seen in Table 3.12, the model developed in this research matches the validation data within 3.1%. In order to match the validated data, the compressor efficiency input is slightly increased. The compressor net efficiency of 64% is an average value and no comment was made on whether those are

[1]Value does not include a 0.7 W external parasitics

polytropic, isentropic or otherwise defined values, nor was it explained if the inter-turbine heat rejection was taken into account for this efficiency value. It was therefore decided to tweak this parameter slightly to match the cycle efficiency, instead of tweaking the other input values of which no uncertainty of definition exists.

Table 3.12: 20 K, 20 W cryocooler performance results against model predictions

Performance parameter	Validated result	Model prediction	Difference
Operating conditions			
Cycle gas	Helium-4	Helium-4	-
Mass flow rate	3.2 g/s	3.1 g/s	-3.1%
Compressor pressure ratio	1.45	1.45	-
Compressor inlet pressure	4.2 atm	4.2 atm	-
Heat rejection temperature	300 K	300 K	-
Load outlet temperature	20 K	20 K	-
Electronics			
Bus DC input electrical power	1215 W	1231 W	1.3%
Compressor inverter power	1235 W	1250 W	1.2%
Turboalternator power recovery	29 W	29 W	0%
Inverter overhead power	10 W	10 W	-
Electronics heat rejection	87 W	-	-
Compressor/Aftercooler			
Compressor AC input power	1160 W	1175 W	1.3%
Compressor & aftercooler total heat rejection	1150 W	1163 W	1.1%
Compressor net efficiency	64%[1]	66%	2%
Cold end			
Turboalternator net output power	32 W	32 W	0%
Turboalternator net efficiency	77%	77%	0%
Recuperator loss	12 W	12 W	0%
Recuperator loss	38%	38%	0%
Recuperator overall thermal effectiveness	0.997	0.997	0%
Net refrigeration	20 W	20 W	0%
Cryocooler COP as % of Carnot COP	23%	22.4%	-0.6%

It can be seen that the predicted mass flow rate is lower. Due to the no thermal ineffectiveness in the cold HEX of the model, the specific cooling power is increased. Hence, the required mass flow rate is lower. Additionally, the model assumes no thermal ineffectiveness in the warm HEX (aftercooler), which can be seen in the increased heat rejection predicted by the model. Moreover, it can be observed that the specific power of the turbine and compressor are increased as a result. This can be attributed to differences in assumed pressure losses throughout the system.

Despite the differences in both models, the maximum difference in data is just 3.1%. This, in combination with the previous validation case and performed verification, shows that the model developed in this research represents the conceptual description and can accurately predict the RTBC system process in the real world. The RTBC system model is therefore deemed verified and validated.

[1] Average value

3.5. Model integration of the Liquid Hydrogen Fuel Tank, the Reverse Turbo-Brayton Cryocooler system, and the Conceptual Compressor design

In this chapter, the design and modelling methodologies for the liquid hydrogen fuel tank, Reverse Turbo-Brayton Cryocooler, and conceptual compressor have been discussed. The three models are integrated to perform a concurrent simulation and design of RTBC systems.

In order to do so, first a study is done with the liquid hydrogen fuel tank model to obtain the required cooling power and cooling load temperature for the RTBC. With these inputs, the RTBC system design is performed based on assumptions on component performance. Once the RTBC system is designed, the performance of the turbomachinery is investigated by constructing a detailed conceptual design of the centrifugal compressor for the conditions defined by the RTBC system model. The performance of this conceptual compressor is assessed, and used in the RTBC instead of the constant compressor efficiency assumption. Then, the performance of the RTBC system is assessed again. With the performance of the RTBC and its conceptual compressor known, an integrated study with the liquid hydrogen fuel tank model is performed. This is done based on the exploration study on the active cooling of the liquid hydrogen fuel tank concept of the carbon neutral long range Flying-V aircraft (Section 4.1). With the obtained results, new insights can be gained to widen the understanding and feasibility of carbon neutral aeronautical applications.

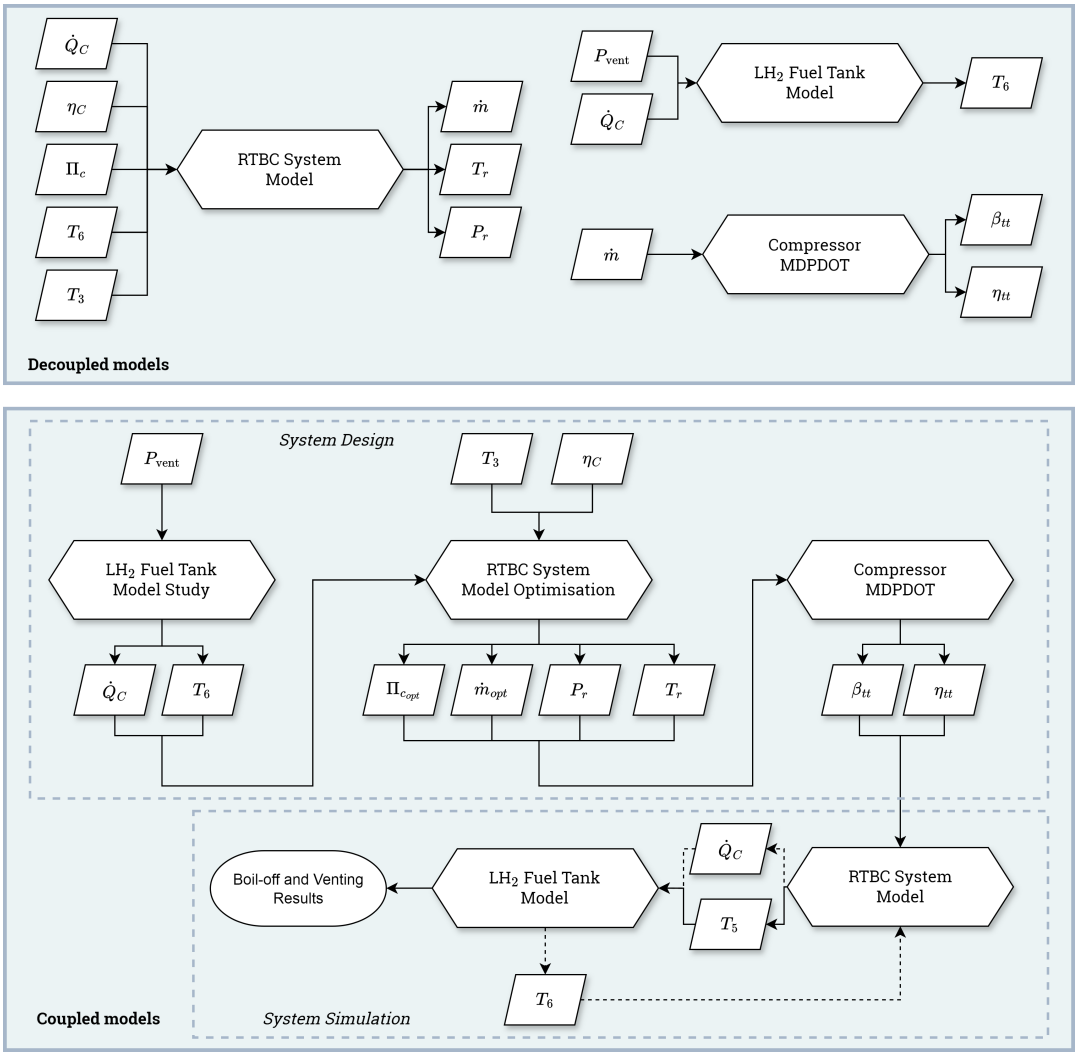

Figure 3.24: Executive flowchart of decoupled and coupled modelling and simulation method. The dotted arrows are envisioned steps for future off-design simulations

An executive flowchart of the decoupled and coupled models is shown in Figure 3.24. The executive distinction is made here, as the flowchart is a simplified representation and only includes the model variables needed to make executive decisions about the model integration. In the current research,

the RTBC is simulated at the design point. The values for the cooling power ($\dot{Q}_C$) and cooling load temperature (T_6) are therefore taken from the system design. For future off-design studies, however, the cooling power and cooling load temperature need to be integrated differently. The envisioned extra steps to do so, are denoted with the dotted arrows in Figure 3.24.

The RTBC system model and conceptual compressor model are constructed in python (Sections 3.3.1 and 3.3.2). Despite the liquid hydrogen fuel tank being constructed in Dymola, the model can be accessed and run directly via python (Section 3.2.6). As all three models can be accessed and run from the same coding environment, it is possible to integrate the three models into one integrated model. Doing so, it provides the possibility for performing multidisciplinary design analysis and optimisation (MDO). This is recommended for further studies, as it will enable to assess the impact of active cooling to disciplines outside of the fuel tank system.

4

Results

This chapter documents the results of the modelling and design efforts obtained with the methodology described in Chapter 3. First, the definition of the exploration study is provided in Section 4.1. This definition of the exploration study provides the inputs needed for the models and design efforts, and provides a clear foundation from which the final conclusions can be build. In Section 4.2, the RTBC design and results of its modelling is discussed. Hereafter, Section 4.3 deepens into the conceptual design of the compressor and its performance at the design conditions. Lastly, Section 4.4 integrates the results from the previous sections into the exploration study on the integrated performance of the RTBC, including detailed conceptual compressor design, on the cooling of the liquid hydrogen fuel tank.

4.1. Definition of the exploration study

A detailed physical representation of the liquid hydrogen fuel tank, and the Reverse Turbo-Brayton Cryocooler have been described in Section 3.1. In order to explore the capabilities of the Reverse Turbo-Brayton Cryocooler for active cooling of the liquid hydrogen fuel tank of the Flying-V, the flight specifics of the exploration study need to be clearly defined. Woensel [94] has performed a study on the integration of a liquid hydrogen fuel tank in the concept of the Flying-V. Several configurations of the fuel tank integration are considered, retrofitted into the original Flying-V. Moreover, the study performs a structural iteration to account for the lower fuel weight of hydrogen. For the exploration study in this report, configuration 1 of the structural iterated Flying-V design (case 2: Iteration) is considered.

Configuration 1 has a **Maximum Take-Off Weight (MTOW) of 159 metric ton**, and an **Operational Empty Weight (OEW) of 99 metric ton**. Compared to the original FV-900 with an MTOW of 234 metric ton and an OEW of 115 metric ton, the structural improvement and use of hydrogen shows significant weight reductions. Based on the methodology presented by Woensel [94], the flight performance and mission profile of the mission with maximum passengers could be recreated. Unfortunately, for payload weights less than the maximum number of passengers, the range estimation deviates (see Figure 4.1). The flight performance analysis for maximum passengers that matches that of Woensel [94] is shown in Table 4.1, and is indicated on the payload-range diagram in Figure 4.1. As seen in the diagram, despite the reduction in structural weight, the range of the hydrogen Flying-V is less than that of its original kerosene design. This limits the feasibility of the hydrogen Flying-V concept, and emphasises the need for effective boil-off management. To put the exploration study into perspective, the flight distance is related to available flight destinations when departing from Schiphol Airport (AMS). With maximum passengers, the original kerosene Flying-V concept has a range of 10800 km. This is approximately the flight distance from AMS to Singapore (SIN), an important connection hub. The hydrogen Fling-V concept has a **maximum passenger range of 8900 km**, which is approximately the flight distance from AMS to Los Angeles (LAX). In Figure 4.18 the range for both concepts is plotted on a world map, which shows that this reduction in maximum flight distance can limit the flight operation of the aircraft.

For this exploration study, it was decided to explore the period of the mission that generates the most hydrogen boil-off. Boil-off is predominantly generated during phases of the mission spanning prolonged periods of time, with minimal fuel usage. The phase of most interest is, therefore, **the cruise phase**. All other phases of the mission are much shorter in duration, and/or subtract more fuel from the tank. Verstraete et al. [92] showed that the hold period of an aircraft can have considerable effect on boil-off and tank design as well. The hold period, caused by runway congestion or other reasons to postpone take-off, can be reduced by efficient aircraft handling. It is therefore recommended for further studies

that an integration study with aircraft logistics is performed to investigate the effect of hold period on boil-off behaviour. Additionally, it is recommended to use the liquid hydrogen tank model to investigate the boil-off behaviour of all other phases of flight, to have an understanding of the required RTBC operation throughout the mission.

The general characteristics of the exploration study are summarised in Table 4.2. All characteristics follow from the mission profile, whilst the tank pressure is assumed to have reached venting pressure at the start of the cruise phase. an RTBC with a **cooling power of 800 W** is included per tank, which is the same cooling power as a reference design developed for turboelectric aircraft (see Section 3.1.2). Using the weight and dimensions of the reference design, definite conclusions can be drawn about the feasibility of using RTBC to cool liquid hydrogen fuel tanks. The cooling temperature corresponds to the temperature of the liquid hydrogen in the fuel tanks at the venting pressure. Note that this is the temperature of the RTBC working fluid leaving the cooling element (T_6). One deviation is present from the study performed by Woensel [94]. That is, the tank is not assumed to be a hollow cylinder with an "effective radius" to match the volume of the structural tank. Instead, the tank is modelled as a cylindrical tank section with the same length and two end domes with an aspect ratio (see Section 3.2.5), such that it has the same volume as the original structural tank. Note that the hydrogen Flying-V concept has two liquid hydrogen fuel tanks.

Table 4.1: Flight performance analysis results for configuration 1, case 2: Iteration, plus the kerosene based FV-900 [94]

	Conf. 1	FV-900
MTOW [t]	159	234
OEW [t]	99	115
Range [km] with n_{pax}		
440 pax	8900	10800

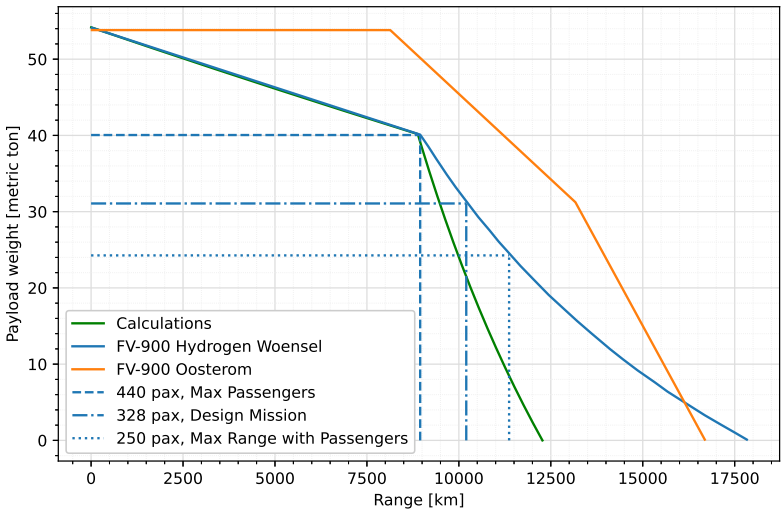

Figure 4.1: Payload-range diagram of configuration 1, case 2: Iteration, plus the kerosene based FV-900 [94]

Table 4.2: General exploration study characteristics. Note that the hydrogen Flying-V concept has two liquid hydrogen fuel tanks and two RTBC

Parameter	Value	Parameter	Value
Length of cylindrical tank	10 m	Fuel weight at start cruise	18.439 t
Insulation thickness	0.16 m	Fuel volume at start cruise	269.6 m^3
Tank internal radius	2.0 m	Fill fraction at start cruise	0.849
Venting pressure	1.75 bar	Fuel usage during cruise	0.394 kg/s
Cooling power	800 W	Cruise time	9 h 19 min
Cooling temperature	22.4 K	Cruise range	8406 km
Tank volume	158.7 m^3	Cruise altitude	13000 m
Aspect Ratio end domes	1.0	Cruise Mach number	0.85

4.2. RTBC system design

This section describes the system design and modelling results of the RTBC. The system design variables and other inputs to the model are defined in Section 4.2.1. The obtained design point for the

RTBC is then presented in Section 4.2.2. Finally, a sensitivity study on the efficiency of its components is performed in Section 4.2.3.

4.2.1. RTBC system design variables and specifications

In order to asses the performance of the RTBC, the inputs to the model need to be defined. This is done based on the outputs from the liquid hydrogen fuel tank model (Section 4.4), outputs from the conceptual compressor design (Section 4.3), and parameters from literature. The pressure ratio is varied over the range of 1 to 8, in order to find the optimal system design. A summary of the input values are shown in Table 4.3. Note that the majority of the design specifications are assumptions.

The cooling power input is taken to be 800 W, which corresponds to a NASA innovation research at TRL4 [95]. This RTBC has the purpose of cooling superconducting systems in aircraft, and its input power, efficiency, dimensions and mass are provided (see Section 3.1.2). The cold load temperature is taken from results of the liquid hydrogen tank model, and the heat rejection temperature is corresponding to the value used in the majority of public literature. A value of 300 K is used throughout literature, independent of the application [97, 47, 16, 79, 25, 99, 27, 57]. This heat rejection temperature is higher than the ambient temperature during cruise. However, current advanced aerospace recuperators under development for RTBC are all designed for warm-end inlet temperatures of 300 K and cold-end inlet temperatures around 20 K [26, 71]. As the performance metrics of these recuperators are used in this research, the heat rejection temperature is kept at 300 K. A reduction in heat rejection temperature, however, could significantly increase the cycle efficiency. It is therefore recommended to research the development of a new advanced aerospace recuperator, capable of operating with lower warm-end inlet temperatures.

The compressor efficiency is taken from the results of the conceptual compressor design, and the turbine efficiency corresponds to the efficiencies presented by Deserranno, Niblick, and Zagarola [24]. In this study a 5-stage 1 kW turboalternator is tested, of which three stages, with each a pressure ratio close to 2, have an aerodynamic efficiency of 89% or higher. A similar turbine efficiency has been reported in a study on RTBC for zero boil-off liquid hydrogen storage [25]. Although the net efficiencies are slightly lower, it is assumed that a net efficiency of 89% can be achieved due to the improvements in turbomachinery design over the past 10 years.

Table 4.3: RTBC system design variables and specifications

Description	Definition	Value	Source
Design variables			
Cooling power	$\dot{Q}_C$	800 W	[95]
Cold load temperature	T_6	22.4 K	Section 4.4
Heat rejection temperature	T_3	300 K	[97]
Compressor pressure ratio	Π_C	1-8	[97]
Design specifications			
Cycle fluid	-	Helium-4	-
Compressor efficiency	η_C	85.9%	Section 4.3
Turbine efficiency	η_T	89%	[24, 25]
Recuperator thermal effectiveness	ϵ_R	0.995	[26]
Recuperator LPS inlet pressure	P_6	5.6 atm	[26]
Recuperator pressure drop	P_{drop_R}	1.7%	[71]
Cold-end HEX pressure drop	$P_{drop_{CHEX}}$	0.005 bar	[27]
Warm-end HEX pressure drop	$P_{drop_{WHEX}}$	0.02 bar	[27]

The recuperator thermal effectiveness is taken from the performance test of a high-capacity shell-and-tube recuperator (Deserranno et al. [26]). This recuperator has a warm-end and cold-end temperature of 300 K and 20 K respectively, and a low pressure side (LPS) inlet pressure of 5.6 atm. The pressure drop over the recuperator is not mentioned, therefore the non-dimensional pressure drop is used from tests of a new-technology recuperator developed by the same company (Niblick, Cox, and

Zagarola [71]). The values for the pressure drops over the cold and warm heat exchangers are taken from a study on a high-capacity RTBC for HTS cables (Dhillon and Ghosh [27]). Although not an aerospace application, these are the only pressure drop values found for HEX in high-capacity RTBC. Finally, note that the input parameter P_1 can easily be obtained as the recuperator pressure drop and the recuperator LPS inlet pressure P_6 are known.

4.2.2. RTBC system optimisation and design point

The results of the optimisation study as described in Section 3.3.1 are displayed in Figure 4.2. In this figure, the power of the compressor, turbine and recuperator are plotted against pressure ratio. Moreover, the mass flow rate, COP and the percentage of Carnot efficiency are displayed. In each plot, the design with maximum COP is marked with a red cross. The temperature versus entropy diagram (TS-diagram) of the cycle with maximum COP is shown in Figure 4.3. As observed from the power plots, the minimum compressor input power determines the maximum COP and its corresponding pressure ratio. The turbine power and recuperator loss both follow a different trend, which is similar to the behaviour of the mass flow rate.

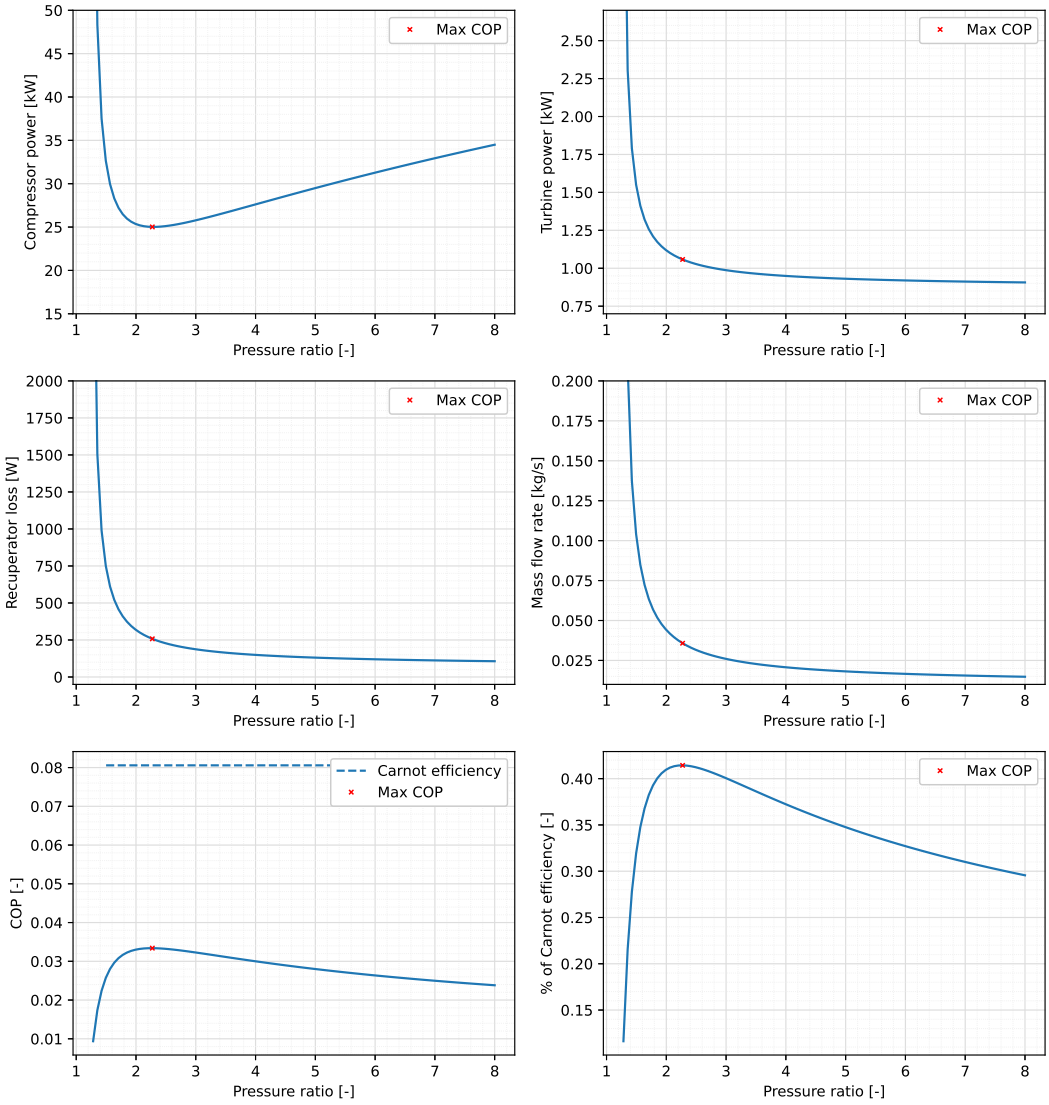

Figure 4.2: Variation of system and subsystem parameters of the RTBC design with cycle pressure ratio

The behaviour of the three subsystems can be attributed to a combination of their non-dimensional variation with the pressure ratio and the mass flow behaviour. With increasing pressure ratio, the specific power of the compressor and turbine increase (see Equations (3.45) and (3.46)). On the other hand, the specific recuperator loss does not change with pressure ratio (Equation (3.47)). When correct heat flow accounting is performed, it can be deduced that (see also Figure 4.3):

$$\dot{Q}_C = \dot{W}_T - \dot{Q}_{R_L} \tag{4.1}$$

The result is that with increasing pressure ratio, the specific cooling power increases. This causes the mass flow to decrease. For the compressor power, the decrease in mass flow initially dictates its behaviour. At a certain point, however, the increase in specific power of the compressor becomes dominant and starts to dictate its behaviour. For the turbine power, this effect is similar but much less pronounced. The specific recuperator loss does not vary with pressure ratio, and thus the recuperator loss follows the same trend as the mass flow rate. The compressor power is much bigger in size than the cooling power and the turbine power (COP $\leq$ 4%), and thus the COP and percentage of Carnot efficiency are dictated by the behaviour of the compressor. These findings are supported by findings in literature [27].

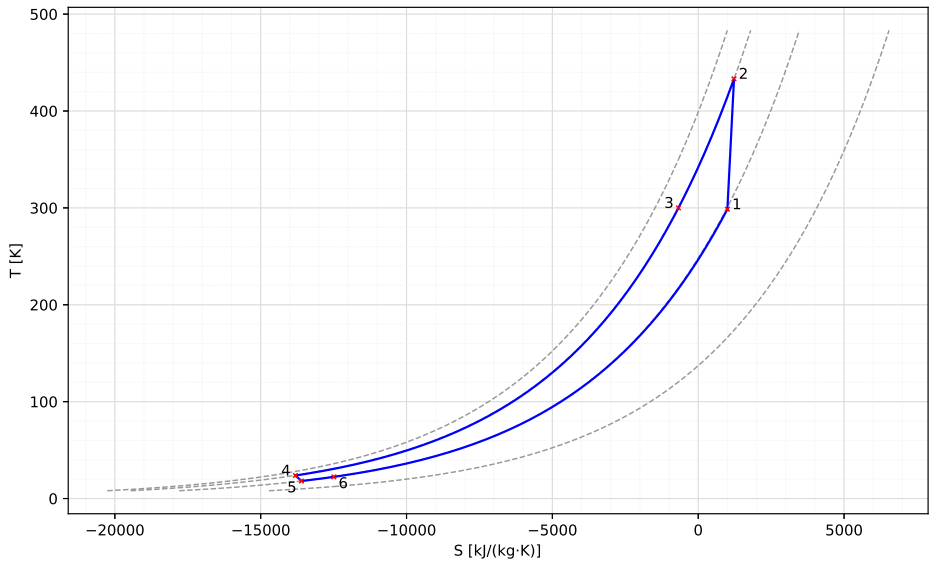

Figure 4.3: The temperature-entropy diagram (TS-diagram) of the RTBC design cycle. The numbers with corresponding red crosses indicate the stations in the cycle

The final RTBC design at maximum COP is summarised in Table 4.4. The data of one of the most efficient 20 K cryocoolers to date is added in the table, which is for a lower capacity space application [25]. As seen, the designed RTBC has an efficiency of 40.6%, which is almost a factor 2 more than the efficiency of the lower capacity RTBC. The result is an increase in cooling power of a factor 40, with just an increase in input power by a factor of 20. The increase in efficiency is mainly contributed to the increase in compressor efficiency. Although no electromagnetic dissipation is taken into account for the aeronautical RTBC design, an improvement of close to 20% is obtained. This clearly shows the superb level of scalability of the turbomachinery that characterises the RTBC. It must be noted that due to the assumptions and different application of the RTBC system model, the data is not directly comparable but can still provide valuable insights.

Note for the space RTBC in Table 4.4 that the heat rejection temperature of 300 K appears to be a high value for an RTBC operating in space. Although no information in literature is given why this space RTBC and most others have such a high rejection temperature, a simple reason is suspected. When lowering the heat rejection temperature, the compressor inlet temperature decreases accordingly. Before 2020, all research towards RTBC compressor design were using standard compressor inlet conditions at sea level (i.e. around 300 K). In 2020, a first research effort was made on compressors with lower inlet temperatures (see Section 2.1.2). The operating condition of the compressor presented a challenge for stable gas bearing operation [21]. No RTBC compressor which is capable of handling lower inlet temperatures is designed at the moment of this writing, which is the expected cause of the heat rejection temperature of 300 K. Accordingly, all research efforts towards RTBC recuperators use a warm-end inlet temperature of 300 K. In order to lower the heat rejection temperature, therefore, advancements must be made in high-speed miniature compressor and recuperator design first.

Table 4.4: Performance parameters of the designed aeronautical RTBC system, including those of a state-of-the-art space RTBC design

Performance parameter	Aeronautical RTBC Design	Space RTBC [25]
Operating conditions		
Cycle gas	Helium-4	Helium-4
Mass flow rate	35 g/s	3.2 g/s
Compressor pressure ratio	2.29	1.45
Compressor inlet pressure	5.5 atm	4.2 atm
Heat rejection temperature	300 K	300 K
Load outlet temperature	22.4 K	20 K
Electronics		
Bus DC input electrical power	24460 W	1215 W
Compressor inverter power	25515 W[1]	1235 W
Turboalternator power recovery	1055 W	29 W
Inverter overhead power	-	10 W
Compressor/Aftercooler		
Compressor stages	1	3
Compressor AC input power	25515 W	1160 W
Compressor & aftercooler heat rejection	25260 W	1150 W
Compressor aerodynamic efficiency	-	79%-82%[2]
Compressor net efficiency	85.9%[3]	62%-66%[2]
Cold end		
Turboalternator net output power	1055 W	32 W
Turboalternator aerodynamic efficiency	-	89%
Turboalternator net efficiency	89%[3]	77%
Recuperator loss	255 W	12 W
Recuperator loss	24.2%	38%
Recuperator overall thermal effectiveness	0.995	0.997
Net refrigeration	800 W	20 W
Cryocooler COP as % of Carnot COP	40.6%	23%
Crycooler mass and size		
Cryocooler mass	-	88 kg
Turbine diameter	-	10 mm
Compressor diameter	23 mm	19 mm
Recuperator UA	2836[4] W/K	6191 W/K

[1] No motor loss taken into account, but ultra high-speed reluctance machines for >1m rpm have efficiencies up to 98% [41]
[2] Depending on the stage
[3] Electromagnetic dissipation not taken into account
[4] Average value over the five modules [26]

4.2.3. Design specification sensitivity study: the turbine, recuperator and compressor efficiencies

The design variables of the RTBC are determined by its application, and can therefore differ based on the required design. The design specifications, however, are results from models and assumptions of subsystems. In order to quantify the effect they have on the performance of the RTBC, a sensitivity study is performed.

In this sensitivity study, the three subsystem efficiencies and effectiveness are considered. For each of the considered subsystems in Figures 4.4 to 4.6, the original RTBC design is displayed with a solid line. The compressor and turbine efficiencies are then changed from 75% to 100% in steps of 5%. The recuperator thermal effectiveness is changed from 0.98 to 0.99 in steps of 0.005, whilst from 0.99 to 1.00 the step is shortened to 0.0025. This is done as the range of most interest is for $\epsilon_R \geq 0.99$, since the most advanced recuperators fall in this range. For novel recuperators under development, however, the effectiveness might drop to as low as $\epsilon_R = 0.98$.

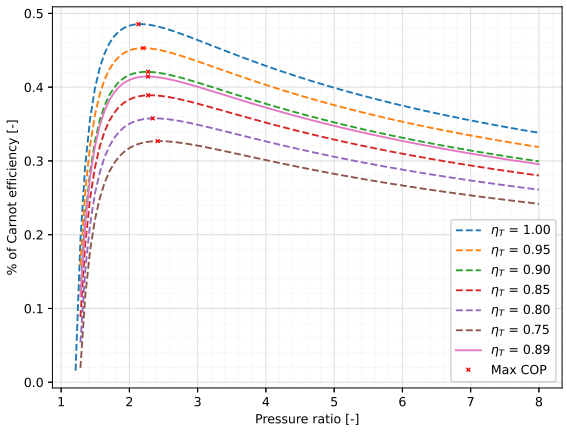

Figure 4.4: Variation of COP as a percentage of the Carnot efficiency with cycle pressure ratio, for different turbine efficiencies

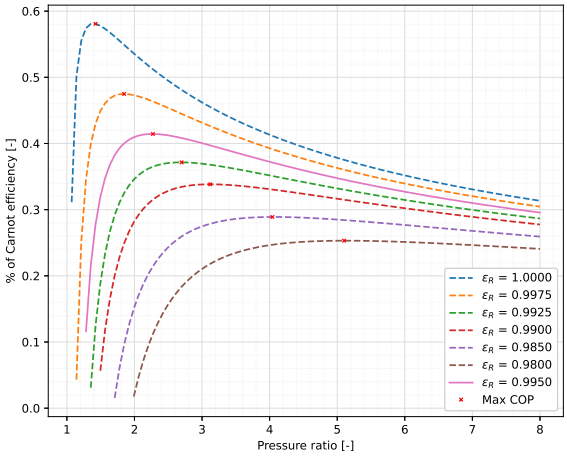

Figure 4.5: Variation of COP as a percentage of the Carnot efficiency with cycle pressure ratio, for different recuperator thermal effectiveness

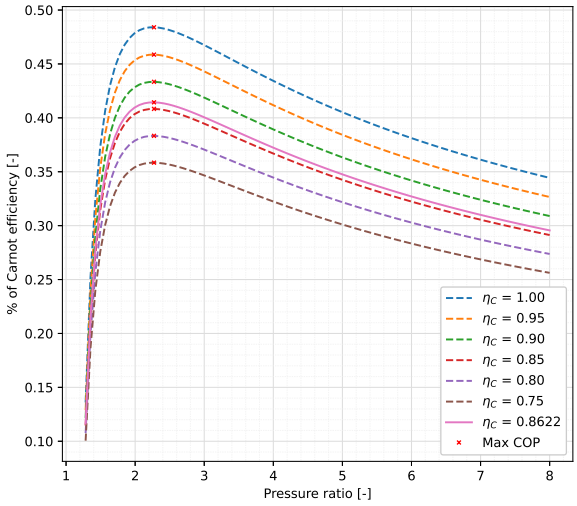

Figure 4.6: Variation of COP as a percentage of the Carnot efficiency with cycle pressure ratio, for different compressor efficiencies

In Figures 4.4 to 4.6, it can be clearly observed that the variations in compressor efficiency have no effect on the optimum pressure ratio. The turbine efficiency shows a light shift to lower pressure ratios with higher efficiency, whilst the recuperator thermal effectiveness has a major impact on the optimum pressure ratio of the cycle. This shift towards lower optimum pressure ratio's for higher recuperator thermal effectiveness is not favourable. As previously discussed, and shown in Figure 4.2, a lower

pressure ratio leads towards a higher mass flow rate. Since the mass flow rate acts as the main scaling factor for the design, the mass and size of each component will increase with increasing mass flow rate. This is especially true for the recuperator, which is the heaviest and largest component [71]. Additionally, with increasing mass flow the thermal effectiveness of the recuperator decreases [26, 71]. An increase in recuperator thermal effectiveness thus increases the mass flow rate for optimum system performance, which increases its weight, and decreases its thermal effectiveness. This makes the recuperator design an iterative optimisation problem, which needs to be thoroughly investigated.

Regarding the turbomachinery, the COP as a percentage of Carnot efficiency shows a 12% improvement when the compressor efficiency increases from 75% to 100%. Similarly, the study shows a 16% improvement in COP as a percentage of Carnot efficiency when the turbine efficiency increases from 75% to 100%. For both components the change in COP is almost linear with change in efficiency. It show that an increase in turbine efficiency is more effective for an increase in COP. The slight shift to lower pressure ratios, and thus higher mass flow rates, must be taken into account when deciding whether the main focus of turbomachinery improvement must be the turbine or the compressor.

The recuperator has a large deviation in COP as a percentage of Carnot efficiency with change in thermal effectiveness. Moreover, the change in COP is not linear, but the rate of change in COP increases with increasing thermal effectiveness. Comparing the current recuperator ($\epsilon_R = 0.995$) to the thermal effectiveness of an advanced low-capacity recuperator ($\epsilon_R = 0.997$ [25]), it can be seen that the system efficiency increases with 6-7%. Comparing it to a novel high-capacity recuperator ($\epsilon_R = 0.99$ [71]), the system efficiency drops with 6-7%. When a low thermal effectiveness of $\epsilon_R = 0.98$ is assumed, the cycle efficiency can drop to as low as 25% of the Carnot efficiency.

The sensitivity study shows that accurate estimates of the turbomachinery efficiency and recuperator thermal effectiveness are necessary to design the RTBC. Moreover, where Figure 4.2 showed that the compressor power dictates the behaviour of COP, the sensitivity study shows the biggest system performance variations with changes in recuperator effectiveness. The behaviour of all three subsystems, the mass flow rate and COP for each of the three sensitivity studies can be found in the result database for further reference (Appendix A).

4.3. Compressor design

The design of the compressor with the Multi-Dimensional Parametric Design Optimisation Tool (MDPDOT) has been divided into four steps. The first three steps perform the parametric optimisation study of the compressor and is described in Section 4.3.1. The fourth step selects the optimal compressor design based on total-to-total efficiency and computes its on- and off-design performance. This is described in Section 4.3.2. Finally, a sensitivity study is performed based on the manufacturing constraints, i.e. blade thicknesses and clearances. This essential study for such miniature turbomachines is described in Section 4.3.3.

4.3.1. Multi-Dimensional Parametric Design Optimisation

The conceptual compressor design in this report is based on 10 design variables. Of these 10 variables, the mass flow and pressure ratio are set by the RTBC design. The mass flow effectively serves as a scaling parameter. The Multi-Dimensional Parametric Design Optimisation splits the remaining design variables into three domains: overall stage design, impeller design, and diffuser design. The three corresponding parametric design optimisation studies are described below. The starting design vector and used variable range is shown in Table 4.5. This starting vector was determined based on the design method presented by the lecture series AE4206 Turbomachinery (Pini [76]). Note that for some variables the range varies with the typical values in literature (Table 3.7). This alteration was done based on intermediate results, with the objective to minimise computational time whilst allowing for designs to be close to the edge of feasibility.

Overall Stage Design

The three design variables determining the main performance of a centrifugal compressor stage are the swallowing capacity, isentropic loading coefficient, and total-to-total pressure ratio ($\Phi_{t1}, \psi_{is}, \beta_{tt}$). These three variables are predominantly used in literature to characterise compressor design. They relate, for example, pressure ratio, specific work, mass flow, power density, rotational speed and impeller tip speed Mach number to each other.

The parametric study on overall stage design uses 10 samples per variable in the range presented in Table 4.5, resulting in a design space of 1000 unique compressor designs. A three-dimensional representation of the results is presented in Figure 4.7 and shows the effect of the overall stage design variables on total-to-total efficiency. Missing data points represent infeasible designs. It can be seen in

Table 4.5: Compressor design variable range and starting values

Description	Definition	Range	Starting value
Swallowing capacity	$\Phi_{t1} = \frac{\dot{m}}{\rho_{t1} U_2 D_2^2}$	0.02-0.2	0.08
Isentropic loading coefficient	$\psi_{is} = \frac{\Delta h_{tt,is}}{U_2^2}$	0.25-1.0	0.75
Total-to-total pressure ratio	β_{tt}	1.2-6.0	2.29
Mass flow rate	$\dot{m}$	-	0.035 kg/s
Impeller shape factor	$k = 1 - \left(\frac{R_{1,h}}{R_{1,s}}\right)^2$	0.65-0.95	0.9
Impeller outlet absolute flow angle	α_2	60°-75°	65°
Number of blades	N_{bl}	10-20	14
Diffuser radius ratio	R_3/R_2	1.2-2.0	1.5
Diffuser blade height ratio	$H_{r,pinch} = \frac{H_3 - H_2}{H_2(R_2/R_{pinch} - 1)}$	0.0-1.0	1.0
Diffuser pinch radius ratio	$R_{r,pinch} = \frac{R_{pinch} - R_2}{R_3 - R_2}$	0.0-1.0	1.0

the figure that there is a trend towards low pressure ratio, low loading coefficient designs. Low pressure ratio designs generally have a high turbomachine efficiency, which corresponds to the results. Lower loading coefficients result in lower aerodynamic blade loading, and thus less losses in the impeller and a higher stage efficiency. Care must be taken whilst lowering the loading coefficient. A combination with a high pressure ratio can result in unacceptable impeller tip speed Mach numbers, which is seen by the number of infeasible designs missing from the plot (see Equation (3.59)).

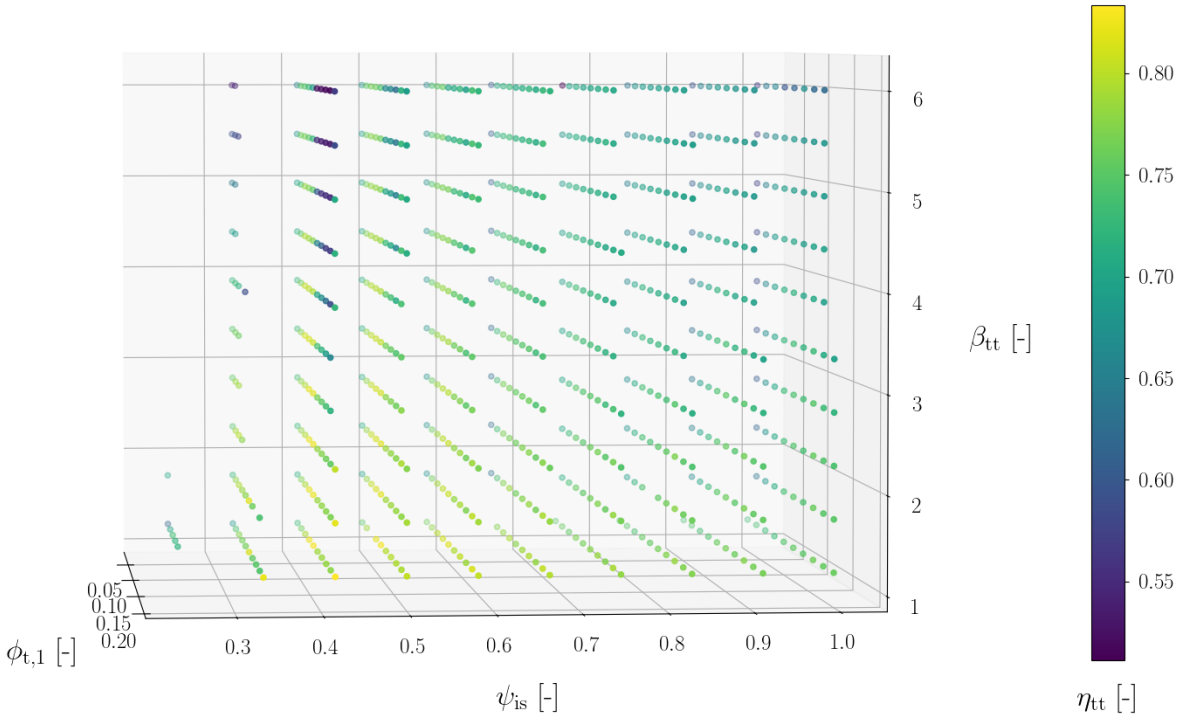

Figure 4.7: Visualisation of the influence of the overall stage design variables on stage efficiency using the MDPDOT for $\dot{m} = 0.035$ kg/s, $k = 0.9$, $\alpha_2 = 65°$, $N_{bl} = 14$, $R_3/R_2 = 1.5$, $H_{r,pinch} = 1.0$, and $R_{r,pinch} = 1.0$

The pressure ratio of the compressor is determined by the RTBC design. The variation of Φ_{t1} and ψ_{is} at the design pressure ratio of $\beta_{tt} = 2.288$ is shown in Figure 4.8. In this plot, a more noticeable behaviour of Φ_{t1} can be observed. For a constant work coefficient at constant pressure ratio and mass flow rate, increasing the swallowing coefficient decreases the impeller outlet diameter, increasing the rotational speed (see Equations (3.60) and (3.61)) [38]. As for low loading coefficients and low pressure ratios the impeller tip speed Mach number is already close to its threshold, increasing the swallowing coefficients pushes the design over that threshold towards an infeasible design. A high swallowing

coefficient is however desired, as it leads to a more compact stage. This lowers material and machining cost, weight, and axial thrust [38].

The three overall stage design variables must be chosen with care. For highest efficiency, a low pressure ratio and low loading coefficient must be chosen. For high power density, a high swallowing coefficient must be selected. Additionally, requirements from the system determines a pressure ratio which does not correspond with the pressure ratio for highest compressor efficiency. A trade-off between the variables must be made, whilst ensuring that the impeller tip speed Mach number stays below its maximum threshold.

The overall stage design with highest total-to-total efficiency has a pressure ratio of $\beta_{tt} = 2.288$, an isentropic loading coefficient of $\psi_{is} = 0.333$ and a swallowing capacity of $\Phi_{t1} = 0.06$. As RTBC already features extremely power-dense and miniature turbomachines, a low swallowing capacity is accepted. This design point in overall stage design is used for the remainder of the Multi-Dimensional Parametric Design Optimisation.

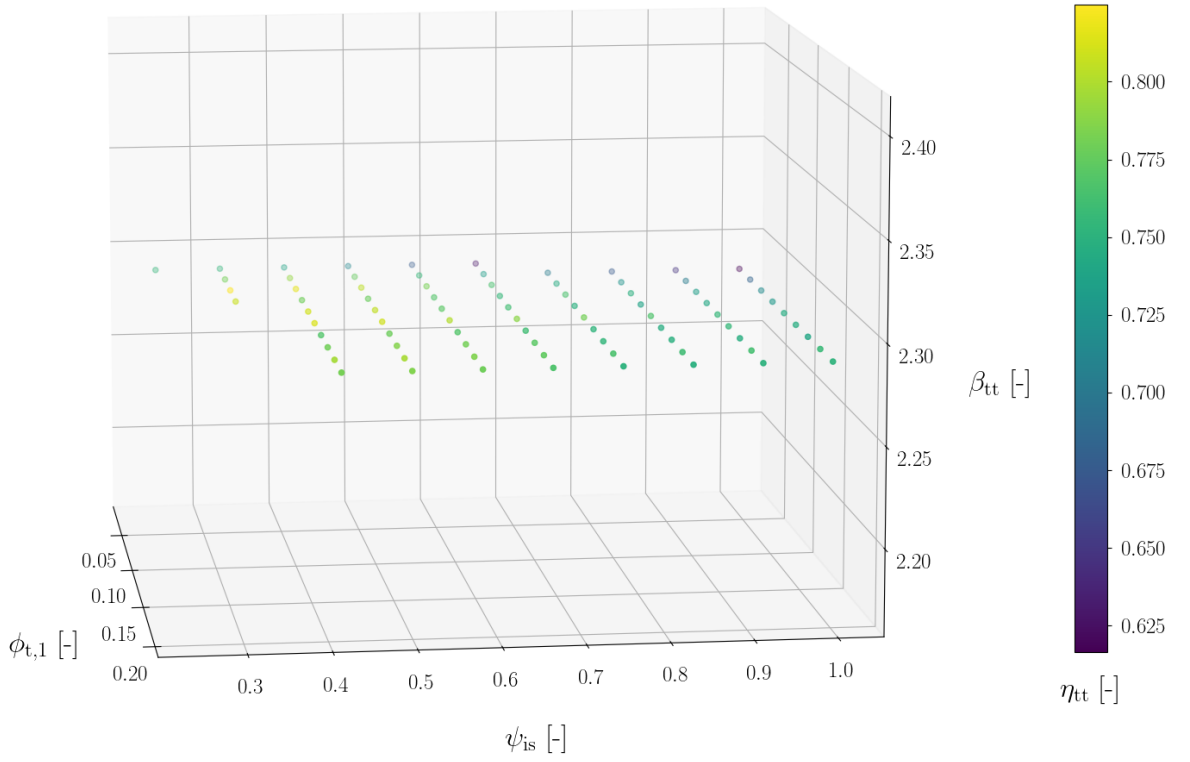

Figure 4.8: Visualisation of the influence of the overall stage design variables on stage efficiency using the MDPDOT, for $\beta_{tt} = 2.288$, $\dot{m} = 0.035$ kg/s, $k = 0.9$, $\alpha_2 = 65°$, $N_{bl} = 14$, $R_3/R_2 = 1.5$, $H_{r,pinch} = 1.0$, and $R_{r,pinch} = 1.0$

Impeller Design

Three design variables complement the overall stage design, and together determine the impeller design. These variables are the impeller shape factor, absolute flow angle at the impeller outlet, and number of blades (k, α_2, N_{bl}). The impeller outlet absolute flow angle determines the shape of the velocity triangles in the impeller, in combination with the chosen swallowing and isentropic loading coefficient. Moreover, α_2 is directly related to diffuser stability. The impeller shape factor relates the impeller inlet hub and shroud radii, and the number of blades has a direct influence on the impeller slip factor.

The parametric study on impeller design uses 11 samples per variable in the range presented in Table 4.5, resulting in a design space of 1331 unique compressor designs. A three-dimensional representation of the results is presented in Figure 4.9 and shows the effect of the impeller design variables on total-to-total efficiency. Missing data points represent infeasible designs. From the figure, a clear overall trend can be observed. For highest total-to-total efficiency, the stage should move towards high shape factors, high absolute impeller outlet angles, and a low number of blades. Infeasible designs exist for a combination of shape factors and number of blades, for $\alpha_2 \geq 65°$. For some of these designs, rotating stall occurs at the design point and are thus regarded as infeasible.

The trend towards a lower number of blades for increased efficiency might be counter intuitive, since a lower blade count generally increases slip. This decreases the slip factor, which in turn reduces the effective isentropic loading coefficient. Since the diameter and rotational speed stay the same, the increase in slip due to a lower blade count effectively decreases the impeller work. A reduction in impeller work, however, does not necessarily mean higher losses, which is clearly observed from this study. This is due to slip being an inviscid effect, having no influence on the flow dissipation. It can be observed in Figure 4.9 that a lower number of blades, resulting in a lower loading coefficient increases the stage efficiency. This is in line with the observations in Figure 4.7, which shows that lower loading coefficients increase the stage efficiency.

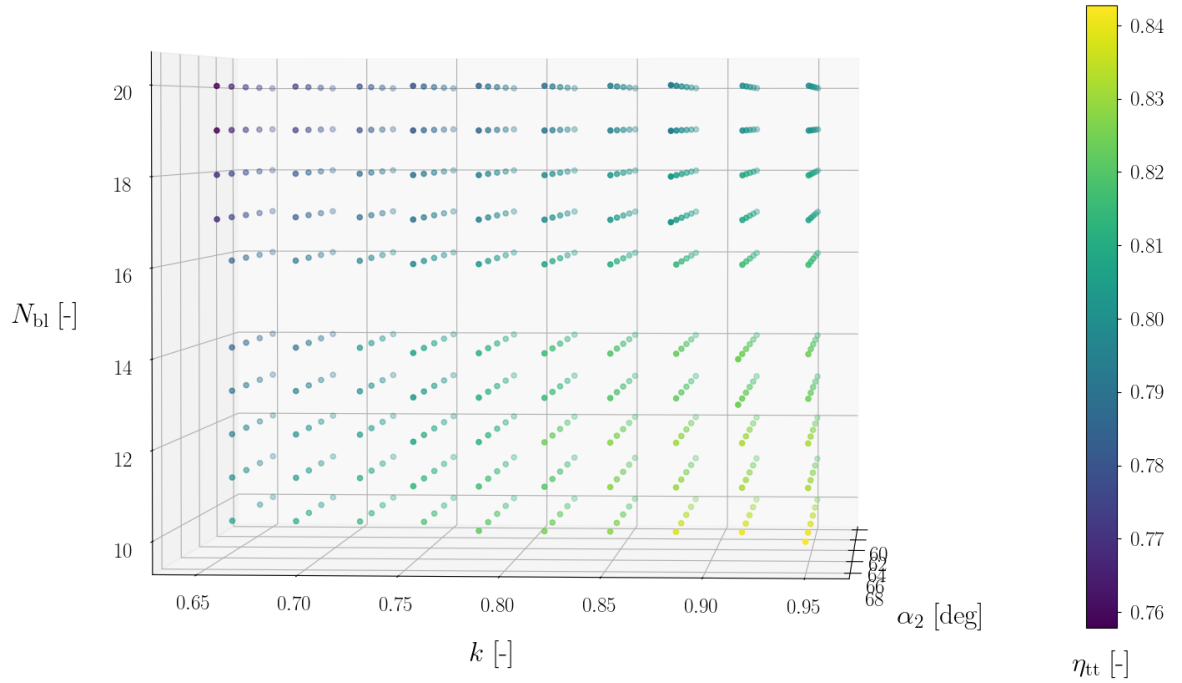

Figure 4.9: Visualisation of the influence of the impeller design variables on stage efficiency using the MDPDOT for $\dot{m} = 0.035$ kg/s, $\Phi_{t1} = 0.06$, $\psi_{is} = 0.333$, $\beta_{tt} = 2.288$, $R_3/R_2 = 1.5$, $H_{r,pinch} = 1.0$, and $R_{r,pinch} = 1.0$

High values of α_2 are seen in Figure 4.9 to obtain higher efficiencies. This can be explained by the scale of the miniature turbomachine (see Figure 2.2). The minimum tip clearance is set by manufacturing constraints, which is a high relative clearance for miniature turbomachines. This results in a considerable efficiency drop. In order to minimise this drop, the meridional velocity component at the impeller outlet can be decreased. This results in higher backsweep angles, increasing the outlet blade span, which in turn reduces the effective relative tip clearance at the impeller outlet. An increase in α_2 ensures such a reduction of the meridional velocity component, and thus increase in effective relative tip clearance. This behaviour has also been observed for miniature twin-stage compressors for aircraft ECS (Giuffré, Colonna, and Pini [37]).

High impeller shape factors indicate a large ratio of shroud to hub radius at the impeller inlet. Moreover, the impeller inlet shroud radius scales with $1/\sqrt{k}$ and the impeller inlet hub radius with $\sqrt{1-k}$. A high impeller shape factor therefore lowers the inlet radii, whilst increasing their relative distance. This decreases the wetted area relative to the flow volume, decreasing frictional losses. Studying the loss breakdown at different impeller shape factors confirms this statement. The increased impeller shape factor also has a direct effect on the radial distribution of the inlet blade angle. For a higher impeller shape factor, a larger difference in the inlet radial blade angle distribution exists. This might result in manufacturing difficulties for the extremely miniature high-speed turbomachines considered, and needs to be investigated in future studies.

The impeller design with highest total-to-total efficiency has a impeller shape factor of $k = 0.92$, an absolute impeller outlet flow angle of $\alpha_2 = 67°$, and a blade number of $N_{bl} = 10$. Since the impeller outlet flow angle is an important design variable relating the diffuser stability, this intermediate design point was computed using the reduced-order compressor model to check for convergence. It was found that the solver was unstable and resulted in an infeasible design with rotating stall at the design mass flow rate. A reduction in the outlet flow angle of $1°$ was applied, resulting in an absolute impeller

outlet flow angle of $\alpha_2 = 66°$. This design point in impeller design is used for the remainder of the Multi-Dimensional Parametric Design Optimisation.

Diffuser Design

Now that the overall stage and impeller design has been set, the final part of the stage can be designed. Altough vaneless diffusers are a simple concept, they effectively utilise the generated kinetic head in the impeller. In fact, efficiently designed diffusers can generate nearly half of the enthalpy (and thus pressure) rise of a stage [76]. The three design variable determining the performance of the vaneless diffuser are the diffuser radius ratio, the diffuser blade height ratio, and the diffuser pinch radius ratio ($R_3/R_2, H_{r,pinch}, R_{r,pinch}$).

The parametric study on diffuser design uses 11 samples per variable in the range presented in Table 4.5. For a design with no pinch, i.e. $H_{r,pinch} = 0$ and/or $R_{r,pinch} = 0$, only the designs with both ratios equal to zero are displayed. This is done as a variation in a pinch variable has no effect if there is no pinch present. This results in a design space of 1111 unique compressor designs. A three-dimensional representation of the results is presented in Figure 4.10 and shows the effect of the diffuser design variables on total-to-total efficiency. Note that the absence of compressor designs is thus not due to infeasible designs.

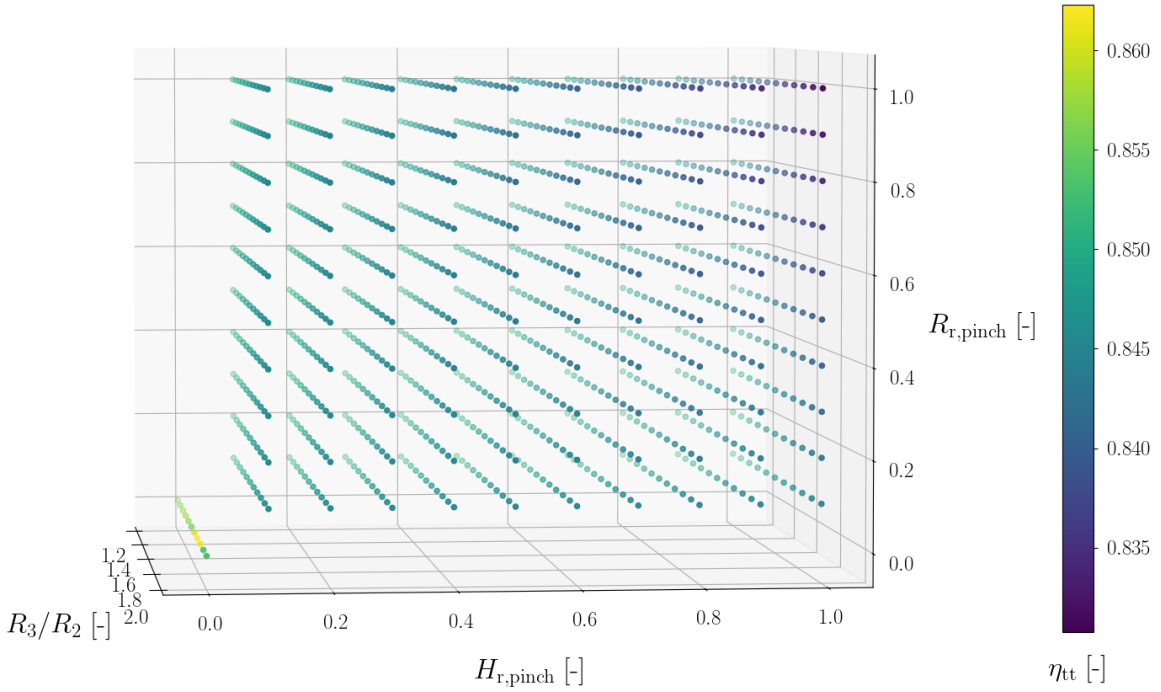

Figure 4.10: Visualisation of the influence of the diffuser design variables on stage efficiency using the MDPDOT for $\dot{m} = 0.035$ kg/s, $\Phi_{t1} = 0.06$, $\psi_{is} = 0.333$, $\beta_{tt} = 2.288$, $k = 0.92$, $\alpha_2 = 67°$, and $N_{bl} = 10$

From Figure 4.10 it is clearly observed that the design favours the absence of a pinch. This is expected, as linearly narrowing the diffuser channel increases the wetted area relative to the flow volume, and thus increases friction losses and decreases pressure recovery. The function of a pinch in the vaneless diffuser is to delay rotating stall inception [38]. Rotating stall is an extremely complex phenomena, which can only be predicted with time-accurate, three-dimensional, full annulus CFD simulations (Marconcini et al. [64]). The currently used semi-empirical correlation proposed by Kobayashi et al. [53] correctly captures rotating stall inception trends, as found by the validation performed by Giuffré, Colonna, and Pini [38]. It was noted in the validation, however, that the use of this correlation is conservative and can lead to an underestimation of the operating range. It was found to be especially the case for small-scale, high rotational speed compressors such as the compressors in RTBC. Moreover, Everitt and Spakovszky [31] found that a possible mechanism for rotating stall inception is the presence of tangential endwall flow parallel to the blade row leading edge. For axial compressors this has been associated with tip leakage flows, but in centrifugal compressors it is proposed to be generated by the high swirl present in the bulk flow in combination with a deficit of radial momentum near the shroud wall [31]. Research has to be done what the extend of this effect is in miniature, high-speed turbomachines

with relative high tip clearances. No major conclusions can therefore be drawn based on the diffuser pinch design, except that a pinch negatively influences the stage efficiency at the operating point if α_2 has been set. A careful trade-off must therefore be done with advanced CFD, to determine the optimum pinch in combination with the impeller design in order to extend operating range and increase efficiency. Note that the delay of stall inception due to the pinch might initially lower efficiency, but can result in an increased α_2 limit for diffuser stability. If in turn an increased α_2 is chosen, this can increase the stage efficiency beyond its original value.

Vaneless diffuser fundamentals suggest that a higher value of R_3/R_2 increases the pressure recovery [76]. From this, one might conclude that a higher diffuser radius ratio increases the stage efficiency. This behaviour can be noted for the no-pinch design in Figure 4.10, up to a diffuser length where the viscous losses outweigh the pressure recovery. For pinched designs, however, higher efficiencies are obtained with lower diffuser radius ratios. This is most dominant for designs with high diffuser blade height ratios, in combination with high diffuser pinch radius ratios. Moreover, for pinched designs a pinch radius closer to the diffuser inlet is favoured. Again, the primary function of a pinch in the vaneless diffuser is to delay rotating stall inception, and not to necessarily decrease other losses. The observed trends for the diffuser pinch should therefore only be considered when no rotating stall is present.

The overall diffuser design with highest total-to-total efficiency has a diffuser radius ratio of $R_3/R_2 = 1.76$, a diffuser blade height ratio of $H_{r,pinch} = 0.0$, and a diffuser pinch radius ratio $R_{r,pinch} = 0.0$. Again, the pinch of the diffuser might need to be redesigned when advanced CFD is done to characterise compressor stall inception. For this research, designing the diffuser to delay rotating stall is not the primary objective. The aforementioned design point in diffuser design, without a pinch, is therefore used for the input to the compressor on- and off-design.

4.3.2. Compressor on-design performance

The design vector of the compressor stage, resulting from the Multi-Dimensional Parametric Design Optimisation, is displayed in Table 4.6. This vector of optimal design variables is used as input to the reduced-order model to compute the on- and off-design performance of the stage. This vector is a target for the model, but the final results differ due to account for slip and other losses. In order to match the target mass flow and total-to-total pressure ratio, the RPM is manually changed and the performance at this RPM is computed. This RPM was determined to be 99.11% of the original RPM, resulting in a design rotational speed of 1,114,145 rotations per minute or 18,569 rotations per second. The main performance, design and geometry values at the design point are summarised in Table 4.7. The loss breakdown is showed in Table 4.8, the inlet and outlet velocity triangles are displayed in Figures 4.11 and 4.12, and the meridional flow path of the compressor stage is shown in Figure 4.13.

Table 4.6: Compressor design input vector for on- and off-design performance

Description	Definition	Value
Swallowing capacity	$\Phi_{t1} = \frac{\dot{m}}{\rho_{t1} U_2 D_2^2}$	0.06
Isentropic loading coefficient	$\psi_{is} = \frac{\Delta h_{tt,is}}{U_2^2}$	0.333
Total-to-total pressure ratio	β_{tt}	2.29
Mass flow rate	$\dot{m}$	0.035 kg/s
Impeller shape factor	$k = 1 - \left(\frac{R_{1,h}}{R_{1,s}}\right)^2$	0.92
Impeller outlet absolute flow angle	α_2	66°
Number of blades	N_{bl}	10
Diffuser radius ratio	R_3/R_2	1.76
Diffuser blade height ratio	$H_{r,pinch} = \frac{H_3 - H_2}{H_2(R_2/R_{pinch} - 1)}$	0.0
Diffuser pinch radius ratio	$R_{r,pinch} = \frac{R_{pinch} - R_2}{R_3 - R_2}$	0.0

Three main conclusions can be drawn. First, friction is indisputably the largest source of loss for the miniature compressor. This is expected, due to the high ratio of wetted area experienced by a flow through a miniature turbomachine. Second, the outlet blade angle is high, decreasing the meridional velocity component in an effort to increase blade span. This effort in increasing the blade span aims to decrease tip clearance losses (see Section 4.3.1). This might pose problems for structural design in

Table 4.7: On-design performance of the compressor stage

Description	Definition	Value
Performance characteristics		
Total-to-total efficiency	η_{tt}	85.9%
Rotations per minute	RPM	1,114,145 @ 99.1% RPM
Impeller tip speed Mach number	M_{U_2}	1.32
Maximum power	P_{max}	25,515 W
Maximum centrifugal stress	σ_{max}	749.3 MPa
Design variables		
Swallowing capacity	$\Phi_{t1} = \frac{\dot{m}}{\rho_{t1} U_2 D_2^2}$	0.054
Isentropic loading coefficient	$\psi_{is} = \frac{\Delta h_{tt,is}}{U_2^2}$	0.399
Total-to-total pressure ratio	β_{tt}	2.29
Mass flow rate	$\dot{m}$	0.035 kg/s
Impeller shape factor	$k = 1 - \left(\frac{R_{1,h}}{R_{1,s}}\right)^2$	0.92
Impeller outlet absolute flow angle	α_2	71.4°
Number of blades	N_{bl}	10
Diffuser radius ratio	R_3/R_2	1.76
Diffuser blade height ratio	$H_{r,pinch} = \frac{H_3 - H_2}{H_2(R_2/R_{pinch} - 1)}$	0.0
Diffuser pinch radius ratio	$R_{r,pinch} = \frac{R_{pinch} - R_2}{R_3 - R_2}$	0.0
Geometry		
Station radii	$(R_{1,h}, R_{1,s}, R_2, R_3, R_4)$	(1.8, 6.2, 11.5, 20.2, 32.1) mm
Station heights	(H_1, H_2, H_3)	(4.5, 2.2, 2.2) mm
Blade thickness at the hub	t_{max}	0.2 mm
Blade thickness at the shroud	t_{min}	0.1 mm
Tip gap ratio at impeller outlet	H_2/R_2	0.023
Axial length ratio	L_{ax}/R_2	0.7

Table 4.8: Loss breakdown at the design point

Description	Definition	Value	Description	Definition	Value
Incidence loss	$\Delta\eta_{incidence}$	0.06%	Diffuser loss	$\Delta\eta_{diffuser}$	1.13%
Shock wave loss	$\Delta\eta_{shockwave}$	0.00%	Volute loss	$\Delta\eta_{volute}$	0.59%
Loading loss	$\Delta\eta_{loading}$	0.11%	Exit cone loss	$\Delta\eta_{exitcone}$	0.17%
Friction loss	$\Delta\eta_{friction}$	8.42%	Disk friction loss	$\Delta\eta_{diskfriction}$	1.65%
Clearance loss	$\Delta\eta_{clearance}$	0.57%	Recirculation loss	$\Delta\eta_{recirculation}$	0.12%
Mixing loss	$\Delta\eta_{mixing}$	0.35%	Seal leakage loss	$\Delta\eta_{leakage}$	1.29%

combination with the low blade thickness. The third conclusion that can be drawn, is that the rotational velocity of the turbomachine is extremely high, exceeding the current RTBC RPM in literature. It was found with the MDPDOT that the design tends to favour increased RPM, which needs to be taken into consideration when using the MDPDOT. Although the estimation of the resulting maximum centrifugal stress is below the yield strength for titanium alloys such as Ti-6Al-4V, careful structural analysis needs

to be performed to ensure feasibility of the structural design. All three observations are related to structural design and performance, and hence further research in the structural domain is recommended. The results of the off-design are not discussed here, but the interested reader can inspect these results in the result database. This can be accessed in Appendix A.

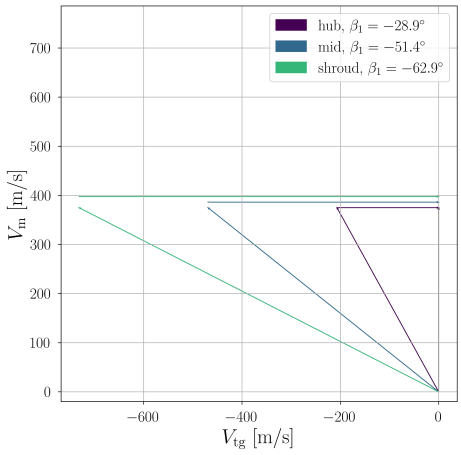

Figure 4.11: Velocity triangles at the impeller inlet, at the hub, midspan, and shroud

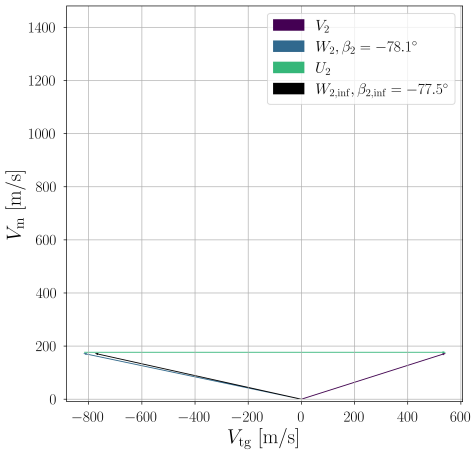

Figure 4.12: Velocity triangle at the impeller outlet

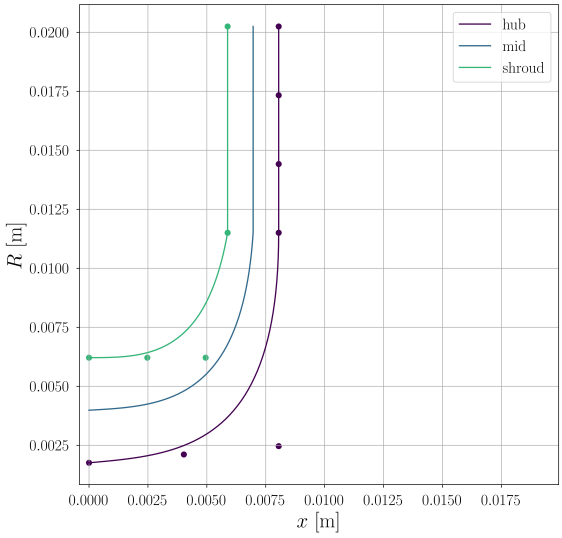

Figure 4.13: Meridional flow path of the compressor stage

4.3.3. Sensitivity study on manufacturing constraints

Few of the geometrical parameters are intentionally taken as dimensional. This is done, as for miniature turbomachinery not every geometrical feature can be scaled due to manufacturing constraints. In Section 3.3.2, it was described that the dimensional parameters in Table 3.8 are a third of the original values used in the in-house reduced-order compressor model. In order to quantify the effect this has on the compressor design, the dimensional parameters are reset to their original value and the design point is recomputed. Additionally, the effect of surface roughness will be studied by recomputing the design point with a surface roughness of an order of magnitude smaller.

Clearance and blade thickness

To assess the impact of reducing all clearances and blade thicknesses by a factor 3, the same compressor design is assessed with the original values of the in-house reduced-order compressor model. The design values, and original standard values (denoted by modified values) are displayed in Table 4.9.

Unfortunately, at the design point with the standard geometrical values the stage experiences rotating stall. Rotating stall inception is estimated when the absolute flow angle at the impeller outlet (α_2) exceeds the critical outflow angle for rotating stall ($\alpha_{2,c}$). This $\alpha_{2,c}$ is computed by the model using the semi-empirical correlation of Kobayashi et al. [53] (see Section 4.3.1), and during computations the model will detect stall when $\alpha_2 > \alpha_{2,c}$. At the design point with the standard geometrical values, α_2 exceeds its critical value. This predicted inception of rotating stall is expected, as the high relative clearance for miniature turbomachines forces the absolute flow angle at the impeller outlet (α_2) to be close to the critical angle for rotating stall, in order to increase efficiency (see Section 4.3.1). In order to mitigate the rotating stall, either the pinch characteristics can be changed, the α_2 input can be lowered, or the number of blades can be increased to decrease the slip. For this study, it has been decided to decrease α_2 by one degree.

Table 4.9: Geometrical dimensional parameters related to manufacturing constraints, design values and modified values

Variable	Design value	Modified value	Variable	Design value	Modified value
$t_{bl,h}$	0.2 mm	0.6 mm	$t_{bl,s}$	0.1 mm	0.3 mm
$\epsilon_{t,1}$	0.05 mm	0.15 mm	$\epsilon_{t,2}$	0.05 mm	0.15 mm
ϵ_b	0.05 mm	0.15 mm	α_2	66°	65°

Table 4.10: Loss breakdown of the design point with the modified manufacturing constraints

Description	Definition	Value	Description	Definition	Value
Incidence loss	$\Delta\eta_{incidence}$	0.06%	Diffuser loss	$\Delta\eta_{diffuser}$	2.90%
Shock wave loss	$\Delta\eta_{shockwave}$	0.00%	Volute loss	$\Delta\eta_{volute}$	0.63%
Loading loss	$\Delta\eta_{loading}$	0.22%	Exit cone loss	$\Delta\eta_{exitcone}$	0.17%
Friction loss	$\Delta\eta_{friction}$	7.50%	Disk friction loss	$\Delta\eta_{diskfriction}$	1.77%
Clearance loss	$\Delta\eta_{clearance}$	1.74%	Recirculation loss	$\Delta\eta_{recirculation}$	0.28%
Mixing loss	$\Delta\eta_{mixing}$	0.52%	Seal leakage loss	$\Delta\eta_{leakage}$	3.74%

The loss breakdown at the design point with the modified manufacturing constraints is shown in Table 4.10. Comparing the values with Table 4.8, it can be seen that the total efficiency of the stage drops from $\eta_{tt} = 85.92\%$ to $\eta_{tt} = 81.40\%$. This decrease is primarily caused by three of the loss sources. The clearance loss increased with a factor 3 from 0.57% to 1.74%. This increase follows from the increase in clearance at the inlet and outlet. Moreover, the seal leakage loss tripled and the diffuser loss doubled. The increase in seal leakage loss originates from the increase in back face clearance ϵ_b, increasing the channel height leading towards the seal. The diffuser loss doubling can be explained by the wake at the impeller outlet. Due to a higher tip clearance, a bigger portion of the flow enters the diffuser as a jet-flow without guidance of the blade. The unsteadiness resulting from the jet-wake at the impeller outlet persists throughout the diffuser, lowering its effectiveness [31].

All other losses do not increase significantly, however, the friction loss decreases by 1%. This decrease is attributed to the increase in tip clearance, and hence the blades having a smaller relative height, and thus smaller wetted area. Despite the increase in blade thickness, this reduces the friction loss throughout the impeller.

The drop in total efficiency shows that manufacturing constraints have a substantial effect on the stage performance. It is therefore of great importance to correctly quantify the manufacturing constraints, and its effects on efficiency. Doing so, future design efforts can be focused on the areas enabling largest performance gain. From this sensitivity study, it can be concluded that manufacturing could be a high-potential research area for increasing high-speed miniature centrifugal compressor performance.

Surface roughness

To quantify the effect the surface roughness has on the loss in the stage, a sensitivity study is done based on the standard value of the in-house reduced-order compressor model. Surface roughness values for advanced manufacturing of miniature RTBC turbomachinery is not publicly available, as mentioned in Section 3.3.2. In order to have an idea of the effect of surface roughness on the compressor, the roughness at the design point is decreased by an order of magnitude. This is corresponding

to surface roughness values of 5-axis CNC milling reported by Sadílek et al. [86]. The original and reduced value are shown in Table 4.11.

The loss breakdown of the design with the modified surface roughness is shown in Table 4.12. Comparing it with Table 4.8, it can be seen that the friction loss decreases significantly. This increases the total efficiency of the stage from $\eta_{tt} = 85.92\%$ to $\eta_{tt} = 87.42\%$. This shows, again, the substantial effect of manufacturing constraints on the stage performance. Correctly quantifying these constraints, and their effect on efficiency, is of great importance for future research. By doing so, future design efforts can be focused on the areas that enable the largest performance gain. As for the sensitivity study on clearance and blade thickness, it can be concluded from this sensitivity study that manufacturing could be a high-potential research area for increasing high-speed miniature centrifugal compressor performance.

Table 4.11: Geometrical dimensional parameters related to manufacturing constraints, design values and modified values

Variable	Design value	Modified value
Ra	3.2 µm	0.32 µm

Table 4.12: Loss breakdown at thedesign point with the modified surface roughness

Description	Definition	Value	Description	Definition	Value
Incidence loss	$\Delta\eta_{incidence}$	0.07%	Diffuser loss	$\Delta\eta_{diffuser}$	1.40%
Shock wave loss	$\Delta\eta_{shockwave}$	0.00%	Volute loss	$\Delta\eta_{volute}$	0.75%
Loading loss	$\Delta\eta_{loading}$	0.01%	Exit cone loss	$\Delta\eta_{exitcone}$	0.89%
Friction loss	$\Delta\eta_{friction}$	5.59%	Disk friction loss	$\Delta\eta_{diskfriction}$	1.86%
Clearance loss	$\Delta\eta_{clearance}$	0.58%	Recirculation loss	$\Delta\eta_{recirculation}$	0.00%
Mixing loss	$\Delta\eta_{mixing}$	0.48%	Seal leakage loss	$\Delta\eta_{leakage}$	1.30%

4.4. Integrated liquid hydrogen fuel tank modelling

The main purpose of the exploration study, is to show the potential of the use of airborne cryocoolers for cryogenic hydrogen storage. This is obtained by integrating the designed RTBC, its conceptual compressor design and liquid hydrogen tank model for the exploration study as defined in Section 4.1. The liquid hydrogen fuel tank model, constructed in Section 3.2, consists of 2076 unknown variables that can be used for result analysis. For this exploration study, however, three main results are discussed that combine the models of the RTBC, compressor, and liquid hydrogen fuel tank. First, the boil-off and vented mass during the mission are discussed for no cooling power and a cooling power of 800 W (see Sections 3.1.2 and 4.1). The second result is the study on the total tank and boil-off mass for a combination of insulation thicknesses and cooling power capacities. Finally, the third result is a study on the effect of insulation thickness and cooling power on the cruise range.

Recall from Section 3.2.3 that one hypothesis was formulated regarding the heat transfer through the liquid hydrogen fuel tank wall:

> *No transverse conduction occurs in the wall, due to the small temperature differences between the segments.*

During the exploration study, this hypothesis was verified for the results presented in Section 4.4.1. For wall segments in contact with the vapour, the transverse temperature difference throughout the insulation and tank wall did not exceed more than 2K. For the sections in contact with the liquid, the transverse temperature was even lower. For a wall segment in contact with the liquid adjacent to a wall segment in contact with the liquid, however, the temperature difference increased to up to 7 K during simulations. Although still not significantly large, this temperature difference is expected to increase for simulations where the superheated vapour temperature is much higher than the liquid temperature. It is therefore recommended for further research to include transverse conduction in the wall.

4.4.1. Effect of cooling power on boil-off and venting

To quantify the result of the exploration study, the effect of cooling power on the primary issue for long-term storage of cryogenic hydrogen is investigated, i.e. the boil-off [67]. Additionally, the vented

mass is computed to illustrate the amount of hydrogen lost during the flight. The results are shown in Table 4.13. The results of a study with identical mission characteristics, but without active cooling, are also displayed. The accompanying TS-diagram of the the two-phased liquid hydrogen mixture for both cooling power capacities during the mission duration is shown in Figure 4.14, plotted against the liquid-vapour dome of hydrogen and corresponding isobaric curves.

Table 4.13: Final system performance. Note that two tanks (and two RTBC) are present in the Flying-V

LH2 tank performance parameter	800 W RTBC cooling	No active cooling
Flight conditions		
Aircraft	Flying-V	Flying-V
Mission	AMS-LAX	AMS-LAX
Mission range	8891km	8891km
Cruise range	8406km	8406km
Cruise duration	9.31 hr	9.31 hr
Tank characteristics (per tank)		
Fuel @ start cruise	9222 kg	9222 kg
Fuel @ end cruise	2456 kg	2413 kg
Fuel consumption	0.197 kg/s	0.197 kg/s
Boil-off & venting (per tank)		
Boil-off	162.0 kg	206.4 kg
Vented mass	1.0 kg	37.6 kg

The results show that with a cooling power of 800 W per tank, the boil-off can be reduced by 44 kg per tank. Additionally, the venting is almost completely reduced to zero. Figure 4.14 shows that for both cooling power capacities, the liquid remains in a state of saturation at identical pressure. Figure 4.14 also shows that for both cooling power capacities, the vapour is superheated at identical pressure to approximately the same final temperature. This shows that an RTBC with a cooling power of 800 W has no significant effect on the thermodynamic state of the liquid and vapour during the mission duration, when compared to no active cooling.

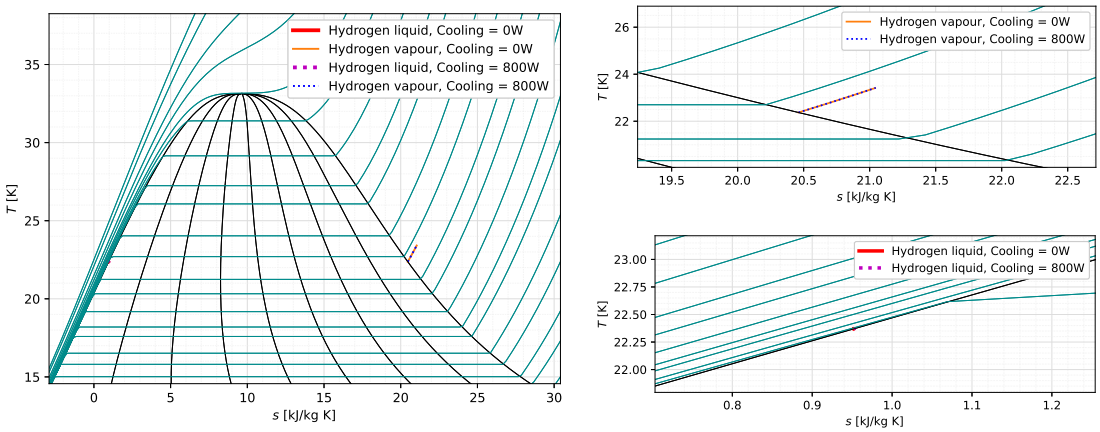

Figure 4.14: The temperature-entropy diagram (TS-diagram) of the two-phased liquid hydrogen mixture during the mission duration, plotted against the liquid-vapour dome of hydrogen and corresponding isobaric curves. Top right is zoomed in on the vapour state, bottom right is zoomed in on the liquid state

In order to achieve the reduction in boil-off and venting, the RTBC is estimated to weigh an additional 304 kg (Section 3.1.2) and require an additional power of 25.5 kW (Section 4.3.2). Based on this, there is no benefit of using an RTBC for the active cooling of the hydrogen fuel tank in the Flying-V concept

in its current state. In the next two sections, however, the use of RTBC is investigated in combination with the variation of insulation thickness to see the effect of a more integrated study.

Note that much of the input power is rejected as heat at 300 K (Table 4.4). Other usage of this heat rejection can be foreseen, in order to increase the efficiency of the system. Examples could be de-icing of aircraft wings or compressor blades, integration into the environmental control system, or turbine blade cooling.

4.4.2. Effect of insulation thickness and cooling power on total tank and boil-off mass

The liquid hydrogen fuel tank as described in Section 4.1, has an insulation thickness that ensures a maximum acceptable boil-off rate [94]. To investigate the full potential of the use of an RTBC, the effect of cooling power for various insulation thicknesses must be investigated. As a reduction in insulation thickness decreases the tank weight, the total tank and boil-off mass is used as performance parameter. This effectively describes the mass of the filled tank weight that cannot be used as fuel. The total tank and boil-off mass versus insulation thickness is plotted in Figure 4.15 for various cooling power capacities. For each power setting, the total tank and boil-off mass decreases with increasing insulation thickness up to a minimum. From this point of minimum mass, the addition of extra insulation outweighs the boil-off reduction it generates. Note that the mass of the RTBC is not taken into account in this graph. Also, the tank weights can deviate from the values reported by Woensel [94]. In the current research, only the loads on the tank wall due to the pressurised storage are considered. This results in lower wall thicknesses, and weight, than when the aircraft structural loads the wall carries are also taken into account.

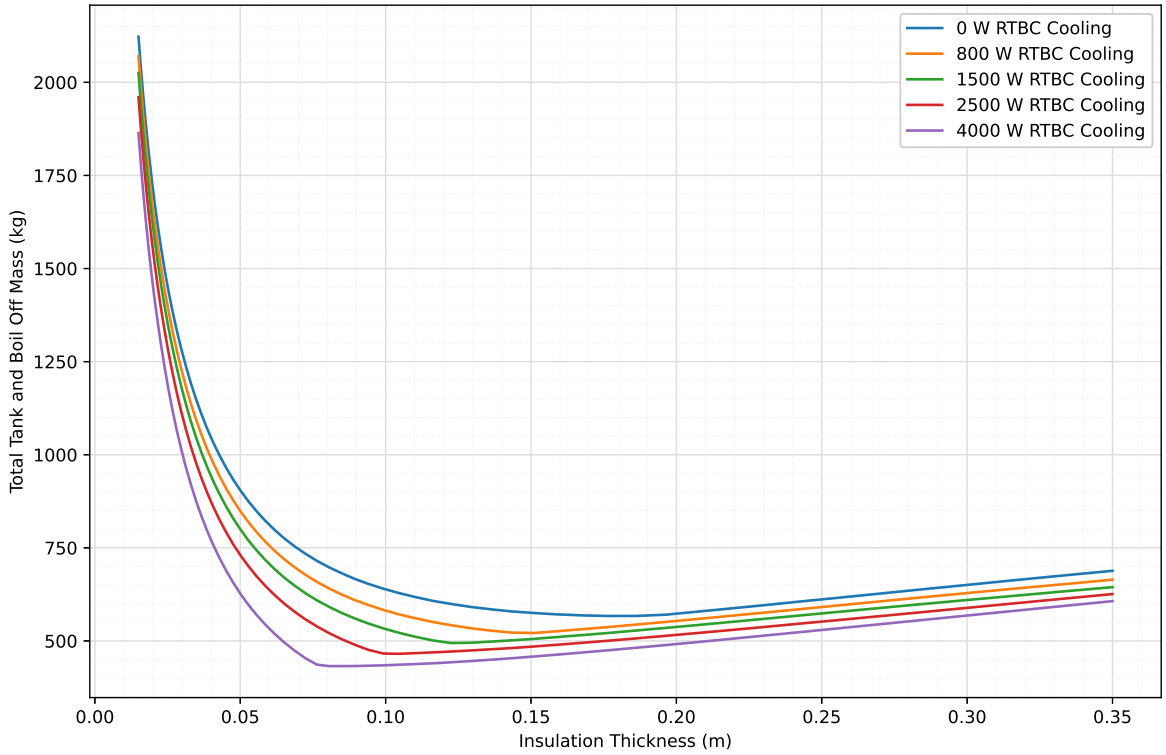

Figure 4.15: Effect of insulation thickness on overall tank system weight (including boil-off mass), for various RTBC cooling power capacities. Note that two tank systems (and two RTBC) are present in the Flying-V

It can be observed in Figure 4.15 that for increasing cooling power, the total tank and boil-off mass decreases. Moreover, the point of minimum mass moves to lower insulation thicknesses. This is not surprising, as an RTBC provides active cooling which replaces the passive cooling provided by the insulation. The combined effect is that an RTBC can have a weight saving that is considerably more when the insulation thickness is integrated with the conceptual RTBC design. To illustrate this, at an insulation thickness of 0.20 m an RTBC of 4000 W can have a weight saving of 85 kg due to boil-off reduction. Reducing the insulation thickness, however, can save up to an additional 53 kg per tank. This is due to a decrease in the minimum insulation thickness of 60%. These weight savings of 138 kg

are an indication of the maximum mass the 4000 W RTBC system must have, in order to have direct weight savings. Similarly, the maximum mass of the other examined RTBC systems can be obtained from Figure 4.15. These maximum mass limits are, however, lower than the weight estimate of the 800 W RTBC of 304 kg. The RTBC systems with a cooling capacity above 800 W are expected to weigh more, and require more input power. This demonstrates that, despite extra weight savings due to a decrease in insulation thickness, there is currently no direct weight benefit of incorporating high-capacity RTBC into the design. As more advanced RTBC are designed in the future, however, the mass of the system will decrease, and the use of RTBC might become beneficial. For an 800 W RTBC and an insulation thickness for minimum total tank and boil-off mass, the maximum system weight is approximately 50 kg, which requires an 84% decrease in mass from the current weight estimate.

4.4.3. Effect of insulation thickness and cooling power on cruise range

In Chapter 1, the importance of hydrogen storage and handling onboard aircraft was stressed for future net-zero flight. Specifically, boil-off has been identified as the primary technological challenge for long-term storage of cryogenic hydrogen in sustainable flight. The study by Woensel [94] on the integration of a liquid hydrogen fuel tank into the concept of the Flying-V, concluded that the available hydrogen volume is insufficient for equivalent flight performance (see also Figure 4.1). The results in Figure 4.15 showed that the use of an RTBC can reduce the minimum insulation thickness considerably, up to 60% for 4000 W of cooling. As the insulation thickness is located on the inside of the structural tank wall (Section 3.1.1), this decrease in insulation thickness increases the available fuel volume. The effect of using an RTBC on the flight performance of the Flying-V concept, specifically the cruise range, is therefore analysed. In this analysis, the insulation thickness is varied for various cooling powers, and the resulting vacant volume is substituted by fuel.

The flight performance analysis considered in this research is that of maximum passengers (Section 4.1). As a result, the Flying-V concept is operating at its maximum take-off weight. When including an RTBC in the design, the OEW and MTOW increase and an iteration of the design of the aircraft should be performed. For the 800 W RTBC, this would increase the MTOW with 0.4%. Considering that the MTOW of the Flying-V hydrogen concept is a 32% decrease from the original FV-900 MTOW [94], a small increase in MTOW due to the incorporation of the RTBC is expected to be feasible. An iteration of the Flying-V design is, however, beyond the scope of the current research.

Alternatively, the payload weight can be reduced to offer available space for the inclusion of the RTBC. To illustrate, two RTBC of 800 W have a combined mass of 608 kg (Section 4.4.1). The Flying-V hydrogen concept configuration is designed for an average passenger weight of 75 kg, with 12 kg of luggage [74, 94]. In order to use the RTBC to cool the liquid hydrogen fuel tanks, the payload must be reduced by 7 passengers to maintain the same MTOW. Although this decreases the maximum number of passengers by 1.6% to 433 pax, it provides a means to get insights on the effect on aircraft range due to the synergy between the RTBC and insulation thickness. This study, therefore, is purely meant to give an illustration about the possible potential of using RTBC in future flight performance analysis.

Figure 4.16 shows the cruise range versus insulation thickness for various cooling power capacities. Note that no estimates of the weights of the 1500 W, 2500 W and 4000 W RTBC have been made. The effect on the reduction of maximum passengers is, therefore, not quantified and the corresponding analyses are qualitative. In Figure 4.16, it can be seen that the trends are similar to the inverse of the trends observed in Figure 4.15. When decreasing the insulation thickness, the range initially increases linearly due to the additional available volume. This linear increase stops at the same location when the minimum total tank and boil-off mass is reached in Figure 4.15. From this point onwards, the boil-off increases and the range increase flattens off towards a maximum range. At insulation thicknesses lower than this point, the boil-off mass increases more than the additional volume obtained by the reduction in insulation, and the range decreases. An interesting observation is that the linear part of the curve is extended for higher cooling power capacities, but the insulation thickness for maximum range is independent of cooling power.

At the linear part of the curves in Figure 4.16, between insulation thicknesses of 0.19 m to 0.225 m, it can be see that the curves are close to each other and the RTBC have little effect on the cruise range. This is not surprising, as at high insulation thicknesses the boil-off is at a minimum and the RTBC has little effect. When the design enters the non-linear part, i.e. when boil-off increases and starts to reduce the increase in range from the additional available volume, the RTBC has the most impact. When the insulation layer becomes too small, however, the impact of the RTBC diminishes again. This highlights the importance of insulation, and shows that RTBC cannot substitute insulation. Instead, RTBC must be used as an addition to proper insulation design. Note that the cruise range is slightly lower than reported in Section 4.4, as the recreated flight performance results from the original

study in that section did not include the boil-off in the mission profile due to falling within acceptable limits [94].

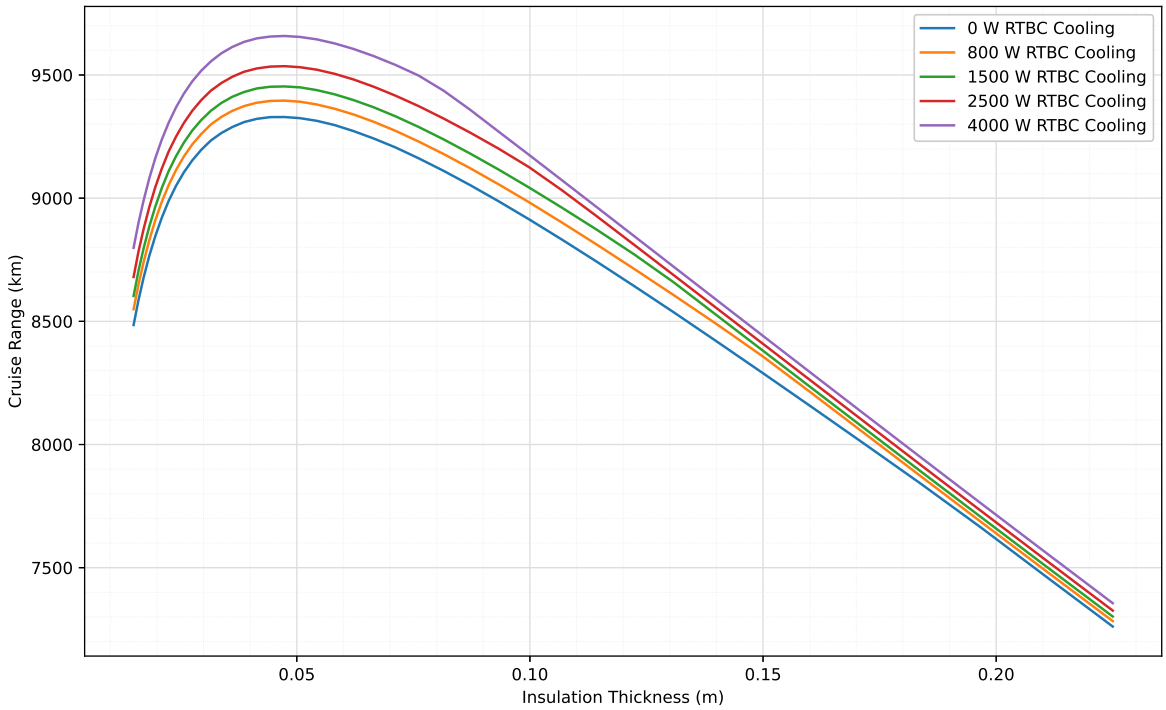

Figure 4.16: Effect of insulation thickness on cruise range, for various RTBC cooling power capacities

Figure 4.17 shows the boil-off and vented mass versus insulation thickness for various cooling power capacities. It can be observed that for each cooling power a certain insulation thickness exists, from which an increase in insulation thickness has little effect on the boil-off mass. Not surprisingly, this value is in close proximity to the insulation thickness for which the minimum total tank and boil-off mass is obtained in Figure 4.15. It can furthermore be observed, that for decreasing insulation thicknesses the percentage of boil-off mass that is vented overboard increases dramatically.

Looking at the trends displayed in Figures 4.16 and 4.17, two conclusions can be made. First, RTBC can significantly increase the cruise range with insulation thicknesses for minimum tank and boil-off mass, provided that a lower maximum passengers capacity is accepted. As an example, having a minimum tank and boil-off mass with no active cooling results in a cruise range of 7800 km. With a cooling power of 800 W, this increases to 8400 km. For a cooling power of 4000 W the cruise range increases to almost 9500 km. The insulation thickness for this increased range and a minimum tank and boil-off mass decreases with cooling power, whilst the insulation thickness for maximum range is independent of cooling power. This implies that there is an optimum cooling power, where the insulation thickness for maximum cruise range coincides with the insulation thickness for minimum tank and boil-off mass. This optimum cooling power is above the investigated 800 W in Section 4.4, and is expected to be up to one or two orders of magnitude higher. That is, the optimum RTBC cooling power for the hydrogen Flying-V concept is expected to fall within the range of 4-20 kW.

The second conclusion is that a decrease in insulation thickness can significantly increases the cruise range when high boil-off and venting is accepted. At the insulation thickness for maximum cruise range, the boil-off is up to 4 times greater than the boil-off at the insulation thickness for minimum tank and boil-off mass, depending on cooling power. Moreover, where the vented mass at the insulation thickness for minimum tank and boil-off mass is close to zero, this increases up to 300-550 kg at the insulation thickness for maximum cruise range, depending on cooling power.

The observation of the increase in boil-off, venting and their ratio for the insulation thickness for maximum cruise range suggests a new application of RTBC integration into the fuel system. If opted for the insulation thickness for maximum range, the venting will be significant and a high fraction of the boil-off mass. Rather than cooling the liquid, the RTBC can instead be used to liquefy the vented hydrogen and introduce it back into the tank as fuel. This closed-loop venting can save weight, as no big and heavy heat exchanger inside the tank needs to be used to cool the mixture. It is recommended to start future research into this novel integration of RTBC into aeronautical liquid hydrogen fuel systems.

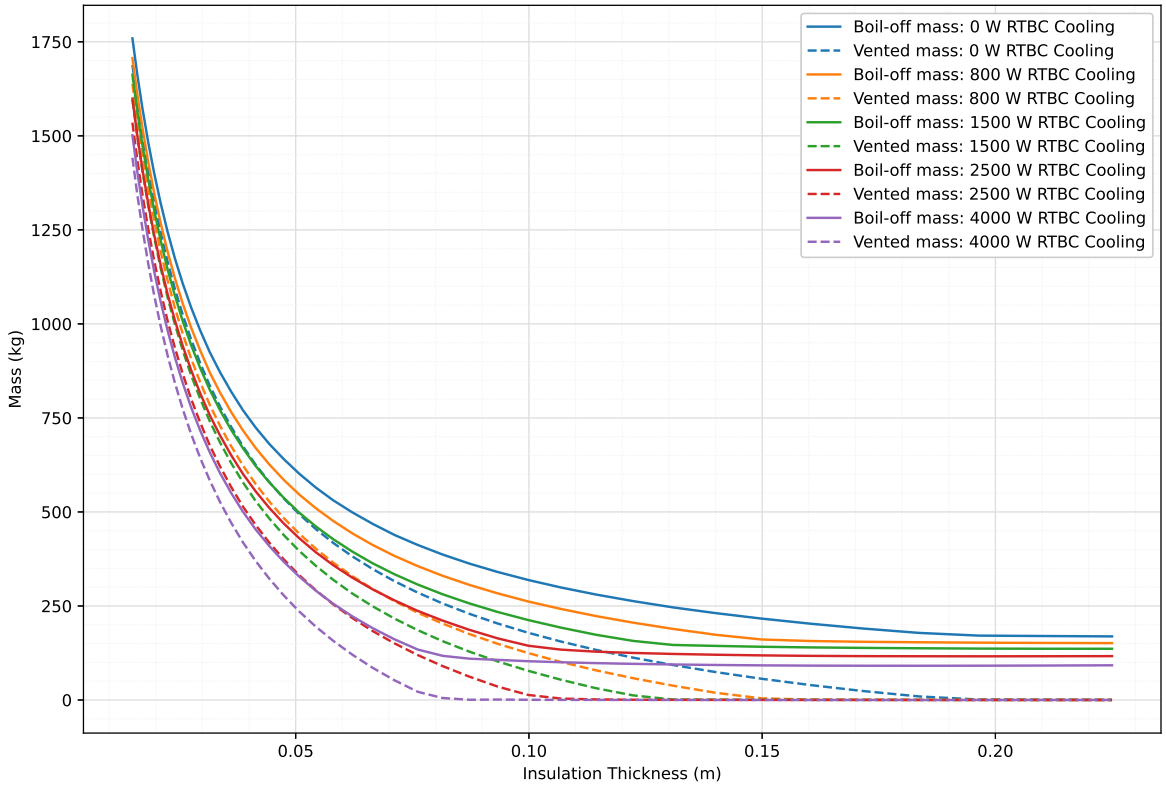

Figure 4.17: Effect of insulation thickness on boil-off and vented mass, for various RTBC cooling power capacities

To put the results into perspective, the range when departing from Schiphol Airport (AMS) is shown in Figure 4.18. This is done for the hydrogen Flying-V hydrogen concept by Woensel [94], the original kerosene Flying-V concept (FV-900) by Oosterom [74], and the Flying-V hydrogen concept with the addition of two 800 W RTBC, a lowered insulation thickness for maximum range, and a reduction in number of passengers from 440 to 433. For the concept with two 800 W RTBC, the range could be increased by almost 1000 km to 9880 km, which is just 900 km short of the range with kerosene. Figure 4.18 shows that the additional range of the concept with the RTBC expands the list of accessible destinations from AMS considerably. The range now includes the whole of North America and Africa, Japan, all of China, and the majority of Brazil and Mainland Southeast Asia.

The range of the concepts shown in Figure 4.18 are for concepts of the same take-off weight. In addition to comparing the concepts at the same take-off weight, a comparison with the same number of passengers can be made. From the payload-range diagram in Figure 4.1, the range of the Flying-V concepts with a reduction in take-off weight of 608 kg, i.e. 7 pax, can be determined. These values are reported in Table 4.14. In this table it can be seen that at the same payload weight, the addition of two 800 W RTBC to the hydrogen FV-900 can reduce the range gap towards the kerosene FV-900 with 46%.

Figure 4.18 and Table 4.14 demonstrate that, despite the conclusion that the RTBC has no weight benefit on its own for the exploration study in Section 4.4.1, the RTBC might increase the range significantly in combination with a reduction of insulation thickness. Furthermore, the study shows the maximum weight that the RTBC thermal management system must have in order to provide benefit for increasing the range of the Flying-V hydrogen concept. It can, therefore, be concluded that the RTBC might offer a valuable addition to the Flying-V design space for boil-off control in addition to careful design of the insulation and tank shape, and provided that the weight of the RTBC is lower than 304 kg.

Note that in the study performed in this section, the increased fuel weight and the decreased tank weight are not taken into account in the MTOW and OEW. Additionally, the operation of the RTBC and its power requirement is not included. It is therefore a simplified study, and it is recommended to perform an integrated study on the use of the RTBC and insulation thickness reduction, with the total aircraft energy system, the structural design domain, and the flight performance domain. Doing so would provide insights into the synergy between RTBC and various aircraft systems, and might provide possibilities for weight savings. Note furthermore that the boil-off and venting results reported

Table 4.14: The range of three Flying-V concepts, for a passenger capacity of 433 and 440 pax

n_{pax}	Range [km]		
	FV-900 Hydrogen Woensel	FV-900 Oosterom	800 W RTBC, Max Range
433 pax	8987	10936	9880
440 pax	8900	10800	-

are conservative (Section 3.4.1), and thus underestimate the cruise range. Additionally, the mission considered is that of the maximum number of passengers, which is the lower range limit (Section 4.1). Despite the simplifications of this study, multiple options are identified to increase the feasibility of carbon neutral long range flight using liquid hydrogen as fuel. The conservative estimations of the model merely increase this expected feasibility.

Figure 4.18: The range of three Flying-V concepts at the same Take-off Weight, departing from Schiphol Airport (AMS)

5

Conclusion

Climate change is an important problem in current society. In the climate change debate, civil aviation is a highly controversial topic. Although the current global CO_2 emissions are only 2.5% [56, 32], civil aviation is expected to emit almost 50% of the CO_2 emissions in the transport sector by 2070 [50]. It is, therefore, important that immediate action is taken to develop technologies for net-zero flight. Hydrogen aircraft are an excellent alternative to the current kerosene aircraft, and appear to be the most viable solution for net-zero flight in the long term [91, 2]. The biggest technological challenge for hydrogen aircraft is to sustain a low boil-off rate for the LH_2 fuel tanks. Currently, aircraft designers have two ways to control this boil-off. That is, the use of insulation, and careful design of the tank shape. The research in this thesis explores an additional method, i.e. the active cooling of the LH_2 mixture in the fuel tank. It has been identified that Reverse Turbo-Brayton cycles are the most interesting research topic for high-capacity aerospace cryocoolers for boil-off reduction.

The research in this thesis is, therefore, focused on high-capacity Reverse Turbo-Brayton Cryocoolers (RTBC) for hydrogen aircraft, and the modelling of boil-off for airborne LH_2 tanks. This is in line with the Climate Action mission of the Delft University of Technology, that states that "TU Delft will harness its innovative powers to support the world-wide transition to non-fossil energy, and adaptation of the living environment to the consequences of global warming." [1] The work in this thesis is one of the first research efforts on aeronautical RTBC outside the United States, and one of few public research efforts on this topic performed in the world. Additionally, this work describes the first detailed numerical thermodynamic modelling effort of cryogenic liquid hydrogen fuel storage in aircraft.

The purpose of this research is to show the potential of the use of, and to open the public research space in airborne cryocoolers for cryogenic hydrogen storage in the next generation hybrid/electric aircraft. To fulfil this purpose, two research areas have been investigated:

- The design and modelling methodology of a liquid hydrogen fuel tank model, a Reverse Turbo-Brayton Cryocooler system model, and a conceptual compressor design for Reverse Turbo-Brayton Cryocoolers
- The integrated modelling of the three aforementioned models for an exploration study of the liquid hydrogen fuel tank concept of the carbon neutral long range Flying-V aircraft (Woensel [94])

Based on the results obtained, the following main conclusions can be drawn.

Modelling and design effort

1. A dynamic, modular, hierarchically structured, a-causal declarative model has been developed based on conservation laws and the first principles of thermodynamics. This model can be used for the conceptual design and modelling of liquid hydrogen fuel tanks in long range aircraft with and without active cooling, in order to minimise boil-off. This model has been verified with two verification cases: a theoretical example of boil-off in a spherical nitrogen tank, and the results of a study performed by NASA that explored various options for hydrogen storage for aircraft applications. Despite the lack of validation data, the outcomes of the model have been compared to test results of NASA's Ground Operations Demonstration Unit for Liquid Hydrogen. It was found that the developed model gives results with a conservative margin, over-predicting boil-off and venting.

[1] https://www.tudelft.nl/en/tu-delft-climate-institute/tu-delft-position-on-climate-action

2. A single-stage Reverse Turbo-Brayton Cryocooler system model has been developed based on fundamental thermodynamics, with the option to optimise the system design for the maximum Coefficient of Performance (COP). This model has been verified, and validated with two validation cases: the only operational RTBC application to date in the Hubble Space Telescope, and a detailed validated model intended for NASA's zero boil-off (ZBO) liquid hydrogen storage in space. With this system model, the performance parameters and TS-diagram of the system can be obtained, whilst only knowing information about the subsystem efficiencies, cooling load temperature, aftercooler outlet temperature, compressor pressure ratio, and the cooling power.
3. The design methodology of an in-house model for the conceptual design of centrifugal compressors based on Local Dimensionless or Scaling Analysis has been presented. An alternative for its multi-objective design optimisation was developed, in order to document the influence that the design variables and parameters have on the design during optimisation. With this developed Multi-Dimensional Parametric Design Optimisation Tool (MDPDOT), multi-dimensional parametric studies can be visualised using process-based parallelism.

Integrated exploration study

1. A high-capacity miniature compressor for RTBC has been designed, with an efficiency of 86%. This is an improvement of the net efficiency with 20% compared to current state-of-the-art low capacity RTBC compressors.
2. The influence of the design variables and parameters of the conceptual compressor have been documented during optimisation. The optimal conceptual design of the compressor is such that high impeller outflow angles are obtained, in an attempt to minimise clearance losses. In combination with the high rotational velocity, the optimal design is operating close to diffuser instability.
3. It has been found that manufacturing constraints have a substantial effect on the compressor stage performance, and that at the current design point the extensive majority of the loss is caused by friction.
4. A 22 K, 800 W RTBC design has been presented with a COP of 41% of the Carnot COP. This is almost a doubling in efficiency compared to state-of-the-art low capacity RTBC.
5. It has been shown that the compressor efficiency dictates the optimum system pressure ratio, power requirements and COP. On the other hand, it has been shown that the system pressure ratio, COP, and system weight are most sensitive to the recuperator thermal effectiveness. Accurate estimates of the turbomachinery efficiency and recuperator thermal effectiveness are necessary to design the RTBC.
6. Based on the integrated modelling effort, it has been shown that there is currently no benefit of using an RTBC for the active cooling of the hydrogen fuel tank in the Flying-V concept in its current state. The expected weight of 304 kg and required power of 25.5 kW do not outweigh the reduction in venting and the decrease in boil-off mass of 44 kg.
7. It has been shown that RTBC decreases the insulation thickness for minimum total tank and boil-off mass. With the inclusion of a 4 kW RTBC, the minimum insulation thickness can be decreased by 60%. This increases weight savings by more than 60%, compared to excluding the reduction of insulation thickness in the study.
8. A study has been performed to quantify the effects of insulation thickness decrease due to RTBC on the range. This has shown that independent of active cooling, a decrease in insulation thickness can significantly increases the cruise range when high boil-off and venting is accepted.
9. The study on range has also shown that RTBC can significantly increase the cruise range of designs for minimum tank and boil-off mass. For an 800 W RTBC, the range could be increased by almost 1000 km to a total of 9880 km, which is only 900 km short of the range with kerosene. It is suggested that an optimum cooling power exists within the range of 4-20 kW, for which the design for minimum tank and boil-off mass coincides with the design for maximum range.

Overall conclusion

From the results of the study, it is concluded that the RTBC might offer a valuable addition to the Flying-V design space for boil-off control in addition to careful design of the insulation and tank shape, and provided that the weight of the RTBC is lower than 304 kg.

5.1. Limitations and Recommendations

The main limitations of this research, and the recommendations to address them are described in the following.

1. The liquid hydrogen fuel tank model uses generalised experimental data for the internal heat transfer relations from the 1980s. The effect is the over-estimation of heat transfer to the liquid compared to the heat transfer towards the vapour, resulting in over-estimations of boil-off and venting. New experiments, specific to cryogenic hydrogen tanks in aircraft, should be conducted in order to establish new dimensionless coefficients that can be used for the internal heat transfer relations.
2. The liquid hydrogen fuel tank model does not take stratification into account, which can result in a slight deviation in the pressure and temperature transients. A future update of the model should include the effects of stratification without over-complicating the model, such that it can still be used in the conceptual design phase.
3. The validation of the liquid hydrogen fuel tank starts from a false equilibrium starting condition, or a fixed state initialisation with a wrong starting vapour temperature. A future study should perform the validation with correct starting conditions to eliminate the artificial initial transient this created.
4. During construction of the liquid hydrogen fuel tank, the hypothesis that no transverse conduction occurs in the wall was used and verified. A future update of the model should include this transverse conduction, as the hypothesis will not generally hold for vapour temperatures higher than that observed during the simulations in this research.
5. The detailed structural design and performance of the compressor is not taken into account by the in-house model, whilst it has been identified to have a substantial effect on the stage performance. Future research should include detailed and accurate manufacturing constraints, and quantify an accurate estimation of the centrifugal stresses throughout the compressor.
6. The RTBC system model uses estimations of component efficiencies based on literature of low capacity RTBC. The model can be improved by incorporating conceptual models of the recuperator, heat exchangers, and turbine such that high-capacity RTBC systems can be designed with more certainty in the performance results and weight estimations can be obtained.
7. The RTBC system model currently only supports a single stage design. The model should be extended to include multi-stage designs, and the possibility of the integration into other thermodynamic systems.
8. The exploration study on the range of the aircraft does not take the increased fuel weight, the decreased tank weight, changes in aircraft structural weight, nor the RTBC power requirement into account. A future effort should contain an integrated study on the use of the RTBC and insulation thickness reduction, with the total aircraft energy system, the structural design domain, and the flight performance domain.

5.2. Outlook

Based on the results obtained in this work and the experience gained during, the following items are envisaged as future research extensions of this thesis.

1. The three models discussed in this report can be used independently for other research purposes. Envisioned applications are novel hydrogen aircraft concepts such as AeroDelft, cooling of superconducting components of electric flight, and multi-dimensional parametric studies of high-speed miniature compressors such as for aircraft environmental control systems.
2. As all three models can be accessed and run from the same coding environment, it is possible to integrate the three models into one integrated model. A future study should create this integrated model for liquid hydrogen fuel systems, such that it provides the possibility for performing multidisciplinary design analysis and optimisation (MDO).
3. In the exploration study of this research, only the cruise phase was considered. Further studies should focus on an integrated study with aircraft logistics, to investigate the effect of the aircraft's hold period on boil-off behaviour. Additionally, future studies should use the liquid hydrogen tank model to investigate the boil-off behaviour of all other phases of flight, to have an understanding of the required RTBC operation throughout the mission.
4. Rather than cooling the liquid hydrogen fuel tank, it has been opted that RTBC can instead be used to liquefy the vented hydrogen and introduce it back into the tank as fuel. This closed-loop venting can save weight, as no big and heavy heat exchanger inside the tank needs to be used to cool the mixture. Moreover, the heat rejection of the RTBC might be of use for other aircraft systems. Future efforts should include studies on novel integration of RTBC into the fuel system and other aircraft systems.

References

[1] D. Acharya et al. “Systems Design, Fabrication, and Testing of a High-Speed Miniature Motor for Cryogenic Cooler”. In: *International Journal of Rotating Machinery* 2009 (2009), pp. 1–9. ISSN: 1023-621X. DOI: 10.1155/2009/936251.

[2] E. J. Adler and J. R. R. A. Martins. “Hydrogen-Powered Aircraft: Fundamental Concepts, Key Technologies, and Environmental Impacts”. In: *Fuel* 32 (2022), p. 7.

[3] M. J. Assael et al. “Correlation of the Thermal Conductivity of Normal and Parahydrogen from the Triple Point to 1000 K and up to 100 MPa”. In: *Journal of Physical and Chemical Reference Data* 40.3 (Sept. 2011), p. 033101. ISSN: 0047-2689. DOI: 10.1063/1.3606499.

[4] J. C. Aydelott. *Normal gravity self-pressurization of 9-inch- (23 cm) diameter spherical liquid hydrogen tankage*. Tech. rep. Cleveland, Ohio: National Aeronautics and Space Administration, 1967.

[5] J. C. Aydelott and C. M. Spuckler. *Venting of Liquid Hydrogen Tankage*. Cleveland, Ohio: National Aeronautics and Space Administration, June 1969.

[6] A. Bejan. *Convection Heat Transfer*. Wiley, Apr. 2013. ISBN: 9780470900376. DOI: 10.1002/9781118671627.

[7] A. Bejan. “Note on Gill’s solution for free convection in a vertical enclosure”. In: *Journal of Fluid Mechanics* 90.3 (Feb. 1979), pp. 561–568. ISSN: 0022-1120. DOI: 10.1017/S0022112079002391.

[8] J. Benad and R. Vos. “Design Of A Flying V Subsonic Transport”. In: *33rd Congress of the International Council of the Aeronautical Sciences*. 2022.

[9] L. G. Bolshinskiy et al. *Tank System Integrated Model: A Cryogenic Tank Performance Prediction Program*. Tech. rep. Huntsville, Alabama: National Aeronautics and Space Administration, Apr. 2017. URL: http://www.sti.nasa.gov.

[10] R. D. Bradshaw. *Evaluation and Application of Data from Low Gravity Orbital Experiment*. Tech. rep. San Diego, CA: Convair Division of General Dynamics, Apr. 1970.

[11] J. J. Breedlove, P. J. Magari, and G. W. Miller. “Cryocooler for air liquefaction onboard large aircraft”. In: *AIP Conference Proceedings*. Vol. 985. 2008, pp. 838–845. ISBN: 9780735405042. DOI: 10.1063/1.2908678.

[12] J. J. Breedlove et al. “Life and Reliability Characteristics of Turbo-Brayton Coolers”. In: *Cryocoolers*. Vol. 11. Boston, MA: Springer US, 2002, pp. 489–497. DOI: 10.1007/0-306-47112-4{_}62.

[13] G. D. Brewer. *Hydrogen Aircraft Technology*. CRC Press, Inc., 1991. ISBN: 9780203751480. DOI: 10.1201/9780203751480.

[14] F. Casella and A. Leva. “Modelica open library for power plant simulation: design and experimental validation”. In: *3rd International Modelica Conference*. Ed. by Peter Fritzson. The Modelica Association. Sweden, Nov. 2003, pp. 41–50. URL: https://modelica.org/events/Conference2003/index_html.html.

[15] M. Casey and C. Robinson. *Radial Flow Turbocompressors*. Cambridge University Press, June 2021. ISBN: 9781108241663. DOI: 10.1017/9781108241663.

[16] H. M. Chang et al. “Thermodynamic design of 10 kW Brayton cryocooler for HTS cable”. In: *AIP Conference Proceedings*. Vol. 1434. 57. 2012, pp. 1664–1671. ISBN: 9780735410206. DOI: 10.1063/1.4707099.

[17] P. Colonna et al. *Modelling, Simulation and Application of Propulsion and Power Systems [PowerPoint slides]*. Brightspace@TU Delft, 2021. URL: https://brightspace.tudelft.nl/.

[18] A. J. Colozza. *Hydrogen Storage for Aircraft Applications Overview*. Tech. rep. 2002. URL: http://www.sti.nasa.gov.

[19] Computational Fluid Dynamics Committee. *Guide for the Verification and Validation of Computational Fluid Dynamics Simulations (AIAA G-077-1998(2002))*. Washington, DC: American Institute of Aeronautics and Astronautics, Inc., Jan. 1998. DOI: 10.2514/4.472855.001.

[20] J. H. Corpening. "Analytical Modeling of Pressurization and Cryogenic Propellant Conditions for Liquid Rocket Based Vehicle Designs". In: *Teledyne Brown Engineering* (2010).

[21] K. Cragin, J. McCormick, and M. V. Zagarola. "Development of a Cryogenic Compressor for Airborne Cryocoolers". In: *IOP Conference Series: Materials Science and Engineering*. Vol. 755. 1. Institute of Physics Publishing, June 2020. DOI: 10.1088/1757-899X/755/1/012032.

[22] F. Datchi, P. Loubeyre, and R. LeToullec. "Extended and accurate determination of the melting curves of argon, helium, ice (H2O) and hydrogen (H2)". In: *Physical Review B* 61.10 (Mar. 2000), pp. 6535–6546. ISSN: 0163-1829. DOI: 10.1103/PhysRevB.61.6535.

[23] J. M. Delhaye. "Jump conditions and entropy sources in two-phase systems. Local instant formulation". In: *International Journal of Multiphase Flow* 1.3 (June 1974), pp. 395–409. ISSN: 03019322. DOI: 10.1016/0301-9322(74)90012-3.

[24] D. Deserranno, A. Niblick, and M. V. Zagarola. "Testing of a 1 kW-Class Cryogenic Turboalternator". In: *Cryocoolers* 18 (2014). Ed. by S D Miller and R G Ross.

[25] D. Deserranno et al. "Optimization of a Brayton cryocooler for ZBO liquid hydrogen storage in space". In: *Cryogenics* 64 (2014), pp. 172–181. ISSN: 00112275. DOI: 10.1016/j.cryogenics.2014.04.025.

[26] D. Deserranno et al. "Performance Testing of a High Effectiveness Recuperator for High Capacity Turbo-Brayton Cryocoolers". In: *Cryocoolers* 19 (2016). Ed. by S D Miller and R G Ross.

[27] A. K. Dhillon and P. Ghosh. "Performance characteristics map using exergy analysis of reverse Brayton cryocooler for HTS applications: Selection, Optimization, Design and Operational guidelines". In: *Cryogenics* 106 (Mar. 2020). ISSN: 00112275. DOI: 10.1016/j.cryogenics.2019.103024.

[28] D. Eckardt. "Detailed Flow Investigations Within a High-Speed Centrifugal Compressor Impeller". In: *Journal of Fluids Engineering* 98.3 (Sept. 1976), pp. 390–399. ISSN: 0098-2202. DOI: 10.1115/1.3448334.

[29] D. Eckardt. "Instantaneous Measurements in the Jet-Wake Discharge Flow of a Centrifugal Compressor Impeller". In: *Journal of Engineering for Power* 97.3 (July 1975), pp. 337–345. ISSN: 0022-0825. DOI: 10.1115/1.3445999.

[30] D. Eckardt. *Investigation of the Jet-Wake Flow of a Highly Loaded Centrifugal Compressor Impeller*. Tech. rep. NASA, Jan. 1978. URL: https://ntrs.nasa.gov/citations/19780008108.

[31] J. N. Everitt and Z. S. Spakovszky. "An Investigation of Stall Inception in Centrifugal Compressor Vaned Diffusers". In: *Volume 7: Turbomachinery, Parts A, B, and C*. ASMEDC, Jan. 2011, pp. 1737–1749. ISBN: 978-0-7918-5467-9. DOI: 10.1115/GT2011-46332.

[32] P. Friedlingstein et al. "Global Carbon Budget 2019". In: *Earth System Science Data* 11.4 (Dec. 2019), pp. 1783–1838. ISSN: 1866-3516. DOI: 10.5194/essd-11-1783-2019.

[33] A. E. Gill. "The boundary-layer regime for convection in a rectangular cavity". In: *Journal of Fluid Mechanics* 26.3 (Nov. 1966), pp. 515–536. ISSN: 0022-1120. DOI: 10.1017/S0022112066001368.

[34] A. Gittens et al. *Aviation Benefits Report*. Tech. rep. The Global Aviation Industry High-level Group, 2019. URL: https://www.icao.int/sustainability/Documents/AVIATION-BENEFITS-2019-web.pdf.

[35] A. Giuffré. "Integrated Design Optimization of Electrically-Driven Vapor Compression Cycle Systems for Aircraft". PhD thesis. Delft: Delft University of Technology, 2023.

[36] A. Giuffré, P. Colonna, and C. De Servi. "Dynamic thermal model of passenger aircraft for the estimation of the cabin cooling and heating requirements". In: *Applied Thermal Engineering* 244 (May 2024). ISSN: 13594311. DOI: 10.1016/j.applthermaleng.2024.122641.

[37] A. Giuffré, P. Colonna, and M. Pini. "Design Optimization of a High-Speed Twin-Stage Compressor for Next-Gen Aircraft Environmental Control System". In: *Journal of Engineering for Gas Turbines and Power* 145.3 (Mar. 2023). ISSN: 0742-4795. DOI: 10.1115/1.4056022.

[38] A. Giuffré, P. Colonna, and M. Pini. “The Effect of Size and Working Fluid on the Multi-Objective Design of High-Speed Centrifugal Compressors”. In: *International Journal of Refrigeration* 143 (Nov. 2022), pp. 43–56. ISSN: 01407007. DOI: 10.1016/j.ijrefrig.2022.06.023.

[39] A. Giuffré and M. Pini. “Design guidelines for axial turbines operating with non-ideal compressible flows”. In: *Journal of Engineering for Gas Turbines and Power* 143.1 (Jan. 2021). ISSN: 15288919. DOI: 10.1115/1.4049137.

[40] D. S. Glaister et al. “An Overview of the Performance and Maturity of Long Life Cryocoolers for Space Applications”. In: *Cryocoolers*. Vol. 10. Boston, MA: Springer US, 2002, pp. 1–19. DOI: 10.1007/0-306-47090-X{_}1.

[41] C. Gong and T. Habetler. “A novel rotor design for ultra-high speed switched reluctance machines over 1 million rpm”. In: *2017 IEEE International Electric Machines and Drives Conference (IEMDC)*. IEEE, May 2017, pp. 1–6. ISBN: 978-1-5090-4281-4. DOI: 10.1109/IEMDC.2017.8002290.

[42] R. Hall. *Simulation of Ideal-Gas Flow by Nitrogen and Other Selected Gases at Cryogenic Temperatures*. NASA, 1981.

[43] L. J. Hastings et al. “An overview of NASA efforts on zero boiloff storage of cryogenic propellants”. In: *Cryogenics* 41.11-12 (Nov. 2001), pp. 833–839. ISSN: 0011-2275. DOI: 10.1016/S0011-2275(01)00176-X.

[44] L. J. Hastings et al. *Spray Bar Zero-Gravity Vent System for On-Orbit Liquid Hydrogen Storage*. Tech. rep. Marshall Space Flight Center, Alabama: National Aeronautics and Space Administration, Oct. 2003. URL: https://ntrs.nasa.gov/citations/20040000092.

[45] R. W. Hill, J. K. Hilderbrand, and M. V. Zagarola. “An Advanced Compressor for Turbo-Brayton Cryocoolers”. In: *Cryocoolers* 16 (2011), pp. 391–396.

[46] J. I. Hochstein, H. C. Ji, and J. C. Aydelott. “Effect Of Subcooling on the On-Orbit Pressurization Rate of Cryogenic Propellant Tankage”. In: *AIAA Paper*. AIAA, 1986. DOI: 10.2514/6.1986-1253.

[47] Y. Hou et al. “Developments in reverse Brayton cycle cryocooler in China”. In: *Cryogenics* 46.5 SPEC. ISS. (2006), pp. 403–407. ISSN: 00112275. DOI: 10.1016/j.cryogenics.2005.11.021.

[48] G. Hwang and S. Jeong. “Pressure loss effect on recuperative heat exchanger and its thermal performance”. In: *Cryogenics* 50.1 (Jan. 2010), pp. 13–17. ISSN: 00112275. DOI: 10.1016/j.cryogenics.2009.10.002.

[49] F. Incropera et al. *Fundamentals of Heat and Mass Transfer*. 6th Edition. John Wiley & Sons, 2007.

[50] International Energy Agency. *Energy Technology Perspectives 2020*. Tech. rep. Paris: International Energy Agency, 2020. URL: https://www.iea.org/reports/energy-technology-perspectives-2020.

[51] D. Japikse. “A Critical Evaluation of Three Centrifugal Compressors With Pedigree Data Sets: Part 5—Studies in Component Performance”. In: *Journal of Turbomachinery* 109.1 (Jan. 1987), pp. 1–9. ISSN: 0889-504X. DOI: 10.1115/1.3262064.

[52] R. A. Kimble et al. “Wide Field Camera 3: a powerful new imager for the Hubble Space Telescope”. In: ed. by Jacobus M. Oschmann Jr., Mattheus W. M. de Graauw, and Howard A. MacEwen. July 2008, 70101E. DOI: 10.1117/12.789581.

[53] H. Kobayashi et al. “A study on the rotating stall of centrifugal compressors. 2nd report, Effect of vaneless diffuser inlet shape on rotating stall.” In: *Transactions of the Japan Society of Mechanical Engineers Series B* 56.529 (1990), pp. 2646–2651. ISSN: 0387-5016. DOI: 10.1299/kikaib.56.2646.

[54] D. A. Kouremenos and X. K. Kakatsios. “The three isentropic exponents of dry steam”. In: *Forschung im Ingenieurwesen* 51.4 (July 1985), pp. 117–122. ISSN: 0015-7899. DOI: 10.1007/BF02558416.

[55] J. W. Leachman et al. “Fundamental Equations of State for Parahydrogen, Normal Hydrogen, and Orthohydrogen”. In: *Journal of Physical and Chemical Reference Data* 38.3 (Sept. 2009), pp. 721–748. ISSN: 0047-2689. DOI: 10.1063/1.3160306.

[56] D. S. Lee et al. “The contribution of global aviation to anthropogenic climate forcing for 2000 to 2018”. In: *Atmospheric Environment* 244 (Jan. 2021), p. 117834. ISSN: 13522310. DOI: 10.1016/j.atmosenv.2020.117834.

[57] K. Lee et al. “Design and performance test of 2 kW class reverse brayton cryogenic system”. In: *Energies* 13.19 (Oct. 2020). ISSN: 19961073. DOI: 10.3390/en13195089.

[58] E. W. Lemmon et al. “NIST standard reference database 23: reference fluid thermodynamic and transport properties-REFPROP, Version 10.0, National Institute of Standards and Technology”. In: *Standard Reference Data Program, Gaithersburg* (2018).

[59] S. Li and L. R. Petzold. *Design of new DASPK for sensitivity analysis*. Tech. rep. UCSB Department of Computer Science, Sept. 1999.

[60] J. H. Lienhard IV and J. H. Lienhard V. *A Heat Transfer Textbook*. 5th ed. Phlogiston Press, Aug. 2020.

[61] C. S. Lin, N. T. Van Dresar, and M. M. Hasan. “Pressure control analysis of cryogenic storage systems”. In: *Journal of Propulsion and Power* 20.3 (2004), pp. 480–485. ISSN: 15333876. DOI: 10.2514/1.10387.

[62] Z. Liu, Y. Dong, and Y. Li. “An experimental study of frost formation on cryogenic surfaces under natural convection conditions”. In: *International Journal of Heat and Mass Transfer* 97 (June 2016), pp. 569–577. ISSN: 00179310. DOI: 10.1016/j.ijheatmasstransfer.2016.02.019.

[63] A. K. Majumdar et al. “Generalized Fluid System Simulation Program (GFSSP), Version 6”. In: *51st AIAA/SAE/ASEE Joint Propulsion Conference*. Orlando, FL: American Institute of Aeronautics and Astronautics Inc, AIAA, July 2015. ISBN: 9781624103216. DOI: 10.2514/6.2015-3850.

[64] M. Marconcini et al. “A Three-Dimensional Time-Accurate Computational Fluid Dynamics Simulation of the Flow Field Inside a Vaneless Diffuser During Rotating Stall Conditions”. In: *Journal of Turbomachinery* 139.2 (Feb. 2017). ISSN: 0889-504X. DOI: 10.1115/1.4034633.

[65] J. R. Mason and R. D. Southwick. *Large Liquid Rocket Engine Transient Performance Simulation System*. Tech. rep. West Palm Beach, FL: United Technologies Corporation, Pratt & Whitney, 1991.

[66] S. Mattick et al. “Progress in Modeling Pressurization in Propellant Tanks”. In: American Institute of Aeronautics and Astronautics (AIAA), July 2010. DOI: 10.2514/6.2010-6560.

[67] E. Mendez Ramos. “Enabling Conceptual Design and Analysis of Cryogenic In-Space Vehicles through the Development of an Extensible Boil-Off Model”. PhD thesis. Georgia Institute of Technology, 2021.

[68] J. Meserole et al. “Mixing-induced ullage condensation and fluid destratification”. In: *23rd Joint Propulsion Conference*. Reston, Virigina: American Institute of Aeronautics and Astronautics, June 1987. DOI: 10.2514/6.1987-2018.

[69] A. Mulero, I. Cachadiña, and M. I. Parra. “Recommended Correlations for the Surface Tension of Common Fluids”. In: *Journal of Physical and Chemical Reference Data* 41.4 (Dec. 2012), p. 043105. ISSN: 0047-2689. DOI: 10.1063/1.4768782.

[70] C. D. Muzny, M. L. Huber, and A. F. Kazakov. “Correlation for the Viscosity of Normal Hydrogen Obtained from Symbolic Regression”. In: *Journal of Chemical & Engineering Data* 58.4 (Apr. 2013), pp. 969–979. ISSN: 0021-9568. DOI: 10.1021/je301273j.

[71] A. Niblick, J. Cox, and M. V. Zagarola. “A Lightweight, High-Effectiveness Recuperator for Next-Generation Airborne Cryocoolers”. In: *International Cryocooler Conference*. Ed. by S D Miller, R G Ross, and J R Raab. Boulder, CO, 2018.

[72] W. U. Notardonato et al. “Zero boil-off methods for large-scale liquid hydrogen tanks using integrated refrigeration and storage”. In: *IOP Conference Series: Materials Science and Engineering* 278 (Dec. 2017), p. 012012. ISSN: 1757-8981. DOI: 10.1088/1757-899X/278/1/012012.

[73] G. Onorato. “Fuel Tank Integration for Hydrogen Airliners”. PhD thesis. Delft: Delft University of Technology, Aug. 2021. URL: http://resolver.tudelft.nl/uuid:5700b748-82c6-49c9-b94a-ad97c798e119.

[74] W. J. Oosterom. *Flying-V Family Design (MSc Thesis)*. Delft: Delft University of Technology, June 2021. URL: http://repository.tudelft.nl/..

[75] L. R. Petzold. “A Description of DASSL: A Differential/Algebraic System Solver”. In: Montreal, Aug. 1982.

[76] M. Pini. *Turbomachinery [PowerPoint slides]*. Brightspace@TU Delft, 2021. URL: https://brightspace.tudelft.nl/.

[77] D. Plachta and P. Kittel. “An updated zero boil-off cryogenic propellant storage analysis applied to upper stages or depots in an LEO environment”. In: *38th AIAA/ASME/SAE/ASEE Joint Propulsion Conference and Exhibit*. 2002. ISBN: 9781624101151. DOI: 10.2514/6.2002-3589.

[78] D. Plachta et al. “NASA cryocooler technology developments and goals to achieve zero boil-off and to liquefy cryogenic propellants for space exploration”. In: *Cryogenics* 94 (Sept. 2018), pp. 95–102. ISSN: 00112275. DOI: 10.1016/j.cryogenics.2018.07.005.

[79] D. W. Plachta and M. C. Guzik. “Cryogenic boil-off reduction system”. In: *Cryogenics* 60 (Mar. 2014), pp. 62–67. ISSN: 00112275. DOI: 10.1016/j.cryogenics.2013.12.006.

[80] X. Qiu et al. “Analysis and Validation of a Unified Slip Factor Model for Impellers at Design and Off-Design Conditions”. In: *Journal of Turbomachinery* 133.4 (Oct. 2011). ISSN: 0889-504X. DOI: 10.1115/1.4003022.

[81] Th. Rettelbach et al. “Thermal conductivity of evacuated insulating powders for temperatures from 10 K to 275 K”. In: *Thermal Conductivity 23*. CRC Press, 1996, pp. 383–394.

[82] Th. Rettelbach et al. *Thermal conductivity of silica aerogel powders at temperatures from 10 to 275 K*. Tech. rep. 1995, pp. 278–284.

[83] E. Ring. “Pressurizing Gas Thermodynamics”. In: *Rocket Propellant and Pressurization Systems*. Englewood Cliffs, NJ: Prentice-Hall Inc., 1964. Chap. 18.

[84] R. G. Ross Jr., ed. *Cryocoolers 10*. New York: Kluwer Academic / Plenum Publishers, 1999.

[85] D. Rusch and M. Casey. “The Design Space Boundaries for High Flow Capacity Centrifugal Compressors”. In: *Journal of Turbomachinery* 135.3 (May 2013). ISSN: 0889-504X. DOI: 10.1115/1.4007548.

[86] M. Sadílek et al. “The Analysis of Accuracy of Machined Surfaces and Surfaces Roughness after 3axis and 5axis Milling”. In: *Manufacturing Technology* 18.6 (Dec. 2018), pp. 1015–1022. ISSN: 12132489. DOI: 10.21062/ujep/217.2018/a/1213-2489/MT/18/6/1015.

[87] J. Schiffmann and D. Favrat. “Experimental investigation of a direct driven radial compressor for domestic heat pumps”. In: *International Journal of Refrigeration* 32.8 (Dec. 2009), pp. 1918–1928. ISSN: 01407007. DOI: 10.1016/j.ijrefrig.2009.07.006.

[88] J. D. Stanitz. *One-Dimensional Compressible Flow in Vaneless Diffusers of Radial- and Mixed-Flow Centrifugal Compressors, Including Effects of Friction, Heat Transfer and Area Change*. Tech. rep. Cleveland, Ohio: Lewis Flight Propulsion Laboratory, 1952.

[89] W. L. Swift et al. “The NICMOS cooling system—5 years of successful on-orbit operation”. In: *AIP Conference Proceedings*. AIP, 2008, pp. 799–806. DOI: 10.1063/1.2908673.

[90] C. Truesdell and R. Toupin. “The Classical Field Theories”. In: 1960, pp. 226–858. DOI: 10.1007/978-3-642-45943-6{_}2.

[91] D. Verstraete. “The Potential of Liquid Hydrogen for long range aircraft propulsion”. PhD thesis. Cranfield University, 2009.

[92] D. Verstraete et al. “Hydrogen fuel tanks for subsonic transport aircraft”. In: *International Journal of Hydrogen Energy* 35.20 (Oct. 2010), pp. 11085–11098. ISSN: 03603199. DOI: 10.1016/j.ijhydene.2010.06.060.

[93] C. Winnefeld et al. “Modelling and designing cryogenic hydrogen tanks for future aircraft applications”. In: *Energies* 11.1 (Jan. 2018). ISSN: 19961073. DOI: 10.3390/en11010105.

[94] C. W. C. van Woensel. *Integration of a Liquid Hydrogen Fuel Tank into the Concept of the Flying-V (MSc Thesis)*. Delft: Delft University of Technology, June 2021. URL: http://repository.tudelft.nl/..

[95] M. V. Zagarola. *A New Cryocooler for MgB2 Superconducting Systems in Turboelectric Aircraft*. June 2018. URL: https://techport.nasa.gov/view/90441.

[96] M. V. Zagarola, K. J. Cragin, and J. A. McCormick. “Operation of gas bearings at cryogenic temperatures”. In: *Cryogenics* 105 (Jan. 2020). ISSN: 00112275. DOI: 10.1016/j.cryogenics.2019.103001.

[97] M. V. Zagarola and J. A. McCormick. “High-capacity turbo-Brayton cryocoolers for space applications”. In: *Cryogenics* 46.2-3 (Feb. 2006), pp. 169–175. ISSN: 00112275. DOI: 10.1016/j.cryogenics.2005.11.018.

[98] M. V. Zagarola et al. “35 K Turbo-Brayton Cryocooler Technology”. In: *Advances in cryogenic engineering: transactions of the cryogenic engineering conference (CEC)*. Ed. by J Waynert et al. American Institute of Physics, 2003, pp. 1635–1642. DOI: 10.1063/1.1774861.

[99] M. V. Zagarola et al. “A 4 K tactical cryocooler using reverse-Brayton machines”. In: *IOP Conference Series: Materials Science and Engineering*. Vol. 279. 1. Institute of Physics Publishing, Dec. 2017. DOI: 10.1088/1757-899X/279/1/012015.

[100] M. V. Zagarola et al. *Efficiency Improvements for Turbo-Brayton Cryocoolers for Space*. Tech. rep. Hanover, NH, 03755 USA: Creare LLC, 2021.

A

Models and Results Repository

All models and results that can be made publicly available are stored at a public GitHub repository. The repository is accessible via:

`https://github.com/mikswart/Exploration-of-a-Reverse-Turbo-Brayton-Cryocooler-for-Carbon-Neutral-Aeronautical-Applications`

B

Definition of end domes with an aspect ratio

In order to include domes with an aspect ratio, a parameterisation needs to be performed to define the liquid level in the tank, and the additional volume. No relations for domes with an aspect ratio exist, so a different approach was opted. The relations for a sphere and cylinder are widely available and present in the model. As such, the computation of the domes is a combination of the computation of a sphere and a cylinder. The definition of a dome with an aspect ratio is shown in Figure B.1. As shown, the dome is effectively a cut-off from a bigger sphere with radius R_{eq}. To compute the volume of the two domes in the model, the volume of the equivalent sphere is calculated. From this equivalent sphere, the volume of two cylinders with radius R* and length L* are subtracted.

The error of using this method is shown in Figure B.3 for aspect ratio's above 0.5. Although in this research an aspect ratio of 1 is used, the model does offer the option to include AR with only a small error percentage in volume and area computation.

The following relations define the parameters shown in Figure B.1 and Figure B.2:

$$AR = \frac{h}{R_{tank_{int}}}, \qquad AR \leq 1 \tag{B.1}$$

$$R^* = \frac{R_{eq} + R_{tank_{int}}}{2}, \qquad L^* = R_{eq} - h \tag{B.2}$$

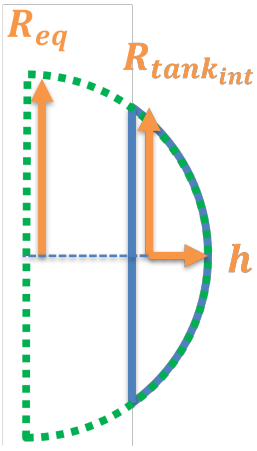

Figure B.1: Definition of the equivalent radius. The blue aspect ratio dome is a part of the green half-sphere.

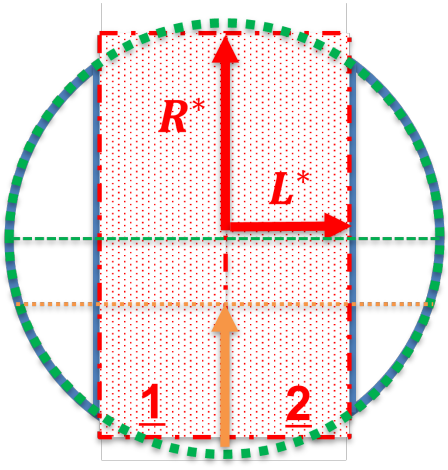

Figure B.2: Definition of R* and L*. The volume and liquid level in the blue domes is computed by computing the liquid level in the green sphere, where the volume of two red cylinders with radius R* and length L* are subtracted from.

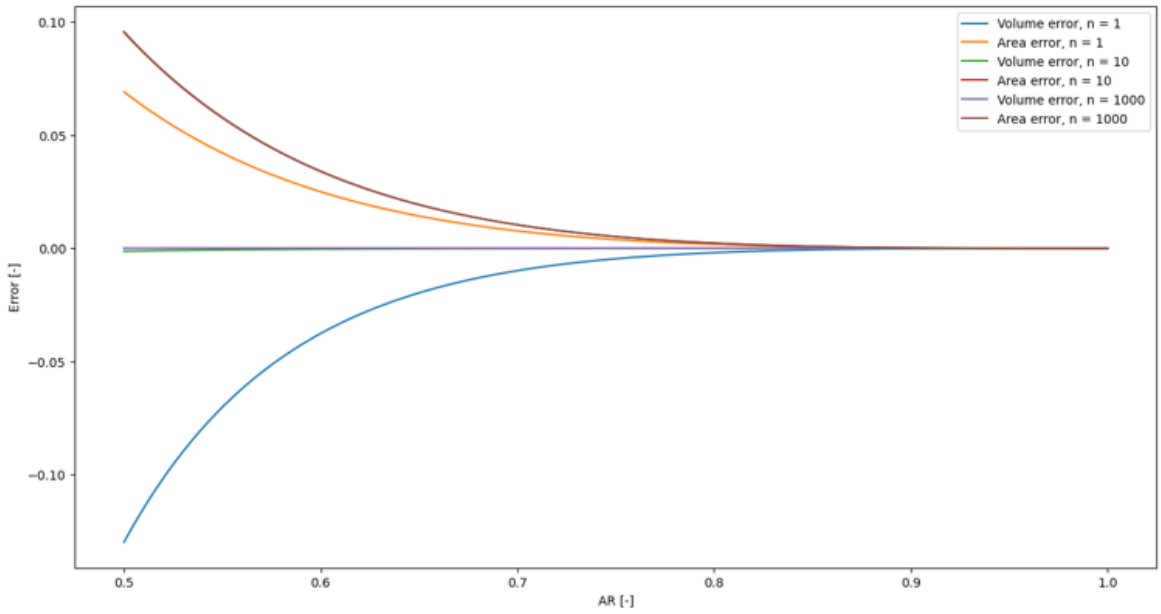

Figure B.3: The error in the volume and area estimations of the dome with an aspect ratio AR